BSGF - Earth Sciences Bulletin 2026, 197, 10
© B.J. Mbassa *et al.*, Published by EDP Sciences 2026
https://doi.org/10.1051/bsgf/2026005

BSGF
Earth Sciences Bulletin
Available online at:
www.bsgf.fr

Open Access

# Sub-continental lithospheric mantle beneath the Adamawa volcanic area (Cameroon Volcanic Line): inference from lavas and hosted mantle xenoliths from Bini Warack, NE-Ngaoundéré, Cameroon (Central Africa)

Benoît Joseph Mbassa[1,*], Olivier Vanderhaeghe[2], Michel Grégoire[2], Mathieu Benoît[2], Zenon Itiga[3], Caroline Ngwa Neh[1] and Pierre Kamgang[4]

[1] Institute of Geological and Mining Research, PO Box 4110, Yaoundé, Cameroon
[2] GET-OMP, Université de Toulouse, UPS, CNRS, IRD, CNES, 14 avenue E. Belin, 31400 Toulouse, France
[3] Département des Sciences de la Terre, Faculté des Sciences, Université de Douala, PO Box 24157 Douala, Cameroon
[4] Département des Sciences de la Terre, Faculté des Sciences, Université de Yaoundé I, BP 812 Yaoundé, Cameroon

Received: 29 July 2025 / Accepted: 20 March 2026 / Publishing online: 1 May 2026

**Abstract –** The sub-continental lithospheric mantle (SCLM) beneath the Cameroon Volcanic Line (CVL) is vertically and laterally heterogeneous, consisting of a complex mixing of DMM, HIMU, and EM1, affected by modal or cryptic metasomatism, depending on the area. The petrography, whole-rock geochemical data, and minerals' chemical composition of lavas and mantle xenoliths from the Bini Warack area, combined with Sr isotope compositions, provide constraints on the origin and thermochemical evolution of the SCLM beneath this sector of the CVL. The host lavas are basanite, basalt, and latite with OIB affinity, characterized by moderate to high silica and alkali contents ($SiO_2$ = 42.35–56.56 wt%, $K_2O+Na_2O$ = 2.34–7.07 wt%), a high Ba/Rb ranging from 12.2 to 26.1, a low Rb/Sr from 0.03 to 0.08, strong enrichment in LREE relative to HREE ($La_N/Yb_N$: 9.3–30), and moderate enrichment in radiogenic isotopes (*e.g.*, 0.702987 < $^{87}Sr/^{86}Sr_{initial}$ < 0.703206; 0.512854 < $^{143}Nd/^{144}Nd_{initial}$ < 0.512918) with positive $\varepsilon Nd_{initial}$ (+4.84 to +6.09). These features are consistent with an origin of the lavas by a low degree of partial melting (<2%) of a lherzolitic mantle source containing 2% to 6% garnet. These lavas have then evolved by fractional crystallization without any evidence of crustal contamination. The studied mantle xenoliths are spinel-bearing lherzolites, characterized by U/Th ratios typically lower than 1, a slight enrichment in LILE relative to HFSE, and mainly consist of minerals with fertile composition ($Fo_{84\text{-}91}$; spinel Cr#: 0.1–0.22; Al-rich pyroxenes). They are consistent with refractory mantle peridotite that evidences low partial-melting degrees. Trace element concentrations of host lavas (high Ba/Rb: 12.2–26.1 and low Rb/Sr: 0.03–0.08), together with olivine's crystals chemical features (high Ca/Fe and 100*Mn/Fe ratios; low 100*Ni/Mg ratios) and low Ca/Al ratios (<5) of clinopyroxenes in spinel-bearing lherzolite xenoliths suggest that the SCLM beneath the Bini Warack area is likely a juvenile lithospheric mantle which that undergone a carbonate-rich metasomatism.

**Keywords:** Cameroon Volcanic Line / OIB affinity / mantle xenoliths / spinel lherzolites / low partial melting degrees / carbonate metasomatism

**Résumé – Manteau lithosphérique sous-continental sous la zone volcanique de l'Adamaoua (Ligne Volcanique du Cameroun): inférence à partir des laves et xénolithes mantelliques de Bini Warack, NE-Ngaoundéré, Cameroun (Afrique centrale).** Le manteau lithosphérique sous-continental (MLSC) sous la ligne volcanique du Cameroun (LVC) est verticalement et latéralement hétérogène, constitué d'un mélange complexe de DMM, HIMU et EM1, affecté par un métasomatisme modal ou cryptique selon la zone. La pétrographie, les données géochimiques des roches totales ainsi que la composition chimique des minéraux des laves et des xénolithes mantelliques de la région de Bini Warack, combinées aux compositions

*Corresponding author: benjo_mbassa@yahoo.fr

isotopiques Sr, fournissent des informations sur l'origine et l'évolution thermochimique du MLSC sous ce secteur de la LVC. Les laves hôtes ont des compositions de basanite, basalte et de latite présentant des affinités avec les OIB, et caractérisées par i) des teneurs modérées à élevées en silice et en alcalins ($SiO_2$ = 42.35–56.56%, $K_2O+Na_2O$ = 2.34–7.07%), ii) de forts rapports Ba/Rb (12.2–26.1), iii) de faibles rapports Rb/Sr (0.03–0.08), iv) un fort enrichissement en terres rares légères par rapport aux terres rares lourdes ($La_N/Yb_N$ : 9.3–30), et v) un enrichissement modéré en isotopes radiogéniques ($0.702987 < {}^{87}Sr/{}^{86}Sr_{initial} < 0.703206$; $0.512854 < {}^{143}Nd/{}^{144}Nd_{initial} < 0.512918$) marqué par des εNd initiaux positifs (+4.84 – +6.09). Ces caractéristiques sont compatibles avec une origine des laves par un faible degré de fusion partielle (moins de 2%) d'un manteau à lherzolite contenant 2 à 6% de grenat. Les laves de Bini Warack ont ensuite évolué par cristallisation fractionnée sans trace de contamination crustale. Les xénolithes quant à eux sont des lherzolites à spinelle, caractérisés par des rapports U/Th généralement inférieurs à 1, un léger enrichissement en LILE par rapport aux HFSE et principalement constitués de minéraux de composition fertile ($Fo_{84\text{-}91}$; spinelle Cr# : 0.1–0.22; pyroxènes alumineux). Ces xénolithes sont compatibles avec un manteau péridotitique réfractaire ayant subi de faibles degrés de fusion partielle. Les teneurs en éléments traces des laves hôtes (Ba/Rb élevé : 12.2–26.1 et Rb/Sr faible : 0.03–0.08), les caractéristiques chimiques des cristaux d'olivine (rapports Ca/Fe et 100*Mn/Fe élevés; ainsi que les faibles rapports 100*Ni/Mg et Ca/Al <5) des clinopyroxènes des lherzolites étudiées, suggèrent que le MLSC sous la zone de Bini Warack est sans doute un manteau lithosphérique juvenile ayant subi un métasomatisme carbonaté.

**Mots-clés :** Ligne volcanique du Cameroun / affinité OIB / xénolites manteliques / lherzolites à spinelle / faibles degrés de fusion partielle / métasomatisme carbonatée

## 1 Introduction

Alkaline mafic to ultramafic volcanic rocks have been studied worldwide because they generally host mantle xenoliths that provide insights on the composition of the upper mantle. The mantle fragments found in volcanic areas emplaced within Archean and Paleoproterozoic belts have been considered to have a temporal and genetic relationship with the overlying crust (Carlson *et al.*, 2005), while in younger terranes and oceanic settings, this correlation remains unclear (Liu *et al.*, 2015, and references therein). The chemical diversity of continental intraplate magmas has been attributed to the heterogeneity of the mantle sources (Stracke *et al.*, 2005, and references therein) and/or to interactions between an upwelling plume and the lithospheric mantle or the upper crust (MacDonald *et al.*, 2001; Lundstrom *et al.*, 2003; Yokoyama *et al.*, 2007). The sub-continental lithospheric mantle (SCLM) is one of the Earth's reservoirs, representing about 2.5 vol.% of the whole mantle, where basaltic magmas are generated by direct melting (Hawkesworth *et al.*, 1983) or through delamination of this lithosphere and reincorporation of the convecting mantle (McKenzie and O'Nions 1983, 1995). The SCLM underlying some continental domains generally displays features of an OIB–mantle source and consists of lherzolites (Downes *et al.*, 2003). The composition of the SCLM is known from the study of either mantle xenoliths hosted in alkaline basalts or, more rarely, that of massive peridotites found in areas having undergone significant tectonic activity, such as Lherz in southern France. However, samples from both settings provide disrupted information on the SCLM due either to their interaction with the host magma in the case of mantle xenoliths or to wide serpentinization and interaction with crustal fluids during their emplacement in the case of massifs (Pearson and Nowell, 2002). Accordingly, characterizing the SCLM is crucial to understanding crustal growth and stabilization and the preservation and transformation of continents through time (Lin *et al.*, 2022).

In this contribution, we present a set of new field, mineralogical, petrographic, whole-rock geochemical, and Sr–Nd isotopic data on peridotite xenoliths together with their basaltic host lavas from Bini Warack in the Eastern Ngaoundéré area in order to characterize the regional SCLM beneath the Adamawa Plateau, discuss its origin and evolution, and explore the possible links to the growth and differentiation of the overlying Precambrian crust.

## 2 Geological context

The Cameroon Volcanic Line (CVL) is a 1600 km Y–shaped intracontinental mainly alkaline volcanic structure straddling the continent– ocean boundary, where the volcanic activity is due to instability within the subcontinental lithospheric mantle at the continental edge (Milelli *et al.*, 2012). The magmas have been proposed to originate either from an asthenospheric source or an enriched SCLM, without significant interaction with the overlying crusts (Marzoli *et al.*, 2000, Rankenburg *et al.*, 2005, Déruelle *et al.*, 2007). Volcanic rocks are typically $SiO_2$-undersaturated in the oceanic sector, mainly basaltic at the continent–ocean boundary with the exception of Mt Etinde that entirely consists of feldspathoids-rich lavas, then generally bimodal in the continental massifs, with abundant mafic and felsic lavas and with few intermediate terms.

The Ngaoundéré volcanic district, which includes our study area, is the easternmost area of the CVL (Fig. 1). The volcanic activity dated between the Oligocene and Pleistocene (Temdjim *et al.*, 2004; Itiga *et al.*, 2013) is characterized by the presence of numerous and diverse eruptive centers, including lava flows, cones, plugs, and maars, respectively associated with effusive and hydro-magmatic explosive dynamisms (Temdjim *et al.*, 2006; Nkouandou *et al.*, 2008; Tiabou *et al.*, 2019). Several studies based on xenoliths from the Ngaoundéré volcanic district (Nkouandou and Temdjim, 2011; Nguihdama *et al.*, 2014; Nkouandou *et al.*, 2015; Adama *et al.*, 2021;

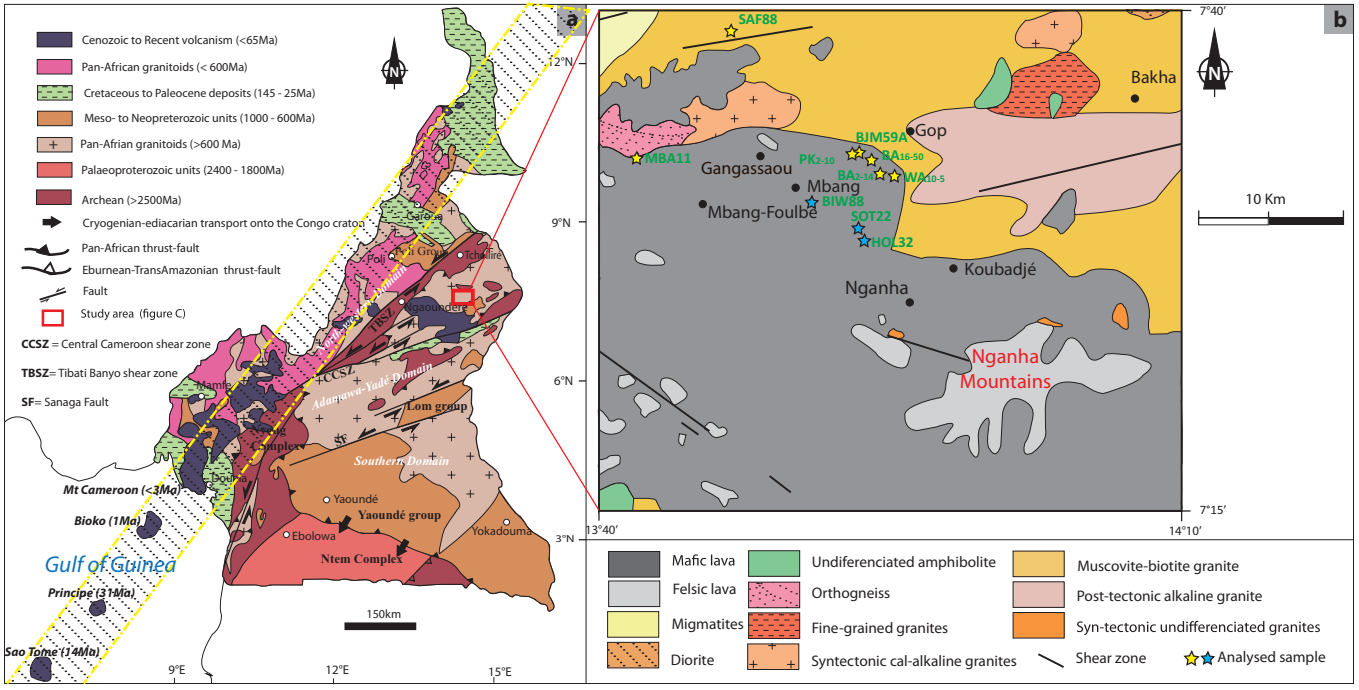


**Fig. 1.** Location of the study area: (a) Geological sketch of Cameroon (modified after Ngako *et al.*, 2003; Owona *et al.*, 2013) with the position of the study area; (b) Simplified geological map of the study area (modified from Mbassa *et al.*, 2025). The hatched band outlined by dashed yellow lines represents the CVL. The blue stars represent lava enclosing mantle xenoliths.

Wagsong Njombié *et al.*, 2018) provide significant information on the nature and the evolution of the lithosphere beneath. The mantle xenoliths of this volcanic district consist of lherzolite, harzburgite, and olivine websterite in Ngaoundéré (Nkouandou *et al.*, 2015), harzburgite in Lake Guinnadji and Ngao Djalsoka (Adama *et al.*, 2021), spinel-bearing lherzolite in Hosséré Garba (Nguihdama *et al.*, 2014), Ngao Voglar (Nkouandou and Temdjim, 2011), and Youkou (Wagson Njombié *et al.*, 2018). These xenoliths have been interpreted to represent refractory mantle residues after partial melting that have likely experienced refertilization processes. According to their equilibrium temperatures and corresponding pressures, xenoliths from the Adamawa region have been entrained from depths range from 25 to 85 km (Nkouandou and Temdjim, 2011; Nkouandou *et al.*, 2015), involving a limited asthenosphere upwelling. Metasomatic processes probably induced by plume-related hydrous silicate melts have been locally recorded and invoked to explain secondary enrichment in some highly incompatible trace elements (Wagsong Njombié *et al.*, 2018, Adama *et al.*, 2021). Overall, the SCLM beneath the CVL is likely both vertically and laterally heterogenous (Pintér *et al.*, 2015).

## 3 Samples processing and analytical methods

Twelve samples from the Bini Warak area, located NE of Ngaoundéré (Cameroon), including 6 mafic lavas and 6 mantle xenoliths, have been selected for the geochemical analyses. However, these analyses are supplemented by a certain number of published data from Tiabou *et al.* (2019) for a better discussion. Powders and thin sections of selected rock samples were prepared at the laboratory *Geosciences Environnement Toulouse* (GET) of the *CNRS-CNES-IRD-Université de Toulouse* (France) for geochemical and mineralogical analyses. Approximately 200 to 500 g of each sample were milled in a steel jaw crusher and then pulverized in an agate mortar for whole-rock geochemical and isotopic analysis. Whole-rock major and trace element concentrations have been determined at the *Service d'Analyses des Roches et des Minéraux* (SARM–CRPG, Nancy, France) by ICP–OES and ICP–MS, respectively, following the procedure described in Carignan *et al.* (2001).

The minerals' major element analyses were carried out at the *Centre de Microcaractérisation Raimond Castaing* of the *CNRS–Université de Toulouse* (France) using a Cameca SX Five electron microprobe. All analyzed samples were carbon coated (15 nm thick layer, density 2.25 g/cm$^3$) before being introduced in the electron microprobe. The analysis conditions were 15 kV accelerating voltage and 10 or 20 nA probe current depending on the resistance of the mineral to the electron beam. The synthetic and natural standards used for measurement of concentrations were albite (Na), corundum (Al), wollastonite (Si, Ca), sanidine (K), pyrophanite (Mn, Ti), hematite (Fe), periclase (Mg), Ni metal (Ni), $Cr_2O_3$ (Cr) and reference zircon (Zr). The acquisition times for most analyzed elements were 10 s at the peak and 5 s at either side of the peak for the continuous background. The detection limits were 70 ppm for Cr and Zr and 100 ppm for Ni. The modal proportion of minerals in lavas and xenoliths was determined using the *PetroMode* spreadsheet (Christiansen, 2009) based on sample whole-rock chemical composition and its mineral phases. Minerals' structural formulas were calculated using minerals spreadsheets available on the GabbroSoft website at http://www.gabbrosoft.org/.

The Sr/Nd isotopic data were performed for 4 basanites at the GET laboratory, using the Thermo Scientific TRITON+ solid-source mass spectrometer, following Labou *et al.* (2020) and Li *et al.* (2011, 2012) procedures. Before measurement, about 100 mg of whole-rock powder was weighed in a Teflon beaker and dissolved in a 1:1 $HF/HNO_3$ mixture. After dissolution, samples were diluted in 1 ml, 2% $HNO_3$, and Nd/Sr were extracted from the matrix (2N $HNO_3$) using a combination of Sr–Spec and Thru–Spec Eichrom resins. Mixed Sr and REE were loaded on a Re filament and were run sequentially (first Sr then Nd) using a double Re filament protocol. Interferences on $^{87}Rb$ and $^{144}Sm$ were monitored according to the protocol of Li *et al.* (2012), and the quality and reproducibility of the measurements were controlled using a sequential measurement of isotopic standards (SRM 987 and JNdi), doped isotopic standards (NBS 987+ Rb and JNdi + Sm), and laboratory-dedicated Sr + REE artificial solutions. Standard reproducibilities are $^{87}Sr/^{86}Sr$ = 0.710225, $^{143}Nd/^{144}Nd$ = 0.512509, and $^{145}Nd/^{144}Nd$ = 0.34897 for SRM–987 (pure and doped) and fall within the recommended values. Measured blanks are 26 pg for Nd and 432 pg for Sr. $^{87}Sr/^{86}Sr$ and $^{143}Nd/^{144}Nd$ ratios were normalized against $^{86}Sr/^{88}Sr$ = 0.1194 and $^{146}Nd/^{144}Nd$ = 0.7219, respectively, after corrections from isobaric interferences using $^{87}Rb/^{85}Sr$ = 0.387041 on $^{87}Sr$ and a combination of $^{147}Sm/^{149}Sm$ = 1.08583 and $^{147}Sm/^{144}Sm$ = 4.87090 on $^{144}Nd$.

## 4 Results

### 4.1 Petrography

#### 4.1.1 Host lavas

The host lavas have a microlitic aphyric or porphyritic texture (Fig. 2b–2c) with a vacuolar tendency. The groundmass is finely crystallized and made up of dominantly microlites of plagioclase, olivine, pyroxene, and opaque mineral microcrystals. The phenocryst phase is dominated by olivine, pyroxene, and opaque minerals. The accessory and/or secondary minerals consist of carbonate and chlorite. The clinopyroxene phenocrysts (0.7–0.3 mm in size) are elongated and subeuhedral with octagonal basal sections displaying two directions of cleavage (HOL32). Olivine (15.22–18.06 wt%) crystals have irregular shapes and various sizes (0.03–0.9 mm) and are often included in pyroxene, although some hexagonal basal sections, generally cracked, with a core more or less altered or resorbed by the groundmass (Fig. 2c), are locally observed. Some show a fan-shaped radial arrangement. Feldspar phenocrysts (0.02–0.4 mm in size) are generally elongated, twinned with intersecting cracks as the twin elongates, and include opaque minerals (HOL32). The vacuoles are locally filled with calcium carbonates.

Several samples contain mantle xenoliths or basement enclaves, all exhibiting a reaction rim in contact with the host lava. The crustal enclave displays a medium- to coarse-grained texture, dominated by quartz, potassic feldspars (Kfs) and plagioclase. Fe–Ti oxides and apatite are accessory minerals, while chlorite is secondary.

#### 4.1.2 Mantle xenoliths

Mantle xenoliths and xenocrysts hosted in lavas are rounded or angular fragments of variable size (1–8 cm). They are characterized by protogranular or porphyroblastic textures (Fig. 2d–2e) and usually display veinlets and melt pockets (Fig. 2g). When the xenocrysts are isolated in the host lavas, they show coronitic reactions consisting of either a spinel overgrowth or a spongy texture. They are essentially made up of four mineral phases, including olivine, clinopyroxene, orthopyroxene, and Cr–spinel, which are apparently in textural equilibrium. These rock-forming minerals display three generations of crystals: (1) euhedral porphyroblasts locally displaying abundant kink bands, undulose extinction, and mechanical twins of orthopyroxene (Fig. 2d), olivine, and Cr–spinel; (2) equidimensional granular neoblasts (Fig. 2f); and (3) microcrystals developed at the expense of porphyroblasts orin intraxenolith melt pools (Fig. 2e–2g). Olivine (41.3–69.5 vol.%) occurs as anhedral crystals with angular or subrounded shapes of variable size (0.5–1.5 mm) and is often included in pyroxenes. They are generally cracked, often rimmed or partially altered into serpentine (Fig. 2g) or Cr–spinel and locally exhibit undulose extinction. Clinopyroxene (11.2–22.2 vol.%) occurs both as small and as large porphyroblasts, often twinned and locally exhibiting undulose extinction. Orthopyroxene (9.8–37.4 vol.%) crystals are midway between olivine and clinopyroxene in terms of size (0.2–0.7 mm). Both clinopyroxene and orthopyroxene crystals are frequently crosscut by parallel melt veinlets and often display abundant fluid inclusions. Cr–spinels (~2 vol.%) are ubiquitous and occur either as large brown anhedral crystals (0.8–1.6 mm) rimmed by thick dark rims more or less altered or as fine dark microcrystals (<0.8 mm). The small crystals are dark and mostly present at interstitial positions between olivine and pyroxene crystals or include pyroxene and olivine phenocrysts (Fig. 2d). They are locally surrounded by melt pockets (Fig. 2g).

### 4.2 Minerals major elements composition

Some representative microprobe analyses of minerals major element compositions of lavas and hosted lherzolites are presented in Tables 1–4.

#### 4.2.1 Feldspars

Representative feldspar analyses from Bini Warack lavas exhibit wide ranges of CaO (0.1–13.8 wt%), $Al_2O_3$ (18.6–30.5 wt%), and FeO (0.1–1.12 wt%) contents (see Table 1). In the An–Ab–Or ternary diagram (Fig. 3a), plagioclase compositions range from labradorite ($An_{67.43–51.86}$) to albite ($An_{6.64}$) in basanites and from labradorite ($An_{53.21–50.47}$) to andesine ($An_{30.04–30.36}$) in latite. The rarely analyzed alkali feldspar is a sanidine ($Ab_{47.55}Or_{52.05}$) xenocryst, also observed in basanite (Sample MBA11–Analyse C3). A compositional variation marked by a significant enrichment in $Al_2O_3$, $K_2O$, and CaO and depletion of $Na_2O$ from the core to the rim of crystals is noticed in some andesine crystals of the latite (BJM59A).

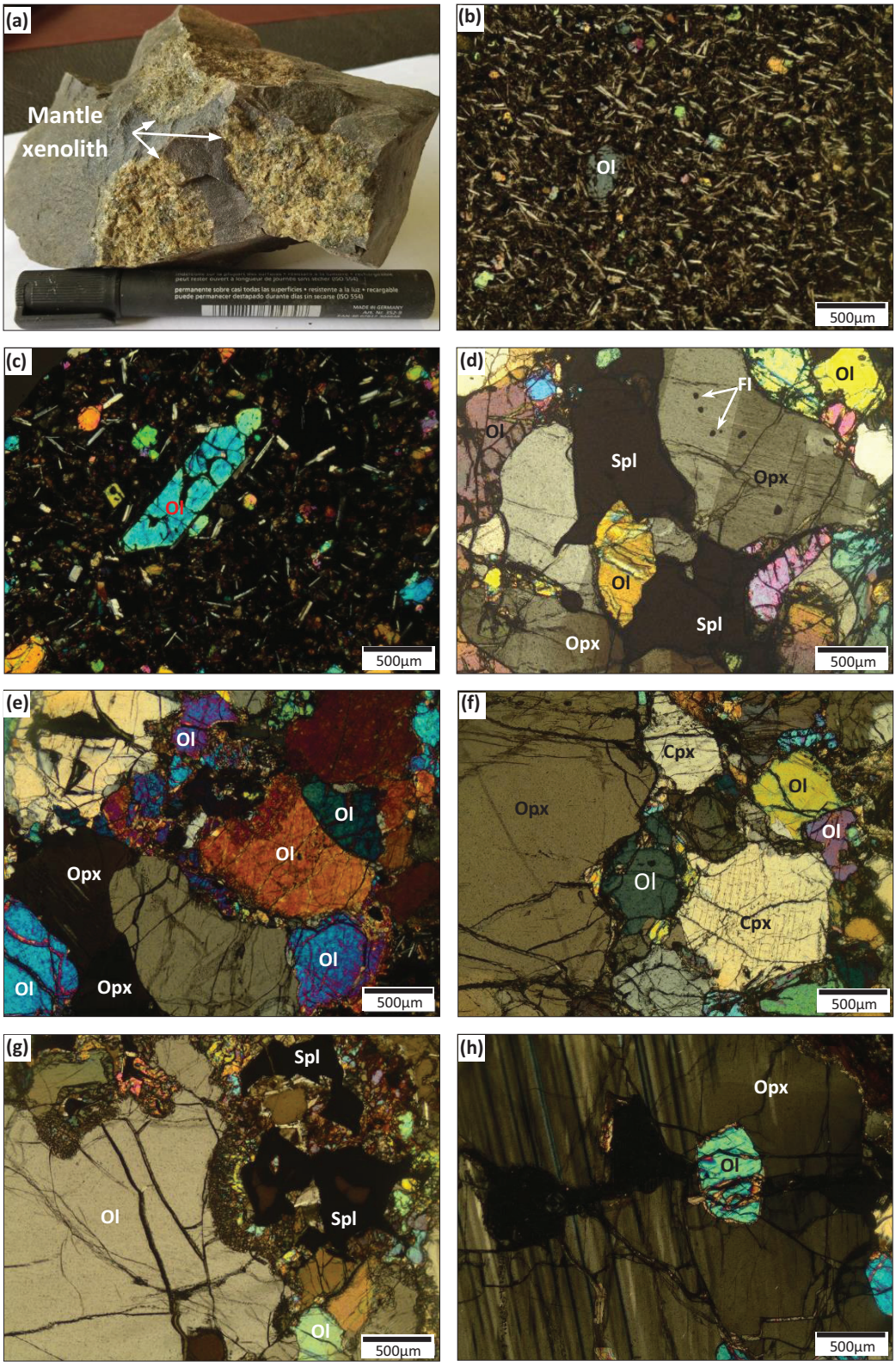


**Fig. 2.** Macroscopic view of host lava and photomicrographs taken under crossed-polarized light. (a) Lava sample hosting mantle xenoliths; (b) microlitic aphyric (SAF88) and (c) microlitic porphyritic texture of the study lavas (SOT22); (d) protogranular texture in a spinel lherzolite with a Cpx crystal showing spinel exsolution lamellae (BIW805); (e) porphyroblastic texture in spinel lherzolite (BIW88); (f) melt veinlets crosscutting olivine, Opx, and Cpx and twinned clinopyroxene crystal displaying numerous fluid inclusions and Cr-spinel encompassing olivine crystal (BIW88); (g) cumulus olivine crystal altered into serpentine and melt pocket around spinel crystal (BIW88); and (h) partially altered Opx phenocrystal including olivine and displaying parallel melt veinlets (BIW88). Mineral symbols are from Kretz *et al*. (1983); FI, fluid inclusion.

**Table 1.** Representative analyses of feldspars from Bini Warack lavas: (b) indicates border, (m) indicates middle, and (c) indicates core.

| **Rock type** | **Basanite** | | | | | | | | | | | | | | |
|---|---|---|---|---|---|---|---|---|---|---|---|---|---|---|---|
| Sample | BIW88AC1 | | | MBA11 | SAF88 | | | Sot22 | | | | | | | |
| Analyse | C1 | C1 (c) | C4 | C3 | C1(m) | C3(m) | C4(m) | C1(m) | C3 | C3 | C4 | C4 | C5 | C5 | C5 |
| **$SiO_2$** | 52.39 | 53.51 | 52.32 | 66.89 | 52.88 | 53.54 | 53.55 | 51.52 | 52.91 | 54.91 | 52.60 | 52.10 | 51.44 | 51.23 | 50.53 |
| **$TiO_2$** | 0.56 | 0.20 | 0.15 | 0.00 | 0.12 | 0.16 | 0.32 | 0.08 | 0.15 | 0.21 | 0.17 | 0.16 | 0.04 | 0.09 | 0.12 |
| **$Al_2O_3$** | 28.49 | 28.72 | 29.81 | 18.56 | 28.65 | 29.02 | 27.43 | 29.81 | 28.50 | 26.25 | 29.08 | 28.94 | 29.40 | 29.29 | 29.71 |
| **FeO** | 1.12 | 0.71 | 0.47 | 0.05 | 0.56 | 0.63 | 0.77 | 0.73 | 0.44 | 0.70 | 0.64 | 0.64 | 0.68 | 0.58 | 0.68 |
| **CaO** | 11.52 | 11.28 | 12.95 | 0.08 | 11.56 | 11.93 | 11.07 | 12.80 | 11.98 | 8.72 | 12.34 | 12.32 | 13.02 | 13.16 | 13.40 |
| **$Na_2O$** | 4.60 | 4.75 | 4.14 | 5.32 | 4.75 | 4.85 | 5.08 | 3.74 | 4.36 | 5.63 | 3.88 | 4.11 | 3.92 | 3.83 | 3.30 |
| **$K_2O$** | 1.21 | 0.44 | 0.33 | 8.85 | 0.26 | 0.29 | 0.91 | 0.33 | 0.47 | 1.34 | 0.64 | 0.58 | 0.52 | 0.43 | 0.42 |
| **BaO** | - | 0.07 | - | 0.00 | 0.03 | - | - | 0.10 | 0.10 | 0.61 | 0.11 | 0.15 | 0.01 | 0.08 | 0.04 |
| **MnO** | 0.02 | 0.00 | 0.01 | 0.00 | 0.00 | 0.03 | 0.04 | 0.06 | 0.03 | 0.01 | 0.00 | 0.01 | 0.02 | 0.03 | 0.09 |
| **MgO** | 0.32 | 0.03 | 0.08 | 0.00 | 0.08 | 0.02 | 0.31 | 0.09 | 0.06 | 0.01 | 0.04 | 0.10 | 0.09 | 0.05 | 0.16 |
| **NiO** | 0.02 | 0.05 | 0.07 | 0.00 | 0.01 | 0.00 | 0.00 | 0.00 | 0.00 | 0.00 | 0.00 | 0.04 | 0.00 | 0.00 | 0.03 |
| **F** | - | 0.03 | - | 0.24 | 0.16 | - | - | 0.00 | 0.05 | 0.00 | 0.00 | 0.00 | 0.37 | 0.05 | 0.11 |
| **Total** | **100.27** | **99.80** | **100.35** | **99.99** | **99.07** | **100.47** | **99.48** | **99.27** | **99.07** | **98.43** | **99.49** | **99.16** | **99.53** | **98.83** | **98.60** |
| **Si** | 9.61 | 9.75 | 9.51 | 12.059 | 9.71 | 9.69 | 9.84 | 9.47 | 9.72 | 10.16 | 9.63 | 9.60 | 9.48 | 9.48 | 9.39 |
| **Ti** | 0.08 | 0.03 | 0.02 | 0.00 | 0.02 | 0.02 | 0.04 | 0.01 | 0.02 | 0.03 | 0.02 | 0.02 | 0.01 | 0.01 | 0.02 |
| **Al** | 6.18 | 6.17 | 6.39 | 3.94 | 6.20 | 6.19 | 5.94 | 6.46 | 6.17 | 5.72 | 6.27 | 6.28 | 6.39 | 6.39 | 6.51 |
| **$Fe^{2+}$** | 0.17 | 0.11 | 0.07 | 0.01 | 0.09 | 0.10 | 0.12 | 0.11 | 0.07 | 0.11 | 0.10 | 0.10 | 0.11 | 0.09 | 0.11 |
| **Ca** | 2.26 | 2.20 | 2.52 | 0.02 | 2.28 | 2.31 | 2.18 | 2.52 | 2.36 | 1.73 | 2.42 | 2.43 | 2.57 | 2.61 | 2.67 |
| **Na** | 1.64 | 1.68 | 1.46 | 1.86 | 1.69 | 1.70 | 1.81 | 1.33 | 1.55 | 2.02 | 1.38 | 1.47 | 1.40 | 1.37 | 1.19 |
| **K** | 0.28 | 0.10 | 0.08 | 2.04 | 0.06 | 0.07 | 0.21 | 0.08 | 0.11 | 0.32 | 0.15 | 0.14 | 0.12 | 0.10 | 0.10 |
| **Ba** | 0.00 | 0.01 | 0.01 | 0.00 | 0.00 | 0.00 | 0.00 | 0.01 | 0.01 | 0.04 | 0.01 | 0.01 | 0.00 | 0.01 | 0.00 |
| **SUM** | **20.20** | **20.03** | **20.05** | **19.92** | **20.05** | **20.08** | **20.15** | **19.99** | **20.01** | **20.12** | **19.98** | **20.04** | **20.08** | **20.06** | **19.98** |
| **An** | 54.12 | 55.30 | 62.16 | 0.40 | 56.49 | 56.67 | 51.86 | 64.13 | 58.64 | 42.53 | 61.32 | 60.25 | 62.80 | 63.88 | 67.43 |
| **Ab** | 39.11 | 42.14 | 35.96 | 47.55 | 42.00 | 41.69 | 43.07 | 33.91 | 38.62 | 49.69 | 34.89 | 36.37 | 34.22 | 33.64 | 30.05 |
| **Or** | 6.77 | 2.57 | 1.87 | 52.05 | 1.51 | 1.64 | 5.08 | 1.97 | 2.74 | 7.78 | 3.79 | 3.38 | 2.97 | 2.49 | 2.52 |

**Table 1.** (continued).

| **Rock type** | | **Basanite** | | | | | | | **Latite** | | | |
|---|---|---|---|---|---|---|---|---|---|---|---|---|
| **Sample** | | **SOT22** | | | **HOL32** | **BJM59A** | | | | | | |
| **Analyse** | C6 | C6 | C6 | C6 | C6 | C1(m) | C3(c) | C3(c) | C3(b) | C4-(m) | (C5) | C5(m) |
| **$SiO_2$** | 52.87 | 52.70 | 52.29 | 51.08 | 51.50 | 56.81 | 61.01 | 60.46 | 56.38 | 55.86 | 54.70 | 55.19 |
| **$TiO_2$** | 0.39 | 0.16 | 0.16 | 0.14 | 0.10 | 0.06 | 0.00 | 0.00 | 0.08 | 0.05 | 0.07 | 0.12 |
| **$Al_2O_3$** | 24.17 | 29.46 | 29.04 | 30.21 | 30.50 | 26.39 | 24.22 | 24.09 | 26.26 | 27.08 | 27.92 | 27.51 |
| **FeO** | 1.11 | 0.62 | 0.61 | 0.60 | 0.50 | 0.58 | 0.21 | 0.20 | 0.52 | 0.54 | 0.45 | 0.59 |
| **CaO** | 8.72 | 12.52 | 12.68 | 13.86 | 13.87 | 9.34 | 6.42 | 6.53 | 9.16 | 9.92 | 11.05 | 10.55 |
| **$Na_2O$** | 5.56 | 4.19 | 4.01 | 3.41 | 3.68 | 5.97 | 7.89 | 7.88 | 6.03 | 5.49 | 5.00 | 5.24 |
| **$K_2O$** | 2.56 | 0.32 | 0.36 | 0.34 | 0.33 | 0.90 | 0.56 | 0.60 | 0.74 | 0.63 | 0.56 | 0.73 |
| **BaO** | 0.31 | 0.02 | 0.04 | 0.04 | - | - | - | 0.01 | 0.00 | - | - | - |
| **MnO** | 0.00 | 0.03 | 0.04 | 0.00 | 0.03 | 0.00 | 0.02 | 0.01 | 0.04 | 0.01 | 0.00 | 0.00 |
| **MgO** | 0.12 | 0.06 | 0.08 | 0.22 | 0.09 | 0.06 | 0.00 | 0.01 | 0.09 | 0.05 | 0.12 | 0.05 |
| **NiO** | 0.00 | 0.00 | 0.00 | 0.00 | 0.00 | 0.02 | 0.00 | 0.05 | 0.05 | 0.00 | 0.00 | 0.00 |
| **F** | 0.05 | 0.00 | 0.00 | 0.19 | - | - | - | 0.08 | 0.08 | - | - | - |
| **Total** | **95.96** | **100.08** | **99.31** | **100.09** | **100.63** | **100.14** | **100.33** | **99.92** | **99.42** | **99.63** | **99.87** | **99.98** |
| **Si** | 10.16 | 9.57 | 9.595 | 9.36 | 9.36 | 10.26 | 10.85 | 10.83 | 10.26 | 10.13 | 9.93 | 10.00 |
| **Ti** | 0.06 | 0.02 | 0.022 | 0.02 | 0.01 | 0.01 | 0.00 | 0.00 | 0.01 | 0.01 | 0.01 | 0.02 |
| **Al** | 5.48 | 6.32 | 6.280 | 6.52 | 6.53 | 5.62 | 5.08 | 5.08 | 5.63 | 5.79 | 5.97 | 5.88 |
| **$Fe^{2+}$** | 0.18 | 0.09 | 0.094 | 0.09 | 0.08 | 0.09 | 0.03 | 0.03 | 0.08 | 0.08 | 0.07 | 0.09 |
| **Ca** | 1.80 | 2.44 | 2.493 | 2.72 | 2.70 | 1.81 | 1.22 | 1.25 | 1.79 | 1.93 | 2.15 | 2.05 |
| **Na** | 2.07 | 1.48 | 1.427 | 1.21 | 1.30 | 2.09 | 2.72 | 2.74 | 2.13 | 1.93 | 1.76 | 1.84 |
| **K** | 0.63 | 0.07 | 0.084 | 0.08 | 0.08 | 0.21 | 0.13 | 0.14 | 0.17 | 0.15 | 0.13 | 0.17 |
| **Ba** | 0.02 | 0.00 | 0.00 | 0.00 | 0.00 | 0.00 | 0.00 | 0.00 | 0.00 | 0.00 | 0.00 | 0.00 |
| **SUM** | **20.39** | **20.01** | **20.00** | **20.01** | **20.05** | **20.07** | **20.03** | **20.07** | **20.06** | **20.01** | **20.02** | **20.05** |
| **An** | 39.95 | 61.12 | 62.26 | 67.82 | 66.29 | 44.03 | 30.05 | 30.37 | 43.72 | 48.14 | 53.22 | 50.46 |
| **Ab** | 46.09 | 37.02 | 35.63 | 30.20 | 31.83 | 50.92 | 66.83 | 66.31 | 52.08 | 48.22 | 43.57 | 45.37 |
| **Or** | 13.96 | 1.86 | 2.10 | 1.98 | 1.88 | 5.05 | 3.12 | 3.32 | 4.21 | 3.64 | 3.21 | 4.16 |

**Table 2.** Representative analyses of olivines form study area; (b) indicates border and (c) indicates core.

| **Rock type** | **Basanite** | | | | | | | | | | | | | | | | | | | | | |
|---|---|---|---|---|---|---|---|---|---|---|---|---|---|---|---|---|---|---|---|---|---|---|
| **samples** | BIW88A | | | | | | | | | SAF88 | | | | | | | Sot22 | | | | | |
| **Analyses** | **C1-b** | **C2 (c)** | **C2(b)** | **C2(c)** | **C3** | **C3** | **C4(b)** | **C4(c)** | **C4(c)** | **C1** | **C3** | **C2** | **C2(c)** | **C2(b)** | **C1(b)** | **C1(c)** | **C3** | **C4(b)** | **C4(c)** | **C5** | **C6(c)** | **C6(b)** |
| **$SiO_2$** | 39.90 | 39.75 | 41.28 | 41.48 | 41.64 | 41.75 | 40.71 | 41.32 | 41.35 | 38.19 | 39.34 | 40.16 | 40.55 | 39.70 | 39.84 | 39.35 | 40.20 | 40.26 | 40.39 | 38.58 | 38.97 | 40.17 |
| **$TiO_2$** | 0.00 | 0.10 | 0.00 | 0.00 | 0.00 | 0.00 | 0.00 | 0.00 | 0.00 | 0.08 | 0.00 | 0.01 | 0.00 | 0.00 | 0.00 | 0.00 | 0.00 | 0.00 | 0.00 | 0.00 | 0.00 | 0.00 |
| **$Al_2O_3$** | 0.00 | 0.10 | 0.00 | 0.07 | 0.00 | 0.06 | 0.05 | 0.00 | 0.06 | 0.08 | 0.02 | 0.02 | 0.05 | 0.03 | 0.04 | 0.04 | 0.06 | 0.02 | 0.04 | 0.08 | 0.00 | 0.00 |
| **$Cr_2O_3$** | 0.00 | 0.02 | 0.01 | 0.04 | 0.03 | 0.06 | 0.01 | 0.03 | 0.03 | 0.01 | 0.01 | 0.02 | 0.04 | 0.02 | 0.02 | 0.00 | 0.03 | 0.02 | 0.03 | 0.00 | 0.01 | 0.03 |
| **FeO** | 18.34 | 17.61 | 9.15 | 8.68 | 8.83 | 8.90 | 10.34 | 10.08 | 9.69 | 25.71 | 20.04 | 15.52 | 14.10 | 16.42 | 17.13 | 19.54 | 15.03 | 14.52 | 15.75 | 21.91 | 20.83 | 14.24 |
| **MnO** | 0.35 | 0.21 | 0.18 | 0.19 | 0.15 | 0.16 | 0.06 | 0.16 | 0.05 | 0.57 | 0.48 | 0.27 | 0.25 | 0.28 | 0.21 | 0.29 | 0.25 | 0.22 | 0.09 | 0.29 | 0.23 | 0.20 |
| **MgO** | 41.49 | 42.21 | 48.94 | 49.34 | 49.09 | 49.48 | 48.02 | 48.85 | 48.34 | 35.83 | 40.51 | 43.17 | 44.77 | 42.27 | 42.42 | 40.37 | 43.93 | 44.45 | 43.54 | 38.34 | 39.93 | 45.05 |
| **NiO** | 0.14 | 0.10 | 0.45 | 0.30 | 0.44 | 0.47 | 0.30 | 0.45 | 0.34 | 0.05 | 0.21 | 0.17 | 0.21 | 0.17 | 0.25 | 0.23 | 0.24 | 0.23 | 0.20 | 0.05 | 0.06 | 0.14 |
| **CaO** | 0.31 | 0.09 | 0.12 | 0.13 | 0.06 | 0.08 | 0.10 | 0.10 | 0.12 | 0.38 | 0.07 | 0.36 | 0.28 | 0.32 | 0.11 | 0.04 | 0.23 | 0.27 | 0.17 | 0.23 | 0.14 | 0.20 |
| **$Na_2O$** | 0.06 | 0.00 | 0.00 | 0.00 | 0.00 | 0.00 | 0.07 | 0.03 | 0.00 | 0.02 | 0.00 | 0.01 | 0.00 | 0.00 | 0.01 | 0.00 | 0.02 | 0.02 | 0.00 | 0.03 | 0.05 | 0.00 |
| **$K_2O$** | 0.00 | 0.00 | 0.06 | 0.00 | 0.06 | 0.00 | 0.02 | 0.03 | 0.00 | 0.00 | 0.00 | 0.00 | 0.01 | 0.00 | 0.01 | 0.02 | 0.00 | 0.01 | 0.00 | 0.03 | 0.02 | 0.00 |
| **Total** | **100.60** | **100.18** | **100.25** | **100.36** | **100.33** | **100.98** | **99.79** | **101.12** | **100.00** | **100.92** | **100.69** | **99.71** | **100.25** | **99.22** | **100.04** | **99.89** | **100.00** | **100.10** | **100.34** | **99.55** | **100.29** | **100.13** |
| Si | 1.01 | 1.01 | 1.01 | 1.01 | 1.01 | 1.01 | 1.00 | 1.01 | 1.01 | 1.00 | 1.01 | 1.02 | 1.01 | 1.01 | 1.01 | 1.01 | 1.01 | 1.01 | 1.01 | 1.01 | 1.00 | 1.01 |
| **Ti** | 0.00 | 0.00 | 0.00 | 0.00 | 0.00 | 0.00 | 0.00 | 0.00 | 0.00 | 0.00 | 0.00 | 0.00 | 0.00 | 0.00 | 0.00 | 0.00 | 0.00 | 0.00 | 0.00 | 0.00 | 0.00 | 0.00 |
| **Al** | 0.00 | 0.00 | 0.00 | 0.00 | 0.00 | 0.00 | 0.00 | 0.00 | 0.00 | 0.00 | 0.00 | 0.00 | 0.00 | 0.00 | 0.00 | 0.00 | 0.00 | 0.00 | 0.00 | 0.00 | 0.00 | 0.00 |
| **Cr** | 0.00 | 0.00 | 0.00 | 0.00 | 0.00 | 0.00 | 0.00 | 0.00 | 0.00 | 0.00 | 0.00 | 0.00 | 0.00 | 0.00 | 0.00 | 0.00 | 0.00 | 0.00 | 0.00 | 0.00 | 0.00 | 0.00 |
| **Fe2+** | 0.39 | 0.37 | 0.19 | 0.18 | 0.18 | 0.18 | 0.21 | 0.21 | 0.20 | 0.57 | 0.43 | 0.33 | 0.29 | 0.35 | 0.36 | 0.42 | 0.32 | 0.30 | 0.33 | 0.48 | 0.45 | 0.30 |
| **Mn** | 0.01 | 0.00 | 0.00 | 0.00 | 0.00 | 0.00 | 0.00 | 0.00 | 0.00 | 0.01 | 0.01 | 0.01 | 0.01 | 0.01 | 0.00 | 0.01 | 0.01 | 0.00 | 0.00 | 0.01 | 0.01 | 0.00 |
| **Mg** | 1.57 | 1.60 | 1.78 | 1.79 | 1.78 | 1.78 | 1.77 | 1.77 | 1.76 | 1.40 | 1.54 | 1.63 | 1.67 | 1.61 | 1.60 | 1.55 | 1.65 | 1.66 | 1.63 | 1.49 | 1.53 | 1.68 |
| **Ni** | 0.00 | 0.00 | 0.01 | 0.01 | 0.01 | 0.01 | 0.01 | 0.01 | 0.01 | 0.00 | 0.00 | 0.00 | 0.00 | 0.00 | 0.01 | 0.00 | 0.00 | 0.00 | 0.00 | 0.00 | 0.00 | 0.00 |
| **Ca** | 0.01 | 0.00 | 0.00 | 0.00 | 0.00 | 0.00 | 0.00 | 0.00 | 0.00 | 0.01 | 0.00 | 0.01 | 0.01 | 0.01 | 0.00 | 0.00 | 0.01 | 0.01 | 0.00 | 0.01 | 0.00 | 0.01 |
| **Total** | **2.99** | **2.99** | **2.99** | **2.99** | **2.99** | **2.99** | **3.00** | **3.00** | **2.99** | **3.00** | **3.00** | **2.99** | **2.99** | **2.99** | **2.99** | **2.99** | **2.99** | **3.00** | **2.99** | **3.00** | **3.00** | **3.00** |
| **Fo** | 79.83 | 80.85 | 90.34 | 90.84 | 90.69 | 90.68 | 89.17 | 89.48 | 89.85 | 70.85 | 77.87 | 82.97 | 84.76 | 81.86 | 81.35 | 78.40 | 83.67 | 84.31 | 83.05 | 75.48 | 77.17 | 84.76 |
| **Fa** | 19.79 | 18.92 | 9.47 | 8.96 | 9.15 | 9.15 | 10.77 | 10.36 | 10.10 | 28.51 | 21.61 | 16.73 | 14.97 | 17.84 | 18.42 | 21.28 | 16.06 | 15.45 | 16.85 | 24.19 | 22.58 | 15.03 |
| **Tp** | 0.38 | 0.23 | 0.19 | 0.20 | 0.16 | 0.17 | 0.06 | 0.17 | 0.05 | 0.64 | 0.52 | 0.29 | 0.27 | 0.31 | 0.23 | 0.32 | 0.27 | 0.24 | 0.10 | 0.32 | 0.25 | 0.21 |

**Table 2.** (continued).

| Rock type | | | | | Basanite | | | | | | | | | Basalt | | | | |
|---|---|---|---|---|---|---|---|---|---|---|---|---|---|---|---|---|---|---|
| Sample | | | | | HOL32 | | | | | | | | | MBA11 | | | | |
| Analyses | C1 | C2 | C2 | C4 | C4 | C4 | C5 | C5 | C5 | C1 | C2 | C2(c) | C2(b) | C2(c) | C4(b) | C4(c) | C5 | C5 |
| **$SiO_2$** | 39.68 | 40.06 | 40.53 | 39.72 | 40.21 | 39.76 | 39.73 | 39.92 | 39.90 | 41.52 | 40.86 | 40.95 | 41.33 | 41.44 | 41.53 | 41.03 | 42.05 | 41.55 |
| **$TiO_2$** | 0.00 | 0.00 | 0.01 | 0.00 | 0.02 | 0.00 | 0.00 | 0.01 | 0.00 | 0.00 | 0.00 | 0.00 | 0.00 | 0.00 | 0.00 | 0.08 | 0.00 | 0.00 |
| **$Al_2O_3$** | 0.00 | 0.06 | 0.04 | 0.07 | 0.00 | 0.11 | 0.00 | 0.09 | 0.05 | 0.07 | 0.03 | 0.05 | 0.08 | 0.02 | 0.06 | 0.04 | 0.05 | 0.05 |
| **$Cr_2O_3$** | 0.00 | 0.01 | 0.00 | 0.05 | 0.05 | 0.02 | 0.01 | 0.00 | 0.04 | 0.02 | 0.02 | 0.00 | 0.03 | 0.02 | 0.02 | 0.00 | 0.01 | 0.01 |
| **FeO** | 16.55 | 16.76 | 14.5 | 12.71 | 12.96 | 15.09 | 13.03 | 15.31 | 13.77 | 10.38 | 11.31 | 11.68 | 10.72 | 10.28 | 9.47 | 9.49 | 8.72 | 8.94 |
| **MnO** | 0.18 | 0.09 | 0.24 | 0.17 | 0.22 | 0.32 | 0.20 | 0.27 | 0.16 | 0.13 | 0.21 | 0.14 | 0.14 | 0.11 | 0.20 | 0.10 | 0.12 | 0.17 |
| **MgO** | 44.02 | 43.77 | 45.04 | 47.55 | 46.8 | 45.36 | 46.69 | 44.15 | 45.98 | 48.35 | 47.85 | 47.6 | 48.21 | 48.73 | 48.88 | 48.47 | 48.84 | 49.62 |
| **NiO** | 0.28 | 0.22 | 0.25 | 0.22 | 0.36 | 0.28 | 0.23 | 0.15 | 0.32 | 0.39 | 0.28 | 0.42 | 0.34 | 0.37 | 0.5 | 0.41 | 0.3 | 0.36 |
| **CaO** | 0.10 | 0.15 | 0.04 | 0.31 | 0.22 | 0.20 | 0.15 | 0.05 | 0.20 | 0.06 | 0.05 | 0.04 | 0.14 | 0.11 | 0.05 | 0.02 | 0.04 | 0.08 |
| **$Na_2O$** | 0.00 | 0.01 | 0.00 | 0.04 | 0.01 | 0.00 | 0.07 | 0.05 | 0.02 | 0.00 | 0.02 | 0.07 | 0.03 | 0.02 | 0.01 | 0.00 | 0.11 | 0.00 |
| **$K_2O$** | 0.02 | 0.00 | 0.00 | 0.00 | 0.01 | 0.03 | 0.00 | 0.04 | 0.00 | 0.00 | 0.02 | 0.01 | 0.01 | 0.00 | 0.03 | 0.01 | 0.01 | 0.00 |
| **Total** | **100.84** | **101.12** | **100.65** | **100.84** | **100.86** | **101.18** | **100.12** | **100.03** | **100.44** | **100.93** | **100.65** | **100.97** | **101.02** | **101.10** | **100.76** | **99.66** | **100.33** | **100.86** |
| **Si** | 1.00 | 1.00 | 1.01 | 0.98 | 1.00 | 0.99 | 0.99 | 1.00 | 1.00 | 1.01 | 1.00 | 1.00 | 1.01 | 1.01 | 1.01 | 1.01 | 1.02 | 1.01 |
| **Ti** | 0.00 | 0.00 | 0.00 | 0.00 | 0.00 | 0.00 | 0.00 | 0.00 | 0.00 | 0.00 | 0.00 | 0.00 | 0.00 | 0.00 | 0.00 | 0.00 | 0.00 | 0.00 |
| **Al** | 0.00 | 0.00 | 0.00 | 0.00 | 0.00 | 0.00 | 0.00 | 0.00 | 0.00 | 0.00 | 0.00 | 0.00 | 0.00 | 0.00 | 0.00 | 0.00 | 0.00 | 0.00 |
| **Cr** | 0.00 | 0.00 | 0.00 | 0.00 | 0.00 | 0.00 | 0.00 | 0.00 | 0.00 | 0.00 | 0.00 | 0.00 | 0.00 | 0.00 | 0.00 | 0.00 | 0.00 | 0.00 |
| **$Fe^{2+}$** | 0.35 | 0.35 | 0.30 | 0.26 | 0.27 | 0.31 | 0.27 | 0.32 | 0.29 | 0.21 | 0.23 | 0.24 | 0.22 | 0.21 | 0.19 | 0.19 | 0.18 | 0.18 |
| **Mn** | 0.00 | 0.00 | 0.01 | 0.00 | 0.00 | 0.01 | 0.00 | 0.01 | 0.00 | 0.00 | 0.00 | 0.00 | 0.00 | 0.00 | 0.00 | 0.00 | 0.00 | 0.00 |
| **Mg** | 1.65 | 1.63 | 1.67 | 1.76 | 1.73 | 1.69 | 1.74 | 1.66 | 1.71 | 1.75 | 1.75 | 1.74 | 1.75 | 1.77 | 1.77 | 1.77 | 1.77 | 1.79 |
| **Ni** | 0.01 | 0.00 | 0.01 | 0.00 | 0.01 | 0.01 | 0.00 | 0.00 | 0.01 | 0.01 | 0.01 | 0.01 | 0.01 | 0.01 | 0.01 | 0.01 | 0.01 | 0.01 |
| **Ca** | 0.00 | 0.00 | 0.00 | 0.01 | 0.01 | 0.01 | 0.00 | 0.00 | 0.01 | 0.00 | 0.00 | 0.00 | 0.00 | 0.00 | 0.00 | 0.00 | 0.00 | 0.00 |
| **Total** | **3.01** | **3.00** | **2.99** | **3.02** | **3.01** | **3.01** | **3.01** | **3.00** | **3.01** | **2.99** | **3.00** | **3.00** | **2.99** | **3.00** | **2.99** | **2.99** | **2.98** | **2.99** |
| **Fo** | 82.43 | 82.24 | 84.49 | 86.81 | 86.36 | 83.99 | 86.28 | 83.47 | 85.47 | 89.13 | 88.10 | 87.77 | 88.78 | 89.32 | 90.01 | 90.01 | 90.78 | 90.66 |
| **Fa** | 17.38 | 17.66 | 15.26 | 13.01 | 13.41 | 15.67 | 13.51 | 16.24 | 14.36 | 10.73 | 11.68 | 12.08 | 11.07 | 10.57 | 9.78 | 9.88 | 9.09 | 9.16 |
| **Tp** | 0.19 | 0.10 | 0.26 | 0.18 | 0.23 | 0.34 | 0.21 | 0.29 | 0.17 | 0.14 | 0.22 | 0.15 | 0.15 | 0.11 | 0.21 | 0.11 | 0.13 | 0.18 |

**Table 2.** (continued).

| Rock type | Lherzolite | | | | | | | | | | | | | | | | | | Xenocrists | | | | |
|---|---|---|---|---|---|---|---|---|---|---|---|---|---|---|---|---|---|---|---|---|---|---|---|
| Sample | C1(b) | C1(c) | C2 | C2(b) | C3 | C3 | C3(c) | BIW805 C3 | C3(c) | C4 | C4(c) | C6 | C6 | C7(b) | C7(c) | C7 | C5 | BIW88A C5(b) | C5 | C4 | BIW88 C6 | C2 |
| Analyses | | | | | | | | | | | | | | | | | | | | | | |
| **$SiO_2$** | 41.08 | 41.37 | 41.39 | 41.49 | 41.11 | 41.15 | 41.32 | 41.01 | 41.15 | 41.35 | 41.19 | 41.3 | 41.69 | 41.28 | 41.15 | 41.24 | 41.4 | 40.99 | 40.79 | 41.59 | 41.42 | 40.41 |
| **$TiO_2$** | 0.01 | 0.00 | 0.00 | 0.00 | 0.00 | 0.00 | 0.00 | 0.00 | 0.00 | 0.00 | 0.00 | 0.00 | 0.00 | 0.00 | 0.00 | 0.00 | 0.00 | 0.01 | 0.00 | 0.00 | 0.00 | 0.00 |
| **$Al_2O_3$** | 0.06 | 0.04 | 0.01 | 0.05 | 0.03 | 0.00 | 0.03 | 0.05 | 0.03 | 0.04 | 0.00 | 0.01 | 0.00 | 0.00 | 0.05 | 0.03 | 0.04 | 0.02 | 0.00 | 0.04 | 0.05 | 0.06 |
| **$Cr_2O_3$** | 0.05 | 0.00 | 0.01 | 0.01 | 0.01 | 0.01 | 0.00 | 0.00 | 0.00 | 0.01 | 0.00 | 0.02 | 0.00 | 0.01 | 0.00 | 0.00 | 0.03 | 0.03 | 0.04 | 0.00 | 0.01 | 0.02 |
| **FeO** | 10.07 | 9.76 | 9.69 | 9.64 | 9.56 | 9.62 | 9.59 | 9.66 | 9.62 | 9.53 | 9.62 | 9.67 | 9.78 | 9.79 | 9.72 | 9.65 | 8.67 | 8.96 | 9.68 | 10.23 | 10.01 | 14.75 |
| **MnO** | 0.13 | 0.10 | 0.15 | 0.19 | 0.13 | 0.15 | 0.13 | 0.14 | 0.10 | 0.10 | 0.10 | 0.13 | 0.11 | 0.17 | 0.11 | 0.14 | 0.15 | 0.15 | 0.18 | 0.11 | 0.16 | 0.25 |
| **MgO** | 47.38 | 47.98 | 48.82 | 48.26 | 48.52 | 48.30 | 48.00 | 48.27 | 48.38 | 48.15 | 48.27 | 48.51 | 49.09 | 48.62 | 48.79 | 48.49 | 49.17 | 49.56 | 48.58 | 48.58 | 48.62 | 44.67 |
| **NiO** | 0.37 | 0.42 | 0.30 | 0.33 | 0.33 | 0.39 | 0.36 | 0.44 | 0.32 | 0.36 | 0.37 | 0.35 | 0.34 | 0.43 | 0.34 | 0.43 | 0.52 | 0.40 | 0.42 | 0.44 | 0.38 | 0.22 |
| **CaO** | 0.12 | 0.11 | 0.06 | 0.04 | 0.07 | 0.05 | 0.04 | 0.07 | 0.08 | 0.06 | 0.08 | 0.07 | 0.03 | 0.02 | 0.04 | 0.06 | 0.05 | 0.08 | 0.09 | 0.03 | 0.02 | 0.19 |
| **$Na_2O$** | 0.03 | 0.00 | 0.00 | 0.00 | 0.02 | 0.00 | 0.01 | 0.00 | 0.00 | 0.03 | 0.04 | 0.00 | 0.00 | 0.04 | 0.00 | 0.00 | 0.00 | 0.01 | 0.00 | 0.00 | 0.00 | 0.04 |
| **$K_2O$** | 0.00 | 0.00 | 0.00 | 0.02 | 0.00 | 0.00 | 0.00 | 0.03 | 0.00 | 0.01 | 0.05 | 0.00 | 0.00 | 0.02 | 0.02 | 0.00 | 0.00 | 0.00 | 0.03 | 0.01 | 0.00 | 0.00 |
| **Total** | **99.29** | **99.77** | **100.43** | **100.03** | **99.79** | **99.67** | **99.48** | **99.67** | **99.68** | **99.64** | **99.73** | **100.06** | **101.04** | **100.37** | **100.24** | **100.05** | **100.06** | **100.33** | **99.82** | **101.03** | **100.68** | **100.62** |
| **Si** | 1.02 | 1.02 | 1.01 | 1.01 | 1.01 | 1.01 | 1.02 | 1.01 | 1.01 | 1.02 | 1.01 | 1.01 | 1.01 | 1.01 | 1.01 | 1.01 | 1.01 | 1.00 | 1.00 | 1.01 | 1.01 | 1.01 |
| **Ti** | 0.00 | 0.00 | 0.00 | 0.00 | 0.00 | 0.00 | 0.00 | 0.00 | 0.00 | 0.00 | 0.00 | 0.00 | 0.00 | 0.00 | 0.00 | 0.00 | 0.00 | 0.00 | 0.00 | 0.00 | 0.00 | 0.00 |
| **Al** | 0.00 | 0.00 | 0.00 | 0.00 | 0.00 | 0.00 | 0.00 | 0.00 | 0.00 | 0.00 | 0.00 | 0.00 | 0.00 | 0.00 | 0.00 | 0.00 | 0.00 | 0.00 | 0.00 | 0.00 | 0.00 | 0.00 |
| **Cr** | 0.00 | 0.00 | 0.00 | 0.00 | 0.00 | 0.00 | 0.00 | 0.00 | 0.00 | 0.00 | 0.00 | 0.00 | 0.00 | 0.00 | 0.00 | 0.00 | 0.00 | 0.00 | 0.00 | 0.00 | 0.00 | 0.00 |
| **$Fe^{2+}$** | 0.21 | 0.20 | 0.20 | 0.20 | 0.20 | 0.20 | 0.20 | 0.20 | 0.20 | 0.20 | 0.20 | 0.20 | 0.20 | 0.20 | 0.20 | 0.20 | 0.18 | 0.18 | 0.20 | 0.21 | 0.20 | 0.31 |
| **Mn** | 0.00 | 0.00 | 0.00 | 0.00 | 0.00 | 0.00 | 0.00 | 0.00 | 0.00 | 0.00 | 0.00 | 0.00 | 0.00 | 0.00 | 0.00 | 0.00 | 0.00 | 0.00 | 0.00 | 0.00 | 0.00 | 0.01 |
| **Mg** | 1.75 | 1.76 | 1.77 | 1.76 | 1.78 | 1.77 | 1.76 | 1.77 | 1.77 | 1.76 | 1.77 | 1.77 | 1.77 | 1.77 | 1.78 | 1.77 | 1.79 | 1.80 | 1.78 | 1.76 | 1.77 | 1.66 |
| **Ni** | 0.01 | 0.01 | 0.01 | 0.01 | 0.01 | 0.01 | 0.01 | 0.01 | 0.01 | 0.01 | 0.01 | 0.01 | 0.01 | 0.01 | 0.01 | 0.01 | 0.01 | 0.01 | 0.01 | 0.01 | 0.01 | 0.00 |
| **Ca** | 0.00 | 0.00 | 0.00 | 0.00 | 0.00 | 0.00 | 0.00 | 0.00 | 0.00 | 0.00 | 0.00 | 0.00 | 0.00 | 0.00 | 0.00 | 0.00 | 0.00 | 0.00 | 0.00 | 0.00 | 0.00 | 0.01 |
| **Total** | **2.99** | **2.99** | **2.99** | **2.99** | **2.99** | **2.99** | **2.98** | **2.99** | **2.99** | **2.99** | **2.99** | **2.99** | **2.99** | **2.99** | **2.99** | **2.99** | **2.99** | **3.00** | **3.00** | **2.99** | **2.99** | **3.00** |
| **Fo** | 89.22 | 89.66 | 89.84 | 89.74 | 89.93 | 89.81 | 89.80 | 89.78 | 89.87 | 89.91 | 89.85 | 89.82 | 89.85 | 89.69 | 89.85 | 89.83 | 90.86 | 90.65 | 89.78 | 89.33 | 89.50 | 84.15 |
| **Fa** | 10.64 | 10.23 | 10.00 | 10.05 | 9.94 | 10.03 | 10.06 | 10.08 | 10.02 | 9.98 | 10.04 | 10.04 | 10.04 | 10.13 | 10.04 | 10.03 | 8.99 | 9.19 | 10.03 | 10.55 | 10.33 | 15.58 |
| **Tp** | 0.14 | 0.11 | 0.16 | 0.20 | 0.14 | 0.16 | 0.14 | 0.15 | 0.11 | 0.11 | 0.11 | 0.14 | 0.11 | 0.18 | 0.12 | 0.15 | 0.16 | 0.16 | 0.19 | 0.11 | 0.17 | 0.27 |

**Table 3.** Representative analyses of pyroxenes; a- clinopyroxenes.

| Rock type | | | | | Basanite | | | Latite | Lherzolite | | |
|---|---|---|---|---|---|---|---|---|---|---|---|
| Sample | Sot22 | | HOL32 | | | BIW88 | | BJM59A | BIW805 | | |
| Analyse | C6 | C6 | C1 | C1 | C1 | C5 (i) | C6 | C5 | C3 | C7(i) | C7(i) |
| **$SiO_2$** | 47.25 | 37.41 | 46.86 | 44.64 | 47.99 | 53.02 | 53.14 | 49.38 | 53.09 | 52.82 | 52.8 |
| **$TiO_2$** | 3.58 | 7.67 | 2.54 | 3.95 | 2.47 | 0.37 | 0.34 | 1.65 | 0.29 | 0.28 | 0.30 |
| **$Al_2O_3$** | 6.69 | 11.07 | 5.58 | 8.20 | 5.47 | 6.12 | 5.90 | 4.52 | 5.51 | 5.92 | 6.15 |
| **$Cr_2O_3$** | 0.03 | 0.00 | 0.08 | 0.42 | 0.12 | 0.80 | 0.78 | 0.13 | 0.70 | 0.00 | 0.00 |
| **FeO** | 8.85 | 12.02 | 7.20 | 7.19 | 6.89 | 2.33 | 2.40 | 10.73 | 2.41 | 2.41 | 2.44 |
| **MnO** | 0.26 | 0.23 | 0.09 | 0.11 | 0.21 | 0.09 | 0.03 | 0.22 | 0.13 | 0.03 | 0.14 |
| **MgO** | 10.82 | 8.25 | 13.38 | 11.84 | 13.63 | 14.50 | 14.68 | 13.69 | 14.82 | 14.8 | 14.86 |
| **CaO** | 21.37 | 19.86 | 23.19 | 22.74 | 22.86 | 22.11 | 22.09 | 18.82 | 21.44 | 21.68 | 20.98 |
| **$Na_2O$** | 0.79 | 0.89 | 0.44 | 0.56 | 0.42 | 1.73 | 1.61 | 0.52 | 1.66 | 1.65 | 1.70 |
| **$K_2O$** | 0.13 | 0.19 | 0.00 | 0.01 | 0.00 | 0.00 | 0.00 | 0.00 | 0.00 | 0.01 | 0.01 |
| **NiO** | 0.11 | 0.00 | 0.03 | 0.00 | 0.05 | 0.00 | 0.00 | 0.00 | 0.04 | 0.06 | 0.03 |
| **Total** | **99.88** | **97.59** | **99.39** | **99.66** | **100.11** | **101.07** | **100.97** | **99.66** | **100.09** | **99.66** | **99.41** |
| **Si** | 1.78 | 1.49 | 1.77 | 1.69 | 1.79 | 1.90 | 1.91 | 1.86 | 1.92 | 1.92 | 1.92 |
| **$Al^{IV}$** | 0.22 | 0.51 | 0.23 | 0.31 | 0.21 | 0.10 | 0.09 | 0.14 | 0.08 | 0.09 | 0.08 |
| **$Al^{VI}$** | 0.08 | 0.01 | 0.02 | 0.05 | 0.03 | 0.16 | 0.16 | 0.06 | 0.15 | 0.17 | 0.18 |
| **$Fe^{3+}$** | 0.00 | 0.18 | 0.14 | 0.10 | 0.09 | 0.03 | 0.02 | 0.04 | 0.01 | 0.03 | 0.01 |
| **Cr** | 0.00 | 0.00 | 0.00 | 0.01 | 0.00 | 0.02 | 0.02 | 0.00 | 0.02 | 0.00 | 0.00 |
| **Ti** | 0.10 | 0.23 | 0.07 | 0.11 | 0.07 | 0.01 | 0.01 | 0.05 | 0.01 | 0.01 | 0.01 |
| **$Fe^{2+}$** | 0.28 | 0.22 | 0.08 | 0.12 | 0.12 | 0.04 | 0.06 | 0.29 | 0.06 | 0.05 | 0.06 |
| **Mn** | 0.01 | 0.01 | 0.00 | 0.00 | 0.01 | 0.00 | 0.00 | 0.01 | 0.00 | 0.00 | 0.00 |
| **Mg** | 0.61 | 0.49 | 0.75 | 0.67 | 0.76 | 0.76 | 0.79 | 0.77 | 0.80 | 0.80 | 0.80 |
| **Ca** | 0.86 | 0.85 | 0.94 | 0.92 | 0.96 | 0.85 | 0.85 | 0.76 | 0.83 | 0.84 | 0.82 |
| **Na** | 0.06 | 0.07 | 0.03 | 0.04 | 0.03 | 0.12 | 0.11 | 0.04 | 0.12 | 0.12 | 0.12 |
| **K** | 0.01 | 0.01 | 0.00 | 0.00 | 0.00 | 0.00 | 0.00 | 0.00 | 0.00 | 0.00 | 0.00 |
| **SUM** | **4.00** | **4.06** | **4.05** | **4.03** | **4.03** | **4.01** | **4.01** | **4.01** | **4.00** | **4.01** | **4.01** |
| **$Fe^{2+}/(Fe^{2+}+Fe^{3+})$** | 0.99 | 0.54 | 0.37 | 0.55 | 0.56 | 0.62 | 0.79 | 0.88 | 0.84 | 0.64 | 0.81 |
| **XMg** | 0.69 | 0.70 | 0.90 | 0.84 | 0.86 | 0.95 | 0.93 | 0.72 | 0.93 | 0.95 | 0.93 |
| **Wo** | 47.52 | 46.87 | 48.08 | 49.56 | 47.54 | 46.740 | 46.68 | 39.76 | 45.57 | 45.97 | 44.88 |
| **En** | 33.48 | 27.09 | 38.61 | 35.91 | 39.44 | 42.66 | 43.17 | 40.25 | 43.83 | 43.67 | 44.23 |
| **Fs** | 15.81 | 22.24 | 11.66 | 12.32 | 11.44 | 3.99 | 4.00 | 18.00 | 4.21 | 4.03 | 4.31 |
| **Ac** | 3.18 | 3.80 | 1.65 | 2.21 | 1.58 | 6.62 | 6.16 | 1.99 | 6.39 | 6.33 | 6.58 |

**Table 3b.** Orthopyroxenes: (b) indicates border, (c) indicates core, and (i) indicates inclusion.

| Rock type | Basanite | | | | | | | | | | | | | Lherzolite | | | | | | | |
|---|---|---|---|---|---|---|---|---|---|---|---|---|---|---|---|---|---|---|---|---|---|
| Sample | MBA11 | BIW88A | | | | | | BIW88 | | | | | | | | | | BIW805 | | | |
| Analyses | C1 | C3(i) | C3-1 | C3(i) | C2 | C4 (b) | C4(c) | C4 | C5(b) | C5(c) | C6(b) | C6(c) | C1(b) | C1 (c) | C2(c) | C2 | C4(c) | C4(c) | C6 (b) | C6 (c) | C6 (c) | C6(i) |
| **$SiO_2$** | 55.70 | 55.96 | 57.63 | 57.27 | 56.17 | 56.00 | 56.07 | 55.61 | 56.00 | 55.08 | 56.12 | 56.11 | 56.07 | 56.10 | 55.73 | 55.48 | 55.91 | 55.77 | 56.3 | 56.46 | 54.96 | 55.51 |
| **$TiO_2$** | 0.10 | 0.06 | 0.03 | 0.05 | 0.06 | 0.06 | 0.06 | 0.05 | 0.07 | 0.17 | 0.05 | 0.06 | 0.05 | 0.04 | 0.06 | 0.06 | 0.04 | 0.04 | 0.05 | 0.04 | 0.04 | 0.06 |
| **$Al_2O_3$** | 4.71 | 3.66 | 2.50 | 2.59 | 3.93 | 4.11 | 4.15 | 4.44 | 3.94 | 4.96 | 3.82 | 4.13 | 3.38 | 3.55 | 4.23 | 4.18 | 3.57 | 3.54 | 3.04 | 3.15 | 5.05 | 5.05 |
| **$Cr_2O_3$** | 0.33 | 0.76 | 0.15 | 0.16 | 0.33 | 0.37 | 0.37 | 0.39 | 0.35 | 0.53 | 0.32 | 0.36 | 0.22 | 0.28 | 0.37 | 0.34 | 0.29 | 0.27 | 0.24 | 0.25 | 0.42 | 0.45 |
| **FeO** | 6.65 | 5.74 | 6.63 | 6.50 | 6.67 | 6.70 | 6.63 | 6.44 | 6.68 | 5.64 | 6.68 | 6.66 | 6.26 | 6.39 | 6.59 | 6.40 | 6.34 | 6.55 | 6.26 | 6.32 | 6.31 | 6.31 |
| **MnO** | 0.23 | 0.14 | 0.07 | 0.13 | 0.16 | 0.18 | 0.13 | 0.16 | 0.18 | 0.11 | 0.13 | 0.14 | 0.22 | 0.15 | 0.17 | 0.21 | 0.14 | 0.14 | 0.23 | 0.10 | 0.17 | 0.20 |
| **MgO** | 32.29 | 32.43 | 34.39 | 33.73 | 32.97 | 32.95 | 33.17 | 33.01 | 33.28 | 28.43 | 33.36 | 33.19 | 32.67 | 32.65 | 32.98 | 32.49 | 32.54 | 32.79 | 33.31 | 33.43 | 32.04 | 31.3 |
| **CaO** | 0.73 | 1.18 | 0.37 | 0.30 | 0.37 | 0.30 | 0.33 | 0.37 | 0.32 | 5.44 | 0.31 | 0.33 | 0.47 | 0.50 | 0.40 | 0.51 | 0.58 | 0.46 | 0.29 | 0.36 | 0.82 | 1.26 |
| **$Na_2O$** | 0.13 | 0.12 | 0.04 | 0.04 | 0.05 | 0.06 | 0.05 | 0.07 | 0.05 | 0.44 | 0.02 | 0.02 | 0.08 | 0.04 | 0.04 | 0.04 | 0.06 | 0.04 | 0.05 | 0.04 | 0.12 | 0.15 |
| **$K_2O$** | 0.00 | 0.01 | 0.00 | 0.00 | 0.00 | 0.00 | 0.00 | 0.00 | 0.00 | 0.01 | 0.00 | 0.00 | 0.00 | 0.00 | 0.00 | 0.00 | 0.00 | 0.00 | 0.03 | 0.01 | 0.02 | 0.01 |
| **NiO** | 0.14 | 0.08 | 0.13 | 0.11 | 0.11 | 0.08 | 0.09 | 0.11 | 0.11 | 0.08 | 0.06 | 0.09 | 0.07 | 0.06 | 0.10 | 0.08 | 0.10 | 0.10 | 0.11 | 0.12 | 0.07 | 0.04 |
| **TOTAL** | **101.01** | **100.14** | **101.94** | **100.88** | **100.82** | **100.81** | **101.05** | **100.65** | **100.98** | **100.89** | **100.87** | **101.09** | **99.49** | **99.76** | **100.67** | **99.79** | **99.57** | **99.7** | **99.91** | **100.28** | **100.02** | **100.34** |
| **Si** | 1.91 | 1.93 | 1.95 | 1.96 | 1.93 | 1.92 | 1.92 | 1.91 | 1.92 | 1.91 | 1.92 | 1.92 | 1.94 | 1.94 | 1.91 | 1.92 | 1.94 | 1.93 | 1.94 | 1.94 | 1.90 | 1.91 |
| **Al** | 0.09 | 0.07 | 0.05 | 0.04 | 0.08 | 0.08 | 0.08 | 0.09 | 0.08 | 0.09 | 0.08 | 0.08 | 0.06 | 0.06 | 0.09 | 0.08 | 0.06 | 0.07 | 0.06 | 0.06 | 0.10 | 0.09 |
| **Al** | 0.10 | 0.08 | 0.05 | 0.06 | 0.08 | 0.09 | 0.08 | 0.09 | 0.08 | 0.11 | 0.08 | 0.08 | 0.08 | 0.08 | 0.09 | 0.09 | 0.08 | 0.08 | 0.07 | 0.07 | 0.11 | 0.12 |
| **$Fe^{3+}$** | 0.00 | 0.00 | 0.00 | 0.00 | 0.00 | 0.00 | 0.00 | 0.00 | 0.00 | 0.00 | 0.00 | 0.00 | 0.00 | 0.00 | 0.00 | 0.00 | 0.00 | 0.00 | 0.00 | 0.00 | 0.00 | 0.00 |
| **Cr** | 0.01 | 0.02 | 0.00 | 0.00 | 0.01 | 0.01 | 0.01 | 0.01 | 0.01 | 0.02 | 0.01 | 0.01 | 0.01 | 0.01 | 0.01 | 0.01 | 0.01 | 0.01 | 0.01 | 0.01 | 0.01 | 0.01 |
| **Ti** | 0.00 | 0.00 | 0.00 | 0.00 | 0.00 | 0.00 | 0.00 | 0.00 | 0.00 | 0.00 | 0.00 | 0.00 | 0.00 | 0.00 | 0.00 | 0.00 | 0.00 | 0.00 | 0.00 | 0.00 | 0.00 | 0.00 |
| **$Fe^{2+}$** | 0.19 | 0.17 | 0.19 | 0.19 | 0.19 | 0.19 | 0.19 | 0.19 | 0.19 | 0.16 | 0.19 | 0.19 | 0.18 | 0.19 | 0.19 | 0.19 | 0.18 | 0.19 | 0.18 | 0.18 | 0.18 | 0.18 |
| **Mn** | 0.01 | 0.00 | 0.00 | 0.00 | 0.01 | 0.01 | 0.00 | 0.01 | 0.01 | 0.00 | 0.00 | 0.00 | 0.01 | 0.00 | 0.01 | 0.01 | 0.00 | 0.00 | 0.01 | 0.00 | 0.01 | 0.01 |
| **Mg** | 1.65 | 1.67 | 1.74 | 1.72 | 1.68 | 1.68 | 1.69 | 1.69 | 1.70 | 1.47 | 1.70 | 1.69 | 1.69 | 1.68 | 1.69 | 1.68 | 1.68 | 1.69 | 1.71 | 1.71 | 1.65 | 1.61 |
| **Ca** | 0.03 | 0.04 | 0.01 | 0.01 | 0.01 | 0.01 | 0.01 | 0.01 | 0.01 | 0.20 | 0.01 | 0.01 | 0.02 | 0.02 | 0.02 | 0.02 | 0.02 | 0.02 | 0.01 | 0.01 | 0.03 | 0.05 |
| **Na** | 0.01 | 0.01 | 0.00 | 0.00 | 0.00 | 0.00 | 0.00 | 0.01 | 0.00 | 0.03 | 0.00 | 0.00 | 0.01 | 0.00 | 0.00 | 0.00 | 0.00 | 0.00 | 0.00 | 0.00 | 0.01 | 0.01 |
| **K** | 0.00 | 0.00 | 0.00 | 0.00 | 0.00 | 0.00 | 0.00 | 0.00 | 0.00 | 0.00 | 0.00 | 0.00 | 0.00 | 0.00 | 0.00 | 0.00 | 0.00 | 0.00 | 0.00 | 0.00 | 0.00 | 0.00 |
| **SUM** | **3.99** | **3.99** | **4.00** | **3.99** | **3.99** | **3.99** | **4.00** | **4.00** | **4.00** | **4.00** | **4.00** | **3.99** | **4.00** | **3.99** | **4.00** | **3.99** | **3.99** | **3.99** | **3.99** | **3.99** | **4.00** | **3.98** |
| **$Fe^{2+}/(Fe^{2+}+Fe^{3+})$** | 1.00 | 1.00 | 1.00 | 1.00 | 1.00 | 1.00 | 1.00 | 1.00 | 1.00 | 1.00 | 1.00 | 1.10 | 1.00 | 1.00 | 1.00 | 1.00 | 1.00 | 1.00 | 1.00 | 1.00 | 1.00 | 1.00 |
| **XMg** | 0.90 | 0.91 | 0.90 | 0.90 | 0.90 | 0.90 | 0.90 | 0.90 | 0.90 | 0.90 | 0.90 | 0.90 | 0.90 | 0.90 | 0.90 | 0.90 | 0.90 | 0.90 | 0.90 | 0.90 | 0.90 | 0.90 |
| **Wo** | 1.42 | 2.31 | 0.69 | 0.57 | 0.72 | 0.58 | 0.64 | 0.72 | 0.61 | 10.82 | 0.60 | 0.64 | 0.92 | 0.98 | 0.77 | 1.00 | 1.14 | 0.90 | 0.56 | 0.69 | 1.62 | 2.51 |
| **En** | 87.62 | 88.26 | 89.40 | 89.40 | 88.77 | 88.79 | 89.00 | 89.04 | 88.92 | 78.66 | 89.12 | 89.04 | 88.87 | 88.86 | 88.86 | 88.71 | 88.71 | 88.78 | 89.47 | 89.51 | 87.96 | 86.78 |
| **Fs** | 10.49 | 9.00 | 9.78 | 9.89 | 10.34 | 10.42 | 10.19 | 10.00 | 10.29 | 8.94 | 10.22 | 10.25 | 9.92 | 10.02 | 10.23 | 10.15 | 9.94 | 10.18 | 9.80 | 9.66 | 9.99 | 10.17 |
| **Ac** | 0.46 | 0.43 | 0.14 | 0.14 | 0.18 | 0.21 | 0.17 | 0.25 | 0.17 | 1.58 | 0.07 | 0.07 | 0.28 | 0.14 | 0.14 | 0.14 | 0.21 | 0.14 | 0.18 | 0.14 | 0.43 | 0.54 |

**Table 4.** Representative analysis of spinels. FeO and $Fe_2O_3$ have been recalculated from analytic microprobe FeOt; (b) indicates border, (c) indicates core, and (i) indicates inclusion.

| Rock type | Basanite | | | | | | | | | | Latite | | | | | | | Lherzolite | | | | | |
|---|---|---|---|---|---|---|---|---|---|---|---|---|---|---|---|---|---|---|---|---|---|---|---|
| Sample | Sot22 | | HOL32 | | | BIW88A | | MBA11 | | | SAF88 | BJM59A | | | | | | BIW805 | | | | BIW88 | |
| Comment | C5 | C6(b) | C6 | C1(i) | C3 | C5 | C4 | C5 | C1 | C1(b) | C1(c) | C3 | C4 | C5 | C2 | C2 | C4 | C4 (c) | C6 (b) | C7 | C3 | C1 | C2 |
| **$SiO_2$** | 0.00 | 0.14 | 0.01 | 0.09 | 0.09 | 0.00 | 0.07 | 0.11 | 0.05 | 0.02 | 0.00 | 0.01 | 0.04 | 0.72 | 0.02 | 0.00 | 0.01 | 0.01 | 0.04 | 0.02 | 0.03 | 8.52 | 0.02 |
| **$TiO_2$** | 20.11 | 21.05 | 20.77 | 22.76 | 0.00 | 24.72 | 24.54 | 1.85 | 21.48 | 21.03 | 0.05 | 23.76 | 4.94 | 46.88 | 0.00 | 0.03 | 0.01 | 0.02 | 0.01 | 0.00 | 0.00 | 3.39 | 0.07 |
| **$Al_2O_3$** | 6.73 | 6.01 | 7.07 | 5.95 | 37.78 | 4.13 | 4.10 | 28.62 | 2.45 | 4.46 | 43.07 | 2.83 | 0.72 | 0.12 | 55.33 | 55.39 | 55.52 | 55.61 | 55.87 | 55.26 | 56.84 | 32.38 | 54.47 |
| **$Cr_2O_3$** | 0.67 | 0.50 | 0.64 | 1.43 | 28.56 | 0.40 | 0.31 | 24.73 | 0.91 | 1.92 | 21.67 | 0.12 | 0.01 | 0.04 | 9.51 | 9.77 | 9.45 | 9.57 | 9.06 | 9.43 | 10.26 | 13.69 | 9.57 |
| **$V_2O_3$** | 0.19 | 0.17 | - | - | 0.02 | - | - | - | - | - | - | - | - | - | - | - | - | - | - | - | - | - | 0.00 |
| **FeO** | 42.86 | 44.66 | 40.65 | 44.63 | 10.28 | 47.10 | 46.83 | 19.61 | 44.42 | 42.71 | 17.05 | 46.25 | 58.02 | 42.39 | 8.69 | 8.79 | 8.34 | 8.64 | 8.54 | 8.81 | 9.43 | 25.73 | 11.48 |
| **$Fe_2O_3$c** | 23.63 | 20.75 | 22.79 | 19.31 | 4.41 | 18.66 | 19.08 | 12.33 | 25.29 | 23.47 | 2.85 | 22.68 | 35.01 | 0.00 | 4.08 | 3.65 | 4.27 | 3.91 | 3.94 | 4.10 | 2.21 | 0.00 | 4.09 |
| **MnO** | 0.63 | 0.50 | 0.48 | 0.63 | 0.15 | 0.80 | 0.76 | 0.42 | 0.85 | 0.70 | 0.38 | 0.78 | 0.57 | 5.93 | 0.06 | 0.08 | 0.16 | 0.11 | 0.09 | 0.07 | 0.08 | 0.32 | 0.24 |
| **MgO** | 4.74 | 3.84 | 6.47 | 5.29 | 17.89 | 4.50 | 4.63 | 11.73 | 3.82 | 5.03 | 13.76 | 4.40 | 0.00 | 0.01 | 20.52 | 20.46 | 20.78 | 20.63 | 20.68 | 20.42 | 20.33 | 11.56 | 18.61 |
| **CaO** | 0.00 | 0.06 | 0.20 | 0.01 | 0.00 | 0.03 | 0.06 | 0.04 | 0.16 | 0.08 | 0.00 | 0.11 | 0.01 | 0.95 | 0.03 | 0.00 | 0.00 | 0.00 | 0.03 | 0.00 | 0.00 | 2.30 | 0.01 |
| **ZnO** | 0.01 | 0.00 | - | - | 0.00 | - | - | - | - | - | - | - | - | - | - | - | - | - | - | - | - | - | 0.01 |
| **$Na_2O$** | 0.06 | 0.02 | 0.06 | 0.04 | 0.01 | 0.02 | 0.00 | 0.00 | 0.00 | 0.00 | 0.01 | 0.07 | 0.00 | 0.00 | 0.00 | 0.00 | 0.00 | 0.00 | 0.03 | 0.00 | 0.00 | 0.75 | 0.02 |
| **K2O** | 0.00 | 0.04 | 0.03 | 0.00 | 0.00 | 0.02 | 0.00 | 0.01 | 0.05 | 0.00 | 0.00 | 0.02 | 0.00 | 0.02 | 0.02 | 0.00 | 0.00 | 0.00 | 0.00 | 0.00 | 0.00 | 0.07 | 0.00 |
| **NiO** | 0.09 | 0.06 | 0.14 | 0.08 | 0.27 | 0.06 | 0.12 | 0.07 | 0.12 | 0.01 | 0.34 | 0.04 | 0.06 | 0.00 | 0.36 | 0.35 | 0.41 | 0.37 | 0.44 | 0.36 | 0.34 | 0.25 | 0.36 |
| **BaO** | 0.03 | 0.00 | - | - | 0.59 | - | - | - | - | - | - | - | - | - | - | - | - | - | - | - | - | - | 0.09 |
| **Total** | **99.76** | **97.80** | **99.30** | **100.22** | **100.05** | **100.44** | **100.50** | **99.52** | **99.60** | **99.43** | **99.18** | **101.06** | **99.38** | **97.06** | **98.62** | **98.52** | **98.95** | **98.87** | **98.74** | **98.47** | **99.52** | **98.96** | **99.04** |
| Si | 0.00 | 0.04 | 0.00 | 0.03 | 0.02 | 0.00 | 0.02 | 0.03 | 0.01 | 0.01 | 0.00 | 0.00 | 0.01 | 0.22 | 0.00 | 0.00 | 0.00 | 0.00 | 0.01 | 0.00 | 0.01 | 2.01 | 0.00 |
| **Ti** | 4.27 | 4.59 | 4.37 | 4.80 | 0.00 | 5.27 | 5.23 | 0.34 | 4.70 | 4.51 | 0.01 | 5.08 | 1.14 | 10.90 | 0.00 | 0.00 | 0.00 | 0.00 | 0.00 | 0.00 | 0.00 | 0.60 | 0.01 |
| **Al** | 2.24 | 2.05 | 2.33 | 1.97 | 10.09 | 1.38 | 1.37 | 8.23 | 0.84 | 1.50 | 11.58 | 0.95 | 0.26 | 0.04 | 13.76 | 13.78 | 13.75 | 13.78 | 13.85 | 13.76 | 13.95 | 9.02 | 13.70 |
| **Cr** | 0.15 | 0.11 | 0.14 | 0.32 | 5.12 | 0.09 | 0.07 | 4.77 | 0.21 | 0.43 | 3.91 | 0.03 | 0.00 | 0.01 | 1.59 | 1.63 | 1.57 | 1.59 | 1.51 | 1.58 | 1.69 | 2.56 | 1.61 |
| **V** | 0.04 | 0.04 | 0.00 | 0.00 | 0.00 | 0.00 | 0.00 | 0.00 | 0.00 | 0.00 | 0.00 | 0.00 | 0.00 | 0.00 | 0.00 | 0.00 | 0.00 | 0.00 | 0.00 | 0.00 | 0.00 | 0.00 | 0.00 |
| **$Fe^{3+}$** | 5.02 | 4.53 | 4.79 | 4.07 | 0.75 | 3.98 | 4.07 | 2.26 | 5.53 | 5.04 | 0.49 | 4.85 | 13.43 | 0.00 | 0.65 | 0.58 | 0.67 | 0.62 | 0.62 | 0.65 | 0.35 | 0.00 | 0.66 |
| **$Fe^{2+}$** | 10.12 | 10.83 | 9.50 | 10.46 | 1.95 | 11.17 | 11.09 | 4.00 | 10.80 | 10.18 | 3.25 | 11.00 | 9.00 | 10.96 | 1.53 | 1.55 | 1.47 | 1.52 | 1.50 | 1.56 | 1.68 | 5.09 | 2.05 |
| **Mn** | 0.15 | 0.12 | 0.11 | 0.15 | 0.03 | 0.19 | 0.18 | 0.09 | 0.21 | 0.17 | 0.07 | 0.19 | 0.15 | 1.55 | 0.01 | 0.01 | 0.03 | 0.02 | 0.02 | 0.01 | 0.01 | 0.06 | 0.04 |
| **Mg** | 2.00 | 1.66 | 2.70 | 2.21 | 6.04 | 1.90 | 1.96 | 4.27 | 1.66 | 2.14 | 4.68 | 1.87 | 0.00 | 0.00 | 6.45 | 6.44 | 6.51 | 6.47 | 6.48 | 6.43 | 6.31 | 4.07 | 5.92 |
| **Ca** | 0.00 | 0.02 | 0.06 | 0.00 | 0.00 | 0.01 | 0.02 | 0.01 | 0.05 | 0.02 | 0.00 | 0.03 | 0.00 | 0.31 | 0.01 | 0.00 | 0.00 | 0.00 | 0.01 | 0.00 | 0.00 | 0.58 | 0.00 |
| **Zn** | 0.00 | 0.00 | 0.00 | 0.00 | 0.00 | 0.00 | 0.00 | 0.00 | 0.00 | 0.00 | 0.00 | 0.00 | 0.00 | 0.00 | 0.00 | 0.00 | 0.00 | 0.00 | 0.00 | 0.00 | 0.00 | 0.00 | 0.00 |
| **SUM** | **24.00** | **24.00** | **24.00** | **24.00** | **24.00** | **24.00** | **24.00** | **24.00** | **24.00** | **24.00** | **24.00** | **24.00** | **24.00** | **24.00** | **24.00** | **24.00** | **24.00** | **24.00** | **24.00** | **24.00** | **24.00** | **24.00** | **24.00** |
| **Fe/Fe+Mg** | 0.88 | 0.90 | 0.84 | 0.87 | 0.31 | 0.89 | 0.89 | 0.59 | 0.91 | 0.88 | 0.44 | 0.89 | 1.00 | 1.00 | 0.25 | 0.25 | 0.25 | 0.25 | 0.25 | 0.26 | 0.24 | 0.56 | 0.31 |
| **Cr/Cr+Al** | 0.06 | 0.05 | 0.06 | 0.14 | 0.34 | 0.06 | 0.05 | 0.37 | 0.20 | 0.22 | 0.25 | 0.03 | 0.01 | 0.18 | 0.10 | 0.11 | 0.10 | 0.10 | 0.10 | 0.10 | 0.11 | 0.22 | 0.11 |
| **$Fe^{2+}/Fe^{3+}$** | 2.02 | 2.39 | 1.98 | 2.57 | 2.59 | 2.80 | 2.73 | 1.77 | 1.95 | 2.02 | 6.66 | 2.27 | 0.67 | - | 2.36 | 2.68 | 2.17 | 2.45 | 2.41 | 2.39 | 4.85 | #DIV/0! | 3.12 |
| **Mg#** | 9.96 | 7.92 | 13.73 | 10.60 | 63.50 | 8.72 | 9.00 | 37.43 | 7.92 | 10.54 | 44.66 | 8.69 | 0.00 | 0.02 | 70.26 | 69.95 | 71.35 | 70.48 | 70.77 | 69.85 | 68.31 | 31.00 | 61.86 |

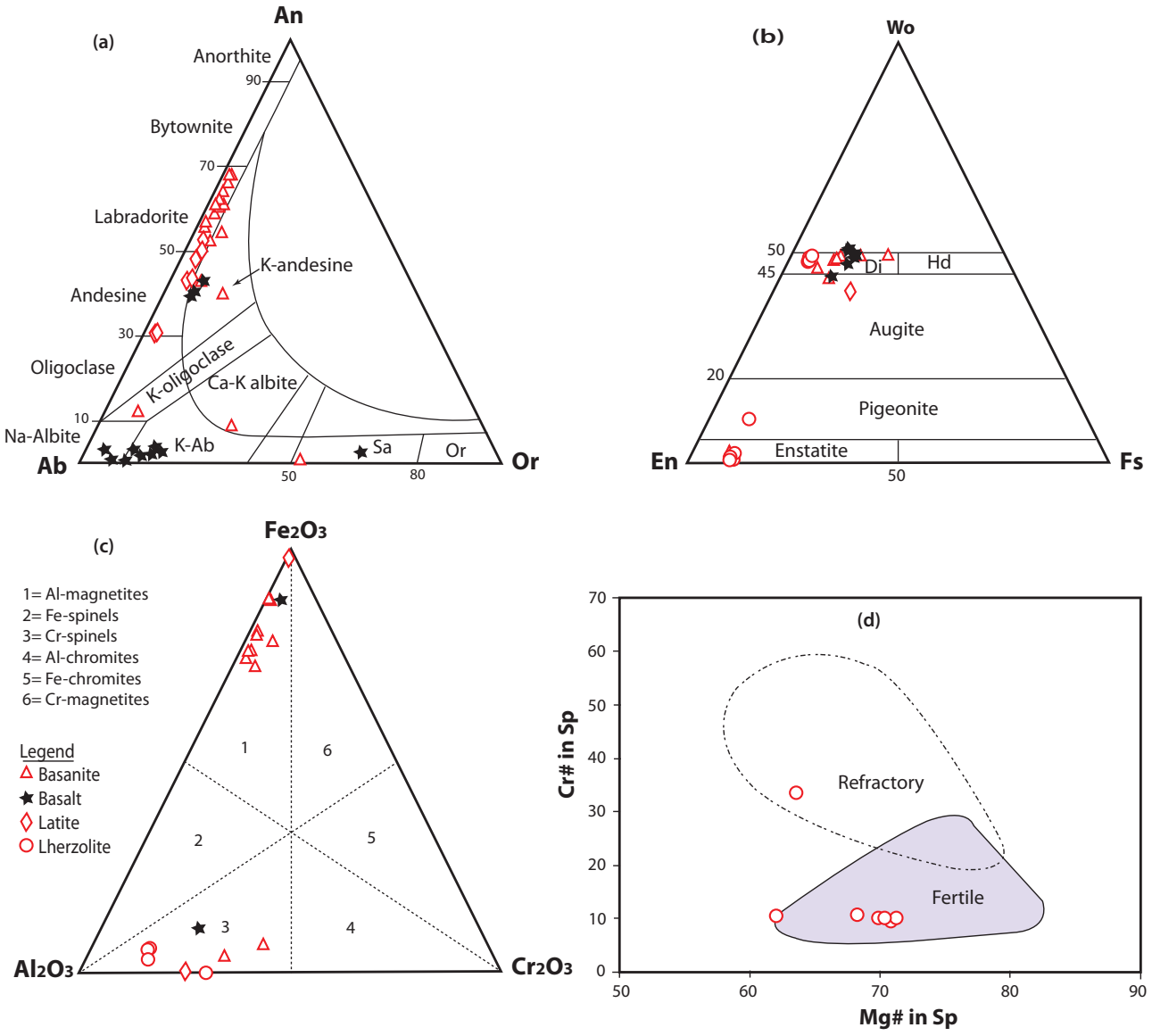


**Fig. 3.** Chemical composition of the main mineral phases of the Bini lavas and hosted spinel lherzolites: (a) representative feldspars in the ternary An–Ab–Or diagram of Smith and Brown (1988); (b) Analyzed clinopyroxenes in the ternary Wo–En–Fs diagram of Morimoto *et al.* (1988); (c) Ti–Fe oxides in the ternary $Fe_2O_3$–$Al_2O_3$–$Cr_2O_3$ diagram of Stevens (1944); (d) Spinels Cr# versus Mg# diagram, the refractory and fertile peridotite fields are from Bian *et al.* (2024). Some data of feldspars and pyroxenes from Tiabou *et al.* (2019) were also used for these diagrams (in black color). For mineral symbols: Ab, albite; An, anorthite; Sa, sanidine; Or, orthoclase; En, enstatite; Di, diopside; Fs, ferrosilite; Wo, wollastonite; Hd, hedenbergite; Sp, spinel.

### 4.2.2 Olivine

Olivine crystals from lavas ($Fo_{70.9–90.4}$) display higher FeO (8.7–25.7 wt%), CaO (0–0.4 wt%), and MnO (0.1–0.6 wt%) but lower MgO (35.8–49.6 wt%) and NiO (0.1–0.5 wt%) contents than those in hosted spinel lherzolites (FeO: 9.5–10.2 wt%; MnO: 0.1–0.2 wt%; CaO: 0–0.1 wt%; NiO: 0.3–0.4 wt%; MgO: 47.4–49.1 wt%), which are slightly more forsteritic ($Fo_{89.2–91}$ against $Fo_{71–91}$) with lower Fo deviation (~2 mol%) (Tab. 2). Compositions of olivine xenocrysts present in basanite samples BIW88 and BIW88A (FeO: 8.7–14.6 wt%; CaO: 0–0.2 wt%; MnO: 0.1–0.3 wt%; MgO: 44.7–49.2 wt%; NiO: 0.2–0.5 wt%) are somewhat comparable with those in lherzolites, although one crystal displays lower forsterite content ($Fo_{84.2}$). The Fo contents of Bini Warack lherzolitic olivines fit with the composition of SCLM olivines (Arai, 1994). Referring to their CaO content range, olivine grains from lavas are mostly of magmatic origin (CaO >0.1 wt%), contrary to those in hosted spinel-bearing lherzolites, which are of residual origin (mostly CaO <0.1 wt%), according to Thompson and Gibson (2000). Overall, olivine of spinel lherzolites from Bini Warack displays similar compositions to those of mantle xenoliths from the northern Kapsiki (Tamen *et al.*, 2015) and are more variable compared to those of Nyos (Temdjim *et al.*, 2004), Mount Cameroon (Suh *et al.*, 2008), Kumba (Lee *et al.*, 1996; Teitchou *et al.*, 2007), and São Tomé (Caldeira and Munha, 2002). The

**Table 5.** Whole-rock chemical analyses of 21 representative host lavas: 6 from this study (italic bold) and 15 from Tiabou *et al.* (2019).

| Rock type | | | | | Basanite | | | | | | |
|---|---|---|---|---|---|---|---|---|---|---|---|
| Sample | BIW 88A | HOL 32 | SAF 88 | SOT 22 | MBA 11 | PK8 | PK3 | BA19 | BA20 | BA50 | BA5 |
| $SiO_2$ | ***40.84*** | ***41.5*** | ***41.86*** | ***42.38*** | ***43.47*** | 42.79 | 42.84 | 39.2 | 41.99 | 41.68 | 42.68 |
| $TiO_2$ | ***3.50*** | ***2.87*** | ***3.70*** | ***2.82*** | ***2.49*** | 2.99 | 3.01 | 3.01 | 3.16 | 3.16 | 3.16 |
| $Al_2O_3$ | ***12.59*** | ***11.98*** | ***13.94*** | ***12.4*** | ***12.6*** | 13.88 | 13.29 | 11.49 | 12.89 | 12.87 | 12.82 |
| $Fe_2O_3$ | ***13.18*** | ***12.42*** | ***13.96*** | ***12.61*** | ***11.05*** | 12.06 | 11.99 | 13.9 | 14.32 | 13.99 | 14.22 |
| MnO | ***0.19*** | ***0.19*** | ***0.22*** | ***0.19*** | ***0.16*** | 0.20 | 0.19 | 0.22 | 0.28 | 0.24 | 0.19 |
| MgO | ***10.62*** | ***11.35*** | ***7.47*** | ***11.36*** | ***13.37*** | 7.69 | 7.63 | 8.14 | 7.15 | 7.16 | 7.21 |
| CaO | ***10.67*** | ***11.22*** | ***9.44*** | ***10.71*** | ***8.33*** | 9.88 | 9.89 | 12.31 | 9.33 | 9.31 | 8.93 |
| $Na_2O$ | ***2.57*** | ***1.83*** | ***3.35*** | ***2.58*** | ***2.74*** | 3.30 | 3.29 | 3.99 | 4.35 | 4.47 | 4.29 |
| $K_2O$ | ***1.38*** | ***1.60*** | ***1.98*** | ***1.72*** | ***1.53*** | 1.29 | 1.33 | 2.03 | 2.27 | 2.37 | 2.27 |
| $P_2O_5$ | ***0.92*** | ***0.92*** | ***1.46*** | ***0.92*** | ***0.71*** | 1.16 | 1.20 | 1.39 | 1.44 | 1.44 | 1.43 |
| TOTAL (wt.%) | ***96.46*** | ***95.88*** | ***97.38*** | ***97.69*** | ***96.45*** | 95.24 | 94.66 | 95.68 | 97.18 | 96.69 | 97.20 |
| LOI | ***2.66*** | ***3.30*** | ***1.78*** | ***1.25*** | ***2.58*** | 4.77 | 4.74 | 4.65 | 2.77 | 2.85 | 2.73 |
| Mg# | ***61.48*** | ***64.41*** | ***51.48*** | ***64.08*** | ***70.56*** | 55.80 | 55.80 | 53.70 | 49.70 | 50.3 | 50.10 |
| DI | ***23.65*** | ***21.28*** | ***33.63*** | ***25.14*** | ***28.9*** | 32.16 | 32.82 | 29.32 | 38.18 | 38.84 | 39.39 |
| **Traces (ppm)** | | | | | | | | | | | |
| Cs | ***0.38*** | ***0.57*** | ***0.48*** | ***0.47*** | ***0.55*** | 1.00 | 1.00 | 1.00 | 1.00 | 1.00 | 1.00 |
| Rb | ***37.44*** | ***42.48*** | ***53.31*** | ***42.81*** | ***48.81*** | 37.00 | 45.00 | 54.00 | 58.00 | 62.00 | 61.00 |
| Ba | ***491.75*** | ***708.48*** | ***648.23*** | ***713.95*** | ***684.35*** | 881.00 | 950.00 | 990.00 | 1111.00 | 979.00 | 975.00 |
| Sr | ***944.17*** | ***894.01*** | ***1340.06*** | ***1093.67*** | ***1018.6*** | 1230 | 1213.00 | 1377.00 | 889.00 | 1401 | 797.00 |
| Pb | ***3.17*** | ***3.62*** | ***4.59*** | ***3.66*** | ***3.73*** | 7.00 | 7.00 | 25.00 | 29.00 | 33.00 | 32.00 |
| Th | ***7.54*** | ***7.87*** | ***10.30*** | ***8.18*** | ***8.10*** | 9.00 | 11.00 | 17.00 | 19.00 | 19.00 | 19.00 |
| U | ***1.96*** | ***1.97*** | ***2.77*** | ***2.05*** | ***1.92*** | 1.00 | 1.00 | 4.00 | 4.00 | 4.00 | 4.00 |
| Zr | ***330.5*** | ***288.05*** | ***530.02*** | ***286.76*** | ***232.26*** | 349.00 | 352.00 | 427.00 | 401.00 | 348.00 | 339.00 |
| Hf | ***7.36*** | ***6.21*** | ***11.15*** | ***6.20*** | ***4.96*** | 6.00 | 6.00 | 8.00 | 8.00 | 8.00 | 8.00 |
| Ta | ***6.01*** | ***5.67*** | ***8.12*** | ***5.68*** | ***5.13*** | 3.00 | 3.00 | 8.00 | 8.00 | 8.00 | 8.00 |
| Y | ***27.8*** | ***26.08*** | ***34.38*** | ***25.13*** | ***20.10*** | 23.00 | 31.00 | 34.00 | 37.00 | 40.00 | 35.00 |
| Nb | ***85.64*** | ***82.39*** | ***110.28*** | ***82.66*** | ***76.82*** | 89.00 | 92.00 | 151.00 | 142.00 | 133.00 | 137.00 |
| Sc | ***22.96*** | ***25.76*** | ***14.50*** | ***24.87*** | ***17.58*** | 22.00 | 24.00 | 16.00 | 13.00 | 14.00 | 14.00 |
| Cr | ***357.56*** | ***431.6*** | ***143.48*** | ***516.77*** | ***645.61*** | 179.00 | 188.00 | 120.00 | 121.00 | 118.00 | 119.00 |
| Ni | ***249.75*** | ***245.95*** | ***95.16*** | ***294.44*** | ***476.49*** | 169.00 | 175.00 | 110.00 | 93.00 | 105.00 | 103.00 |
| Co | ***53.58*** | ***53.27*** | ***40.69*** | ***53.67*** | ***54.62*** | 29.00 | 38.00 | 46.00 | 44.00 | 45.00 | 39.00 |
| V | ***235.8*** | ***214.98*** | ***175.43*** | ***211.28*** | ***182.31*** | 221.00 | 219.00 | 225.00 | 224.00 | 222.00 | 219.00 |
| W | ***2.36*** | ***2.19*** | ***1.89*** | ***3.12*** | ***2.61*** | 1.00 | 1.00 | 2.00 | 2.00 | 2.00 | 1.00 |
| Ga | ***20.15*** | ***18.24*** | ***25.61*** | ***18.63*** | ***17.18*** | 22.00 | 29.00 | 22.00 | 26.00 | 28.00 | 24.00 |
| Zn | ***119.29*** | ***111.84*** | ***173.8*** | ***110.40*** | ***97.84*** | 109.00 | 118.00 | 130.00 | 131.00 | 113.00 | 116.00 |
| Cu | ***38.46*** | ***46.90*** | ***24.22*** | ***46.96*** | ***38.84*** | 26.00 | 37.00 | 40.00 | 60.00 | 58.00 | 56.00 |
| La | ***60.94*** | ***61.44*** | ***87.25*** | ***60.84*** | ***60.27*** | 77.00 | 89.00 | 125.00 | 130.00 | 133.00 | 131.00 |
| Ce | ***122.45*** | ***120.48*** | ***175.05*** | ***118.92*** | ***110.56*** | 160.00 | 164.00 | 222.00 | 221.00 | 226.00 | 231.00 |
| Pr | ***14.14*** | ***13.72*** | ***20.35*** | ***13.39*** | ***11.76*** | 10.00 | 10.00 | 23.00 | 23.00 | 23.00 | 22.00 |
| Nd | ***55.31*** | ***53.90*** | ***80.30*** | ***52.13*** | ***43.75*** | 67.00 | 70.00 | 83.00 | 82.00 | 79.00 | 77.00 |
| Sm | ***10.85*** | ***10.21*** | ***15.48*** | ***9.84*** | ***7.69*** | 7.00 | 8.00 | 14.00 | 14.00 | 15.00 | 15.00 |
| Eu | ***3.41*** | ***3.20*** | ***4.75*** | ***3.07*** | ***2.42*** | 2.00 | 2.00 | 4.00 | 4.00 | 4.00 | 4.00 |

**Table 5.** (continued).

| Rock type | | | | | Basanite | | | | | | |
|---|---|---|---|---|---|---|---|---|---|---|---|
| Sample | BIW 88A | HOL 32 | SAF 88 | SOT 22 | MBA 11 | PK8 | PK3 | BA19 | BA20 | BA50 | BA5 |
| Gd | ***8.82*** | ***8.01*** | ***11.85*** | ***7.75*** | ***6.07*** | 7.00 | 7.00 | 11.00 | 10.00 | 10.00 | 11.00 |
| Tb | ***1.20*** | ***1.08*** | ***1.57*** | ***1.05*** | ***0.82*** | 1.00 | 1.00 | 1.00 | 2.00 | 2.00 | 2.00 |
| Dy | ***6.28*** | ***5.78*** | ***8.03*** | ***5.63*** | ***4.40*** | 5.00 | 5.00 | 8.00 | 8.00 | 8.00 | 7.00 |
| Ho | ***1.13*** | ***1.04*** | ***1.38*** | ***1.01*** | ***0.79*** | 1.00 | 2.00 | 1.00 | 1.00 | 1.00 | 1.00 |
| Er | ***2.62*** | ***2.44*** | ***3.10*** | ***2.39*** | ***1.87*** | 2.00 | 3.00 | 3.00 | 3.00 | 3.00 | 3.00 |
| Tm | ***0.34*** | ***0.33*** | ***0.39*** | ***0.32*** | ***0.25*** | 0.00 | 0.00 | 0.00 | 0.00 | 0.00 | 0.00 |
| Yb | ***2.00*** | ***1.92*** | ***2.27*** | ***1.88*** | ***1.47*** | 3.00 | 3.00 | 2.00 | 2.00 | 3.00 | 3.00 |
| Lu | ***0.28*** | ***0.27*** | ***0.31*** | ***0.27*** | ***0.22*** | 0.00 | 0.00 | 0.00 | 0.00 | 0.00 | 0.00 |
| Eu/Eu* | ***1.06*** | ***1.08*** | ***1.07*** | ***1.07*** | ***1.08*** | 0.87 | 0.82 | 0.98 | 1.03 | 1.00 | 0.95 |
| **Norm CIPW** | | | | | | | | | | | |
| Orthose | ***8.55*** | ***10.00*** | ***12.19*** | ***10.54*** | ***9.44*** | 8.09 | 8.40 | - | 13.99 | 14.67 | 13.98 |
| Albite | ***5.99*** | ***5.33*** | ***11.94*** | ***5.18*** | ***13.8*** | 17.45 | 18.13 | - | 7.44 | 5.91 | 10.72 |
| Anorthite | ***19.69*** | ***20.83*** | ***17.84*** | ***17.79*** | ***18.44*** | 20.44 | 18.77 | 7.88 | 9.32 | 8.44 | 9.40 |
| Leucite | - | - | - | - | - | - | - | 9.96 | - | - | - |
| Nepheline | ***9.11*** | ***5.95*** | ***9.50*** | ***9.42*** | ***5.66*** | 6.61 | 6.29 | 19.36 | 16.76 | 18.27 | 14.69 |
| Diopside | ***23.87*** | ***25.45*** | ***17.12*** | ***25.03*** | ***16.01*** | 19.19 | 20.58 | 35.76 | 23.95 | 24.71 | 22.21 |
| Larnite | - | - | - | - | - | - | - | 2.08 | - | - | - |
| Olivine | ***21.20*** | ***22.19*** | ***18.09*** | ***22.02*** | ***27.98*** | 17.12 | 16.54 | 12.95 | 16.24 | 15.70 | 16.74 |
| Magnetite | ***2.39*** | ***2.26*** | ***2.51*** | ***2.26*** | ***2.00*** | 2.21 | 2.21 | 2.54 | 2.58 | 2.53 | 2.56 |
| Ilmenite | ***6.97*** | ***5.74*** | ***7.31*** | ***5.55*** | ***4.95*** | 6.03 | 6.11 | 6.05 | 6.26 | 6.29 | 6.25 |
| Apatite | ***2.24*** | ***2.25*** | ***3.52*** | ***2.21*** | ***1.72*** | 2.85 | 2.97 | 3.41 | 3.48 | 3.50 | 3.45 |
| $^{87}Sr/^{86}Sr$ | | ***0.70312*** | ***0.70299*** | ***0.70321*** | ***0.70305*** | | | | | | |
| $2\sigma.10^{-6}$ | | ***5.00*** | ***5.00*** | ***5.00*** | ***4.00*** | | | | | | |
| $^{143}Nd/^{144}Nd$ | | ***0.512891*** | ***0.512927*** | ***0.512867*** | ***0.512862*** | | | | | | |
| $2\sigma.10^{-6}$ | | ***4.00*** | ***4.00*** | ***4.00*** | ***3.00*** | | | | | | |
| $^{145}Sm/^{144}Sm$ | | ***0.348404*** | ***0.348413*** | ***0.348415*** | ***0.348407*** | | | | | | |
| $2\sigma.10^{-6}$ | ***3.00*** | ***3.00*** | ***3.00*** | ***2.00*** | | | | | | | |
| $^{87}Rb/^{86}Rb$ | | ***0.133446*** | ***0.109633*** | ***0.109929*** | ***0.134577*** | | | | | | |
| $^{147}Sm/^{144}Sm$ | ***0.110572*** | ***0.112502*** | ***0.110136*** | ***0.102566*** | | | | | | | |
| $(^{87}Sr/^{86}Sr)Ma(^{143}Nd/^{144}Nd)Ma$ | | ***0.7031160.512888*** | ***0.7029870.512924*** | ***0.7032060.512864*** | ***0.7030510.512859*** | | | | | | |
| $^{147}Sm/^{144}Sm$ | | ***0.110572*** | ***0.112502*** | ***0.110136*** | ***0.102566*** | | | | | | |
| εNdi | ***5.11*** | ***5.81*** | ***4.64*** | ***4.54*** | | | | | | | |

**Table 6.** Whole-rock chemical analyses of the studied mantle xenoliths.

| Rock type | Lherzolite | | | | | |
|---|---|---|---|---|---|---|
| sample | BIW 88E | BIW 88-2 | BIW 88-1 | BIW 88-3 | BIW 88-5 | BIW 88-4 |
| $SiO_2$ | 45.23 | 44.62 | 43.83 | 44.29 | 45.33 | 41.08 |
| $Al_2O_3$ | 3.31 | 3.87 | 3.29 | 2.13 | 3.30 | 1.38 |
| $Fe_2O_3$ | 8.55 | 8.98 | 9.05 | 8.72 | 8.87 | 9.02 |
| MgO | 34.61 | 34.54 | 34.02 | 39.23 | 37.51 | 39.70 |
| CaO | 4.18 | 4.65 | 5.10 | 3.17 | 2.81 | 4.31 |
| $Na_2O$ | 0.22 | 0.24 | 0.26 | 0.20 | 0.22 | 0.14 |
| $K_2O$ | 0.07 | 0.10 | 0.16 | 0.06 | 0.04 | 0.05 |
| $TiO_2$ | 0.09 | 0.08 | 0.08 | 0.11 | 0.07 | 0.08 |
| $P_2O_5$ | <L.D. | <L.D. | <L.D. | <L.D. | <L.D. | <L.D. |
| MnO | 0.12 | 0.13 | 0.12 | 0.12 | 0.13 | 0.13 |
| LOI | 2.99 | 2.44 | 3.37 | 1.11 | 1.08 | 3.06 |
| **Total (wt%)** | 99.37 | 99.65 | 99.28 | 99.14 | 99.35 | 98.95 |
| Mg# | 88.90 | 88.40 | 88.20 | 89.90 | 89.30 | 89.70 |
| **Trace (ppm)** | | | | | | |
| Cs | 0.07 | 0.08 | 0.08 | 0.05 | 0.05 | 0.06 |
| Rb | 6.48 | 7.94 | 12.11 | 4.78 | 3.49 | 4.12 |
| Ba | 8.90 | 10.90 | 8.78 | <L.D. | 7.13 | 7.67 |
| Sr | 84.62 | 70.41 | 76.40 | 52.00 | 13.95 | 182.35 |
| Pb | 0.51 | <L.D. | <L.D. | <L.D. | <L.D. | <L.D. |
| Th | 0.10 | 0.10 | 0.04 | 0.05 | 0.15 | 0.12 |
| U | 0.04 | 0.07 | 0.06 | 0.03 | 0.06 | 0.07 |
| Zr | 6.03 | 1.63 | 2.99 | 9.30 | 4.47 | 6.78 |
| Hf | 0.14 | 0.08 | 0.09 | 0.23 | 0.08 | 0.15 |
| Ta | 0.07 | 0.01 | 0.01 | 0.03 | 0.03 | 0.07 |
| Y | 2.41 | 2.63 | 2.40 | 2.40 | 2.37 | 1.68 |
| Nb | 1.92 | 0.40 | 0.44 | 0.56 | 0.73 | 1.29 |
| Sc | 15.26 | 17.47 | 15.47 | 13.04 | 15.69 | 9.42 |
| Cr | 2910.95 | 2980.16 | 3020.06 | 2500.54 | 2804.73 | 1459.50 |
| Ni | 1867.04 | 1725.95 | 1919.51 | 2115.29 | 1878.44 | 2372.31 |
| Co | 99.57 | 98.79 | 105.34 | 105.82 | 103.47 | 118.56 |
| V | 69.36 | 83.74 | 70.880 | 52.13 | 66.92 | 37.41 |
| W | 3.85 | 3.40 | 4.48 | 5.18 | 5.46 | 4.28 |
| Ga | 3.02 | 3.49 | 2.94 | 2.42 | 2.83 | 1.39 |
| Zn | 56.03 | 58.85 | 56.60 | 50.93 | 52.14 | 52.78 |
| Cu | 16.85 | 21.56 | 24.66 | 7.98 | 19.06 | 8.52 |
| As | <L.D. | <L.D. | 0.51 | <L.D. | 0.749 | 0.67 |
| Cd | 0.05 | 0.03 | 0.05 | 0.09 | 0.03 | 0.03 |
| Ge | 0.80 | 0.91 | 0.78 | 0.82 | 0.81 | 0.73 |
| Mo | 5.01 | 4.63 | 6.07 | 7.91 | 8.93 | 5.49 |
| Sb | 0.16 | 0.22 | 0.12 | 0.08 | 0.15 | 0.14 |
| Sn | 0.45 | <L.D. | 0.36 | <L.D. | 0.41 | 0.33 |

**Table 6.** (continued).

| Rock type | Lherzolite | | | | | |
|---|---|---|---|---|---|---|
| sample | BIW 88E | BIW 88-2 | BIW 88-1 | BIW 88-3 | BIW 88-5 | BIW 88-4 |
| Ta | 0.07 | 0.01 | 0.01 | 0.03 | 0.03 | 0.07 |
| La | 0.86 | 1.25 | 0.72 | 0.90 | 0.79 | 0.81 |
| Ce | 1.49 | 1.37 | 0.71 | 2.45 | 0.90 | 1.67 |
| Pr | 0.18 | 0.11 | 0.07 | 0.38 | 0.08 | 0.20 |
| Nd | 0.74 | 0.38 | 0.32 | 1.79 | 0.32 | 0.84 |
| Sm | 0.20 | 0.15 | 0.13 | 0.45 | 0.13 | 0.21 |
| Eu | 0.08 | 0.07 | 0.06 | 0.16 | 0.05 | 0.08 |
| Gd | 0.27 | 0.26 | 0.24 | 0.45 | 0.21 | 0.24 |
| Tb | 0.05 | 0.06 | 0.05 | 0.07 | 0.05 | 0.04 |
| Dy | 0.39 | 0.44 | 0.39 | 0.45 | 0.36 | 0.29 |
| Ho | 0.09 | 0.11 | 0.10 | 0.09 | 0.09 | 0.07 |
| Er | 0.27 | 0.31 | 0.28 | 0.25 | 0.28 | 0.17 |
| Tm | 0.04 | 0.05 | 0.05 | 0.04 | 0.05 | 0.03 |
| Yb | 0.30 | 0.34 | 0.31 | 0.24 | 0.32 | 0.19 |
| Lu | 0.05 | 0.05 | 0.05 | 0.04 | 0.05 | 0.03 |
| **Eu/Eu*** | 1.06 | 1.01 | 1.02 | 1.06 | 0.97 | 1.08 |

presence of well-preserved zoned olivine within the studied basaltic lavas is indicative both of a rapid ascent to the surface of their magma and of a short duration of the interaction between basaltic melt and hosted lherzolite.

#### 4.2.3 Orthopyroxene

Orthopyroxenes are essentially present in lherzolites, although some xenocrysts are found in some basanites and basalts. The main orthopyroxene end-member components are $En_{87.6\text{-}88.3}Fs_{9\text{-}10.5}$ for xenocrysts and $En_{86.8–89.5}Fs_{9–10}$ in lherzolites. There are chemically characterized by CaO (0.3–1.3 wt%), $Al_2O_3$ (2.5–5.1 wt%), and exhibit relatively low $TiO_2$ (0–0.2 wt%) and $Cr_2O_3$ (0.2–0.8 wt%) contents. Their Mg# = [100 Mg/(Mg + $Fe^{2+}$)] varies between 89.7 and 90.9, and enstatite contents range from 86.8 to 89.5 mol% (Table 3). The studied orthopyroxenes display higher enstatite contents and thus $X_{Mg}$ compared to those from Kapsiki mantle xenoliths (En: 77–85 mol%; XMg: 0.89–0.92; Tamen *et al.*, 2015).

#### 4.2.4 Clinopyroxene

Clinopyroxene mainly consists of Cr-diopside ($Wo_{46–47}En_{42.6–44}Fs_{4–4.2}Ac_{6–7}$) in lherzolite, sometimes associated with pigeonite ($Wo_{11}En_{79}Fs_8Ac_2$), diopside in basanites and basalts ($Wo_{47–50}En_{27–39}Fs_{11–22}Ac_{2–4}$), and accessory augite ($Wo_{39.8}En_{40.2}Fs_{18}Ac_2$) in latite. Their compositions are homogeneous at a sample scale but vary from lherzolites to the host lavas. Cr-diopside is characterized by high $X_{Mg}$ (~0.92) and displays significant $Cr_2O_3$ (0.7–0.8 wt%), low $TiO_2$ (0.3–0.4 wt%), and constant $Al_2O_3$ (5.5–6.1 wt%) contents compared to diopside found in basanites and basalts, which has very low $X_{Mg}$ (0.6–0.8), low $Cr_2O_3$ (0–0.4 wt%), and high $TiO_2$ (2.5–7.7 wt%) and $Al_2O_3$ (5.5–11.9 wt%) contents. The single analyzed pigeonite crystal ($X_{Mg}$ = 0.90) found included in a Cr-diopside is Mn-poor (MnO: 0.11 wt%), more aluminous ($Al_2O_3$: 4.96 wt%), and more magnesian (MgO: 28.4 wt%) relative to those analyzed in peralkaline trachyte from the neighboring Tchabal Mbabo massif (MnO: 3.3–3.6 wt%; Bardintzeff *et al.*, 2020) and to those described in trachyandesites from the French Massif Central (Maury and Brousse, 1978: MnO = 0.7–2 wt%).

Clinopyroxenes within mantle xenoliths of sample BIW805 are characterized by $SiO_2$ contents ranging between 52.8 and 53.1 wt%, $TiO_2$ (0.28–0.3 wt%), $Al_2O_3$ (5.5–6.2 wt%), CaO (21–21.7 wt%), $Na_2O$ (1.65–1.7 wt%), and Mg# (92.9–94.5), high $Al^{VI}$, and low $Al^{IV}/Al^{VI}$ ratios, similar to clinopyroxenes formed by basaltic melt-mantle peridotite reactions at mantle depths (Yuan and Yan, 2022). The spinel lherzolites from Bini Warack contain olivine with an average Mg# of 90, coexisting with Opx of Mg# 90 and Cpx with Mg# 93, which is typical of equilibrium lherzolite assemblages.

#### 4.2.5 Spinel

Spinels occurring in host lavas are mainly aluminous magnetites and rarely chromiferous spinels, while those in lherzolites are essentially chromiferous spinels. Basanites contain the most ferriferous, titaniferous spinels, while the hosted lherzolites have the most aluminous and magnesian spinels (Tab. 4). In comparison with the spinels of lavas

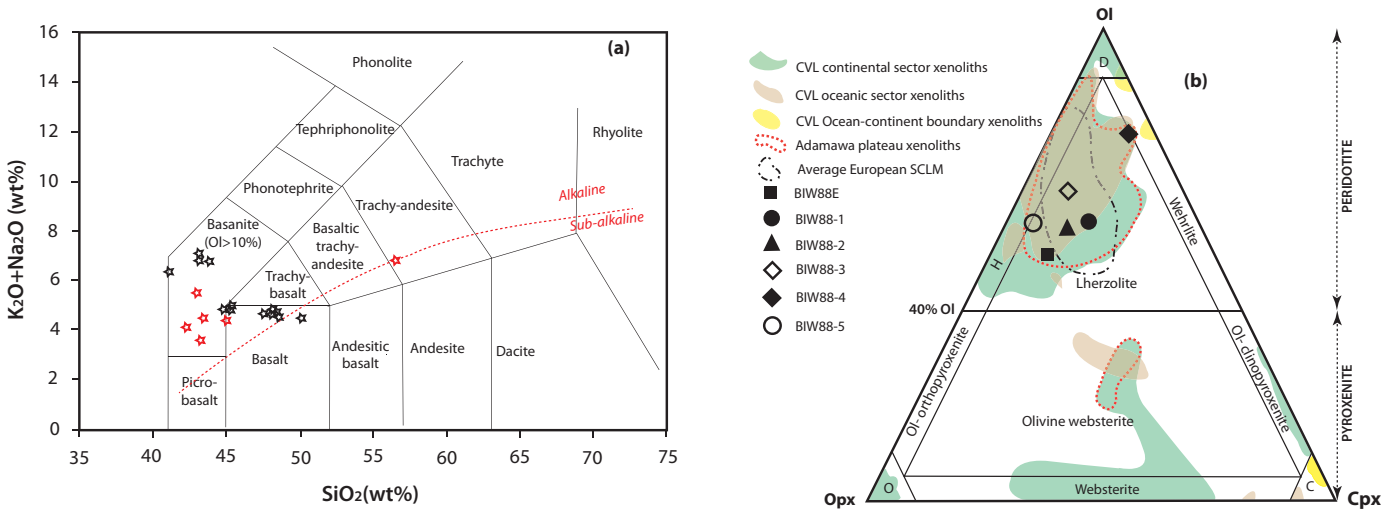


**Fig. 4.** Nomenclature of the studied rock samples. (a) Position of Bini Warack lavas in the $Na_2O+K_2O$ versus $SiO_2$ classification diagram of Le Bas *et al.* (1986)—the black stars correspond to data from Tiabou *et al.* (2019), while the red stars are analyses from the current work; (b) Position of the studied mantle xenoliths in the classification diagram for ultramafic rocks of Streckeisen (1976) compared to other mantle xenoliths studied along the CVL. Ol, olivine; Opx, orthopyroxene; Cpx, clinopyroxene; D, dunite; O, orthopyroxenite; C, clinopyroxenite; H, Harzburgite. Average European subcontinental lithospheric mantle (AESCLM) after Downes (1997); xenoliths from respective sectors of the CVL modified from Pintér *et al.* (2015) using recent data of Nkouandou *et al.* (2015), Wagsong Njombie *et al.* (2018), Tedonkenfack *et al.* (2021), and Puziewicz *et al.* (2023).

[Cr# (Cr/(Al + Cr): 0.01–0.37; XFe: 0.31–1; Mg# ≤45)], spinels from hosted lherzolites usually have higher Cr# (0.1–0.22), higher Mg# (31–71), and lower XFe (0.24–0.56) and mainly plot within the fertile peridotite field in the Cr# versus Mg# diagram (Fig. 3d). The spinels' Cr# values of the studied lherzolites are in the same range as those of mantle xenoliths from several localities from the CVL, such as Wum (0.02–0.29; Puziewicz *et al.*, 2023), Kapsiki (0.13–0.44; Tamen *et al.*, 2015), and Nyoss (0.1–0.39; Temdjim *et al.*, 2004; Teitchou *et al.*, 2011). The wide ranges of $Fe^{2+}/Fe^{3+}$ratios (0.67–6.63) and $TiO_2$ contents (0–46.88 wt%) testify to the presence of both mantle spinels ($TiO_2$ <0.2 wt%; $Fe^{2+}/Fe^{3+}$ > 2) and magmatic spinels in host lavas, according to Kamenetsky *et al.* (2001). Most analyzed spinels from lavas display extremely high $TiO_2$ contents (~20–47 wt%), far above those of xenocrysts or spinels found in other lavas from other localities along the CVL (Nono *et al.*, 1994; Tamen *et al.*, 2007).

## 4.3 Whole-rock geochemistry

Major and trace element compositions of 21 representative samples of the host lavas (6 from this study and 15 from Tiabou *et al.*, 2019) and 6 mantle xenoliths are presented in Tables 5 and 6, respectively. Because of loss on ignition values higher than 2 wt% in most of the analyzed samples, the results were recomputed on an anhydrous base.

### 4.3.1 Host lavas

#### *4.3.1.1 Major elements*

Although a few samples display $Na_2O$-$K_2O$>2 majority of the studied samples are sodic; therefore, we have chosen the TAS classification diagram instead of the potassic series one. The analyzed host lavas plot in the field of basanite, basalt, and basaltic trachyandesite on the classification diagram of LeBas *et al.*, 1986 (Fig. 4a). Since the sample BJM59A plotting in the field of basaltic trachyandesite has ($Na_2O$-2) < $K_2O$, it will be considered rather as a latite. $SiO_2$ ranges from 42.35 to 56.56 wt%, the total alkali ($Na_2O+K_2O$) varies from 2.34 to 7.07 wt%, and $Na_2O/K_2O$ ratios from 0.94 to 1.92 with moderate MgO contents (3.56–13.86 wt%) and Mg# (43.07–70.56). Their differentiation index (DI) ranges from 21.3 (basanite HOL32) to 53.6 (latite), with Mg numbers varying between 43 and 71.

All the analyzed samples are apatite (1.12–3.52 wt%) and ilmenite (3.12–7.31 wt%) normative, and the silica-undersaturated lavas (basanites and basalts) are nepheline (4.31–18.21 wt%) normative. The only lava without normative nepheline or olivine but containing normative quartz (4.82 wt%) and hypersthene (16.14 wt%) is the sample BJM59A, classified as a latite. Mafic lavas are alkaline sodic ($Na_2O/K_2O$: 1.14–1.92), while latite is potassic with $Na_2O/K_2O$ = 0.94.

In the Harker diagrams (Fig. 5), $Al_2O_3$ shows a positive correlation with $SiO_2$, while $Fe_2O_{3T}$, CaO, $P_2O_5$, and $TiO_2$ are negatively correlated with $SiO_2$. The positive correlation of $Al_2O_3$ with $SiO_2$ is indicative of non-fractionation of plagioclase, while the negative trends in $Fe_2O_{3T}$, CaO, $TiO_2$, and $P_2O_5$ versus $SiO_2$ reveal the fractionation of olivine, pyroxenes, Fe–Ti oxides, and apatite, respectively.

#### *4.3.1.2 Trace elements*

The amounts of some trace elements vary significantly from mafic to felsic lavas. Ni (41.05–476.5 ppm, with the highest value in the basanite MBA11); Cr (6–645 ppm, with the highest value in MBA11); Cu (≤60 ppm, with the maximum in basalts WA3 and WA6); Co (25–55 ppm, with the highest amount in MBA11); Nb (22.4–151, with the

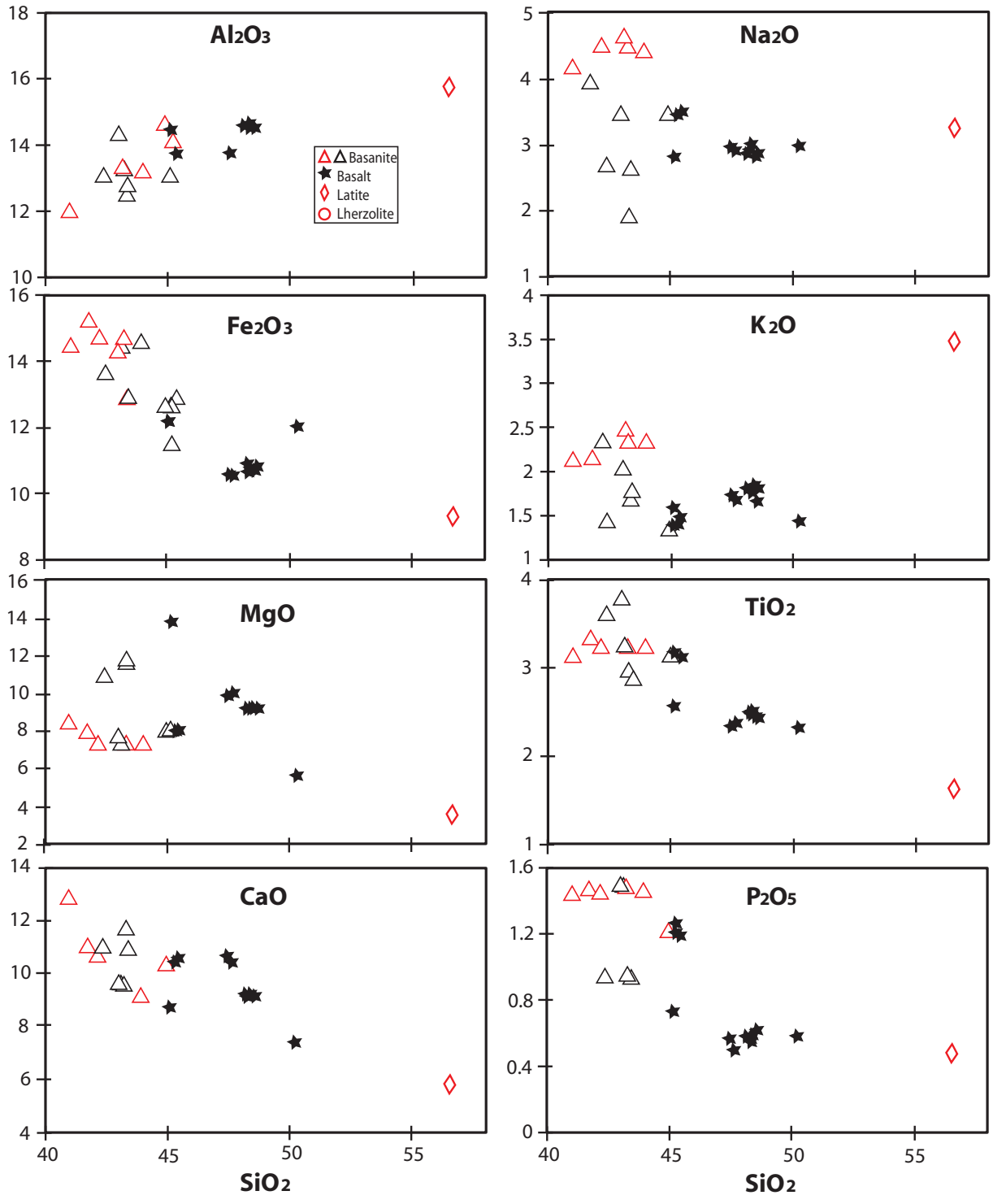


**Fig. 5.** Harker diagrams of host lavas. The legend is the same as in 3 The same rock types from Tiabou *et al*. (2019) are represented in black color.

highest value in basanite BA19); Zn (8–174 ppm, with the highest value in basanite SAF88); Y (20–47 ppm, with the highest value in BJM59A); Ga (15–28 ppm, with the highest value in BA50); and Pb (3–39 ppm, with the highest value in basalt BA16). The amounts of incompatible trace elements range from 397 to 1401 ppm for Sr, 492 to 1111 ppm for Ba, 232 to 530 ppm for Zr, 5 to 11 ppm for Hf, and 2 to 8.5 ppm for Ta. The ranges of some compatible trace element contents, such as Co, Ni, Cr, V, Sc, Cu, and Zn, are consistent with fractional crystallization. The Co and Ni contents are lower than those for primitive magmas (Co: 50–70 ppm; Ni: 300–400 ppm; Tatsumi *et al.*, 1983; Jung and Masberg, 1998)

and are therefore strongly in support of prior fractionation of olivine. The distribution of selected trace elements relative to $SiO_2$ contents displays no significant correlation.

The chondrite-normalized multi-element diagrams (see Fig. 6a–6c) are comparable with those of oceanic island basalts (OIB) and show enrichment in Ba, Th, U, Nb, and La. The basanites and basalts spectra exhibit all negative anomalies in K, Ti, and Y while latite displays negative anomalies in K, Nb, and Ti. The chondrite-normalized rare earth elements (REE) patterns of lavas are quite homogeneous (see Fig. 6b–6d). They show a strong enrichment in LREEs compared with HREEs, reflected by a moderate to high $(La/Yb)_N$ ratio (9.3–30). The mafic lavas show an overall weak positive Eu anomaly, contrary to latite displaying a negative one. The values of Eu anomalies $[Eu/Eu^*=Eu_N/(Sm_N\ Gd_N)^{1/2}]$ as defined by Taylor and McLennan (1985) range from 1.08 to 0.82 in mafic lavas to 0.70 in latite.

#### 4.3.2 Lherzolites

##### *4.3.2.1 Whole-rock compositions*

According to their modal compositions determined using the MINSQ program (Herrmann and Berry, 2002), the analyzed Bini Warack mantle xenoliths are all lherzolites (see Fig. 4b). They are enriched in $Al_2O_3$ (1.38–3.87 wt%), CaO (2.81–5.1 wt%), $TiO_2$ (0.07–0.11 wt%), and $Na_2O$ (0.14–0.26 wt%) relative to harzburgite from the southern Dibi area ($Al_2O_3$: 0.8–1.3 wt%, CaO: 0.32–1.4 wt%, $TiO_2$: 0.06–0.21 wt %, and $Na_2O$: 0.08–0.26 wt%; *cf.* Adama *et al.*, 2021). Their bulk-rock Mg# ranges from 88.2 to 89.9 and is comparable with that of their olivine (Mg#: 84.4–91) and Opx (Mg#: 89.7–90.92). They are similar in terms of bulk-rock composition to the estimated primitive mantle (see McDonough and Rudnick, 1998) and the neighboring Youkou volcano lherzolites (Wagson Njombié *et al.*, 2018). Given their position in the whole-rock compositional variation in $Al_2O_3$ versus CaO diagram (Fig. 7), the studied peridotites evidenced low partial-melting degrees (<15%).

Their primitive mantle-normalized REE patterns enable distinguishing two types of lherzolites: (1) those displaying spoon-shaped REE patterns (*e.g.*, BIW88-1, BIW88-2, and BIW88-5) with inflection at Nd or Sm, depending on the sample, marked by enrichment in LREEs and HREEs (0.7–5.6 times C1) relative to MREEs: $[La/Sm]_N$ = 2.51–5.24, $[Sm/Yb]_N$ = 0.44–1.25, and $[La/Yb]_N$ = 1.70–3.15; and (2) the lherzolite BIW88-3 displaying a more or less "S-shaped" REE pattern (Fig. 6h) characterized by LREE enrichment over MREEs and HREEs. Their chondrite-normalized multi-element spider diagrams are marked by somewhat slightly higher contents in LILE relative to HFSE, with positive anomalies in Rb, K, and Sr (Fig. 6g).

### 4.4 Nd and Sr isotopic signatures

Four new Rb/Sr and Sm/Nd isotopic ratios were obtained in mafic host lavas. They are characterized by $^{87}Sr/^{86}Sr$ isotopic ratios ranging between 0.702994 (basanite SAF88) and 0.703213 (basanite SOT22) and $^{143}Nd/^{144}Nd$ from 0.512862 (basanite MBA11) to 0.512927 (basanite SAF88), with low $^{87}Rb/^{86}Sr$ ratios (<0.15) and low $^{147}Sm/^{144}Nd$ ratios (0.10–0.11). The measured isotopic data have been corrected to 11.39 Ma, representing the oldest dated lava in the area (Marzoli *et al.*, 1999), in order to compare them to the available data from Miocene lavas along the CVL. The analyzed samples are characterized by initial $^{87}Sr/^{86}Sr_{(11.39\ Ma)}$ between 0.702987 and 0.703206 and initial $^{143}Nd/^{144}Nd_{(11.39\ Ma)}$ between 0.512854 and 0.512918. The selected analyzed samples display positive $\varepsilon Nd_{(11.39\ Ma)}$ ranging from +4.84 to +6.09 (Fig. 8).

## 5 Discussion

### 5.1 Characteristics of the SCLM beneath Bini Warack area

At first glance, the low Sr isotopic ratios (0.70299–0.70312) coupled with the positive initial εNd of the Bini Warack host lavas refer to their mantle origin. However, due to the fact that we did not carry out isotopic measurements on all the samples, we will invoke other criteria to constrain their mantle source characteristics.

#### 5.1.1 Magmas sources and nature of the SCLM beneath the Adamawa Plateau

The bulk rock geochemical data of the Bini Warack host lavas all plot above the ΔNb line in the Nb/Y and Zr/Y ratio diagram (Fig. 9a), thus pointing out their compatibility with mantle plume activity. The OIB affinity of the Bini Warack host lavas, illustrated above by the similarities of the rare earth and multi-element spectra, as well as the strong involvement of the HIMU-like signature in their genesis, is also highlighted in the $(^{87}Sr/^{86}Sr)_{initial}$ versus $(^{143}Nd/^{144}Nd)_{initial}$ diagram (see Fig. 8).

Considering that Mn has high affinity for garnet and that Al content is very sensitive to temperature, De Hoog *et al.* (2010) used these major elements in olivine to define mantle lithologies and therefore to distinguish between garnet peridotite, spinel peridotite, and garnet-spinel peridotite. The olivine in the studied xenoliths and xenocrysts displays low Al contents (average $Al_2O_3$ = 0.03 wt%) and high Mn contents (average MnO = 0.14 wt%) similar to those of spinel–lherzolite, showing that the lithology of the mantle lithosphere beneath Bini Warack is likely spinel lherzolite, which is consistent with geochemical findings (Fig. 9b).

#### 5.1.2 Thickness, volume and thermal evolution of the SCLM reservoir beneath Bini Warack

Olivine is one of the major rock-forming minerals in peridotite, and its Fo values are generally considered as a proxy for the extent of partial melting (Pearson, 1999). Forsterite values in the studied mantle xenoliths range from 84% to 91%. This Fo range is typical of olivine of the mantle xenoliths of the Ngaoundéré area (89%–91%: Nkouandou *et al.*, 2015; Nkouandou and Temdjim, 2011; Wagsong Njombié *et al.*, 2018) and similar to that of off-craton mantle rocks (88%–92%: Boyd and Mertzman, 1987; Boyd *et al.*, 1997) and oceanic mantle residues (90.5%–91.5%: Boyd, 1989), indicating that the SCLM beneath the Bini Warack region is likely juvenile and comparable to the oceanic lithospheric mantle.

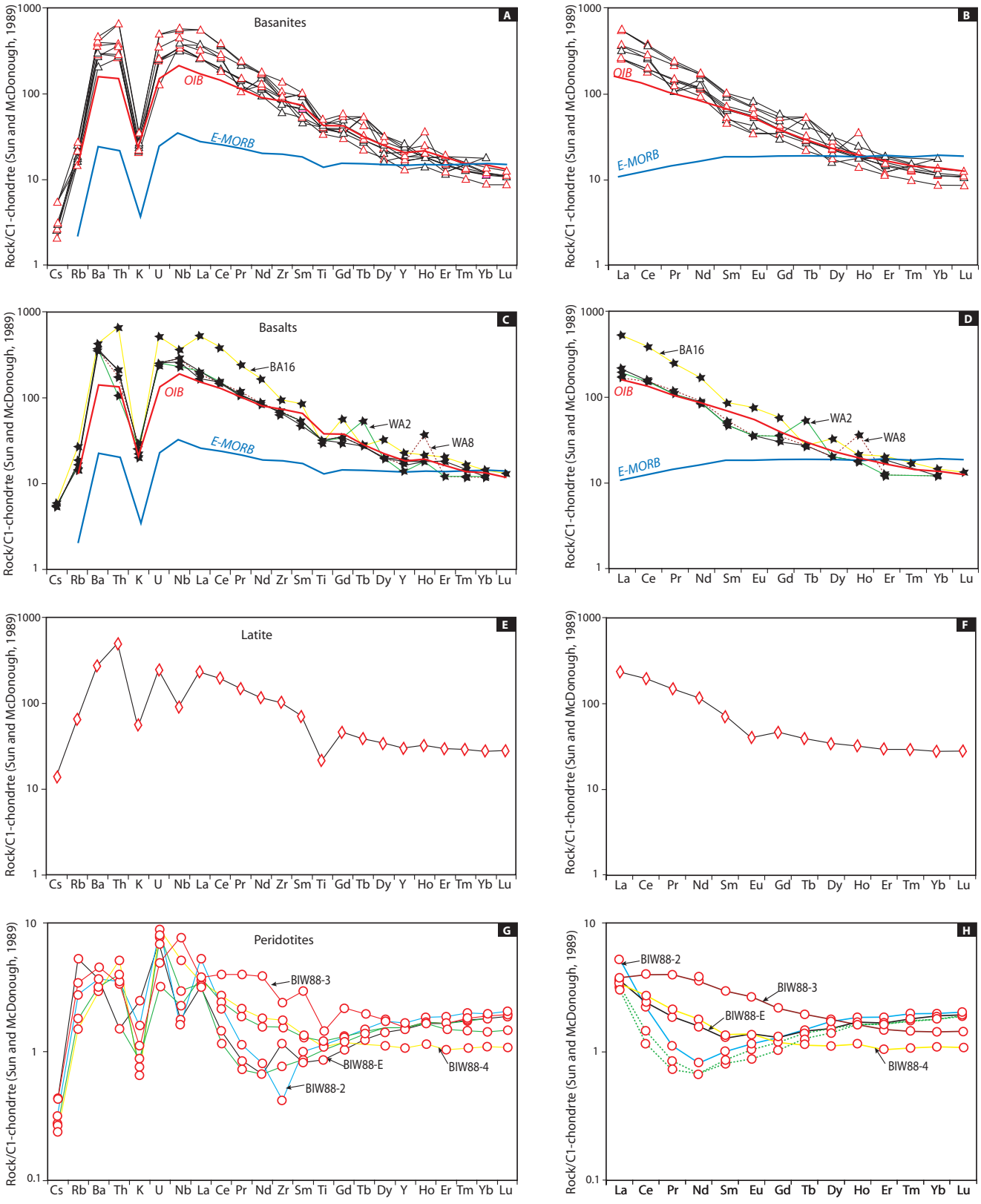


**Fig. 6.** Chondrite-normalized multi-element and rare earth element diagrams of Bini Warack lavas and hosted mantle xenoliths. In red color are samples from this study, while samples from Tiabou *et al*. (2019) are in black; OIB and E-MORB data are from Sun and McDonough (1989).

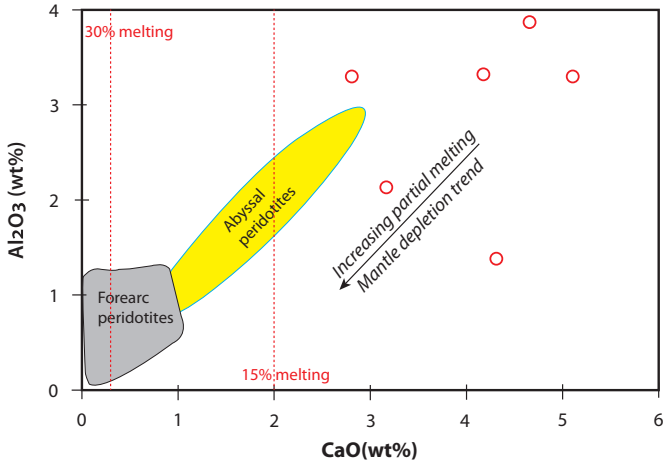


**Fig. 7.** Whole-rock compositional variation in the $Al_2O_3$ versus CaO diagram. Fore-arc and abyssal peridotite fields are after Ishii *et al.* (1992) and Pearce *et al.* (1992) respectively.

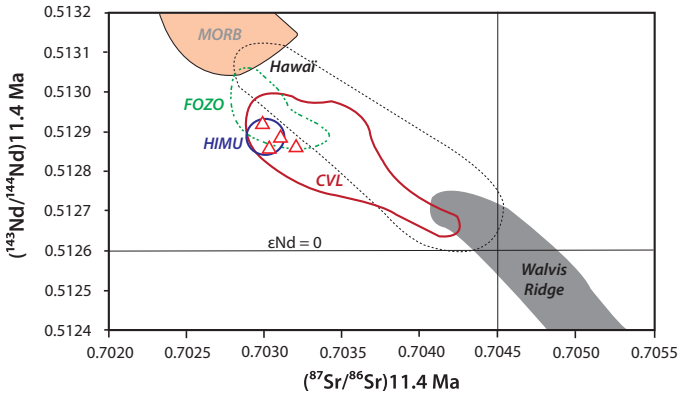


**Fig. 8.** lot of the Bini Warack lavas' isotopic data in the $(^{87}Sr/^{86}Sr)_{initial}$ versus $(^{143}Nd/^{144}Nd)_{initial}$ diagram. The MORB, HIMU, and FOZO mantle poles are from Zindler and Hart (1986); the Walvis and Hawaii fields are from Aït Hamou *et al.* (2000); and the CVL lava fields are from Halliday *et al.* (1990) and Marzoli *et al.* (2000).

Generally, the iron content of the residue, unlike the magnesium content, is sensitive to melting pressure (Herzberg, 2004). Therefore, Mg# in whole rocks, in combination with $Al_2O_3$, can help to infer the melting depth (Herzberg and Rudnick, 2012). The FeOt, $Al_2O_3$, and MgO contents of the Bini Warack peridotites suggest that their melting began at depths $\leq$2 GPa, similar to those of the harzburgite xenoliths from the nearby Guinadji, Djalsoka, and Mokolo–Kapsiki localities (Fig. 10a and 10b). Due to their sensitivity to pressure variations, elements such as the REE, Ti, Na, and Hf are proxies to constrain melting depths (Putirka, 1999). The remarkable negative K peak, contrary to Ba in the multielement profiles (see Fig. 6), indicates the presence of hydrous mineral phases such as phlogopite and amphibole in the mantle source.

On the other hand, melts in equilibrium with amphibole-bearing sources would have rather low Rb/Sr (<0.1) and higher Ba/Rb (>20), while melts being produced with phlogopite in the source would inherit low Ba/Rb values (Furman and Graham, 1999; Ma *et al.*, 2014). Therefore, the low Rb/Sr (0.03–0.37) and high Ba/Rb (4.4–26) ratios of the host lavas from Bini Warack are reliable with the presence of amphibole in the source region. These two hydrous minerals are known to be stable at depths less than 150 km. Furthermore, the presence of sharp contacts of mantle xenoliths with the host lavas may indicate that the magma hosting these mantle materials was likely produced at about 80 to 150 km within the garnet peridotite mantle stability field, as it was evidenced for mantle xenoliths from the Oku volcanic group by Asaah *et al.* (2015a). Those depth values estimated from geochemical data and mineralogical evidence are consistent with geophysical estimates. Indeed, the deepest density discontinuity so far determined beneath the Adamawa region using spectral analysis of gravity data ranges between 75 and 149 km and corresponds to an anomalous low-velocity upper mantle structure (Nnangue *et al.*, 2000). On the other hand, the Moho discontinuity depth ranges from 19 to 36 km (Fairhead and Okereke, 1988; Poudjom Djomani, 1995; Nnange *et al.*, 2000; Tokam *et al.*, 2010), depending on the methods used. These depths overall evidence a crustal thinning related to a mantle upwelling process similar to that described for the northern Kapsiki plateau (Tamen *et al.*, 2015).

The Bini Warack mantle xenoliths are characterized by protogranular to porphyroclastic textures. The work of Zangana *et al.* (1997) demonstrated that undeformed mantle xenoliths, *i.e.*, those showing protogranular to porphyroclastic textures such as those from Bini Warack, have high equilibrium temperatures (>900°C) contrary to deformed xenoliths, which have lower equilibrium temperatures (<900°C).

The pyroxene equilibrium temperatures estimated using the geothermometers of Brey and Kohler (1990) and Liang *et al.* (2013), and also taking into account the Cr# ratios of the spinel in lherzolites, vary from 900 to 1100°C. This equilibrium temperature gradient is identical to that of the mantle xenoliths of the OVG lavas (Puziewicz *et al.*, 2023) located approximately 300 km SW of our study area along the CVL.

### 5.2 Melting conditions for magmas generation

It is noteworthy that partial melts derived from refractory harzburgites are characterized by low $TiO_2$ contents (<1 wt%; Falloon and Danyushevsky, 2000), while melts derived from mafic lithologies (various types of pyroxenites, hornblendite, etc.) typically have high $TiO_2$ contents (>2 wt%; *e.g.*, Kushiro, 1996). The basaltic rocks from the Bini Warack area that have high $TiO_2$ contents could rightly be considered, referring to Dai *et al.* (2023), as issued from the partial melting of silica-deficient pyroxenites embedded in a fertile lherzolitic mantle. Their $TiO_2$ contents are higher than those of harzburgite-derived melts but similar to those of non-peridotite mantle lithologies and those of low-extent melts derived from a low degree (< 10%) of melting of fertile lherzolites (Fig. 9c). Besides their high $TiO_2$ contents, they display high Ti/V ratios, suggestive of low oxygen fugacity (Fig. 9d).

The presence of garnet in the mantle source is sustained by the overall enrichment in LREE and MREE relative to HREE (see Fig. 6h). The Zr/Nb versus La/Yb diagram (Fig. 10a) allows estimating both the amount of garnet in the source and the degree of melting. Thus, it appears that the basalts from the Bini Warack definitely fit in the area of alkali basalts of the

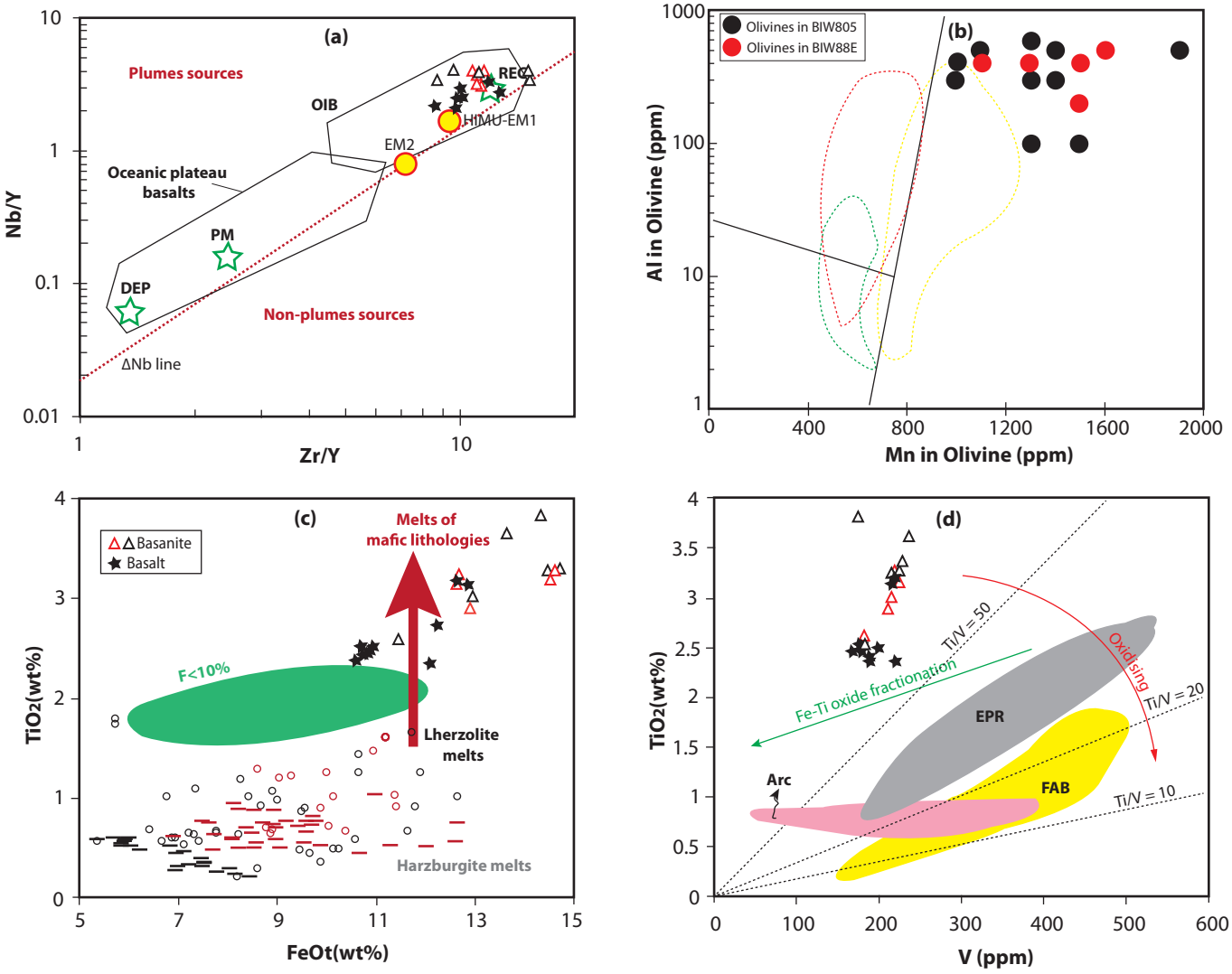


**Fig. 9.** (a) Plot of the host lavas relative to various mantle compositional components (green star) and fields for basalts from different tectonic settings as defined by Weaver (1991) and Condie (2005); (b) Plot of Al versus Mn for the olivine xenocrysts; (c) Comparison of Bini Warack basanites and basalts with experimental melts of representative mantle lithologies using their $TiO_2$ and $FeO_t$ contents; (d) $TiO_2$ versus V plot of Bini basanites and basalts. In panel (a), DEP, deep depleted mantle; EM1, enriched mantle sources; HIMU, high U/Pb mantle source; OIB, oceanic island basalt; PM, primitive mantle; REC, recycled component. In panel (b), the fields of spinel–garnet lherzolite (dashed green line), garnet–lherzolite (dashed red line), and spinel–lherzolite (yellow line) are after Yuan and Yan (2022). The green ellipse in panel (c) denotes the low-degree (<10%) experimental melts of fertile lherzolite. The black circles illustrate partial melts of fertile lherzolite, while the red ones highlight experimental melts formed at 1.5–2.5 GPa, just as the black dashes represent the composition of harzburgite partial melts and the red ones that of their experimental melt at 1.5–2.5 GPa. The thick red arrow schematically shows non-peridotite mantle rocks (*e.g.*, amphibolite, silica-deficient, and silica-excess pyroxenites) typically with high $TiO_2$ contents (≥2 wt%; Kushiro, 1996). Data for experimental melts of lherzolite and harzburgite are consistent with the compilation of Dai *et al.* (2023). In panel (d), the compositional zones for volcanic rocks from various tectonic settings and the magmatic differentiation trend caused by Fe–Ti oxide fractionation are from Reagan *et al.* (2010). FAB, fore-arc basalts; EPR, East Pacific Rise.

CVL and are derived from <2% partial melting of a lherzolitic mantle source, containing 2 to 6% garnet, such as alkaline basalts from the OVG studied by Asaah *et al.* (2015a). In the Yb/Sm versus Tb/Yb diagram (Fig. 10b), the studied mafic lavas from the Bini Warack area lie on the mixing paths of low-extent (<10%) melts from spinel- and garnet-facies mantle sources. Like the basaltic rocks of the northwest China craton (Dai *et al.*, 2024), the basaltic lavas from the Bini Warack area tend to cluster at low Tb/Yb ratios. This is thought to be related to the negligible amount of garnet peridotite-derived melt fractions relative to that of the spinel peridotite-derived melt fraction in the studied basaltic rocks.

Given that heavy REEs are sensitive to the presence of garnet during melting, their bulk-rock abundance combined with residue/melt partitioning modeling is likely to constrain the melting pressure (Canil, 2004; Simon *et al.*, 2008). Figure 10c and 10d display the range of whole-rock REE models of the Bini Warack lherzolite samples together with modeling results for the

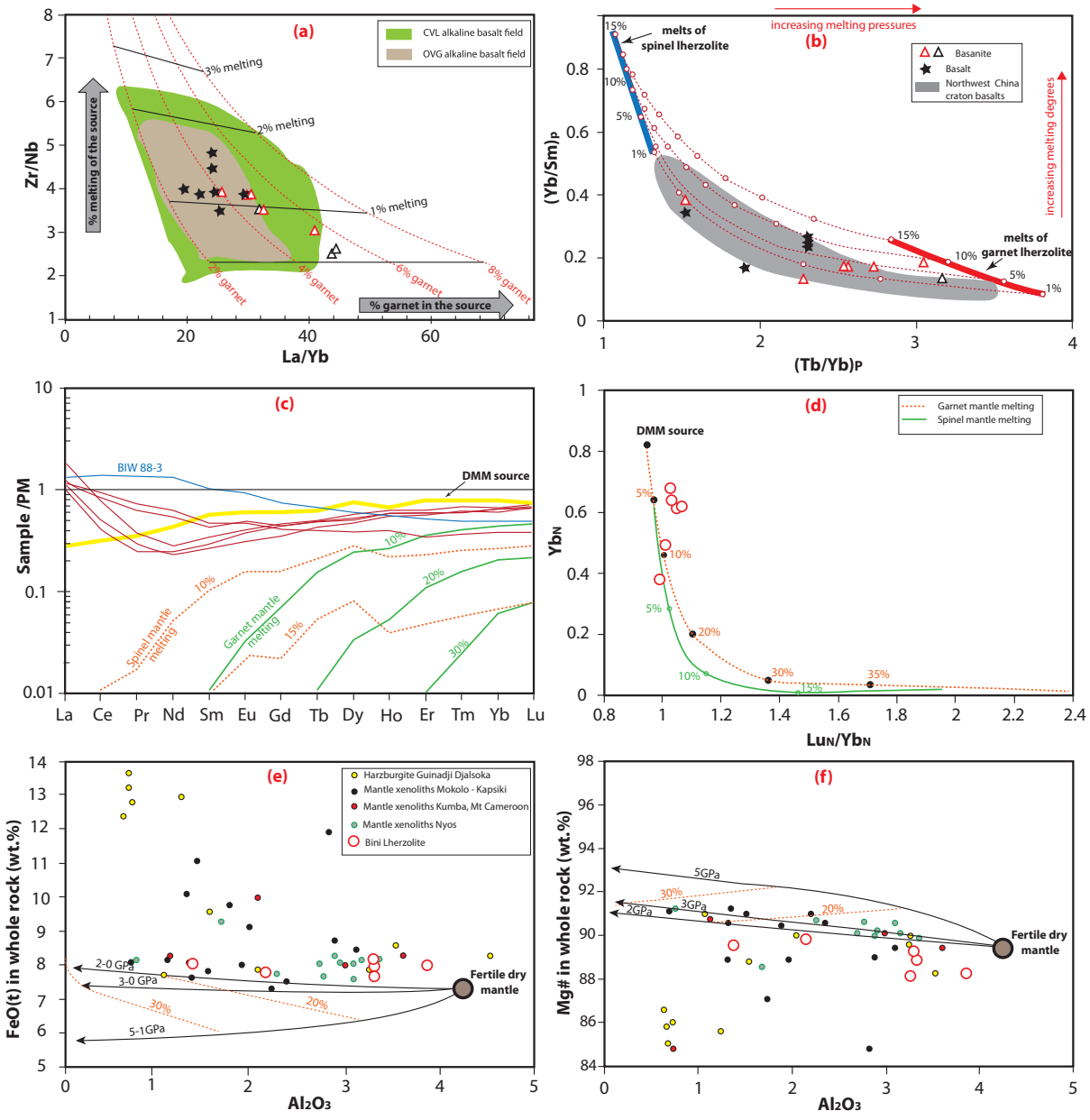


**Fig. 10.** Covariation diagrams of major, trace, and rare earth elements. (a) Modeled melting (Zr/Nb versus La/Yb) results for the studied mafic lavas together with other mafic lavas with MgO>4 from the OVG and CVL. Melts that produced most basanites and alkali basalts were produced by <2% partial melting of a dominantly garnet (<6%) bearing mantle lherzolite. (b) Estimate of the melting degrees of the Bini mafic lavas, given a fertile lherzolite source with primitive mantle-like trace-element contents (McDonough and Sun, 1995). The dashed red lines designate the mixing paths of aggregated fractional partial melts from garnet- and spinel-facies lherzolites at the fixed melting degrees (1%, 5%, 10%, 15%). Partition coefficients are taken from Bédard (2006) for olivine, orthopyroxene, clinopyroxene, and spinel and from Adam and Green (2006) for garnet. In black color are samples from Tiabou *et al.* (2019). (c) Primitive mantle (McDonough and Sun, 1995) normalized REE for the Bini lherzolites. The trace element modeling results for mantle melting in spinel and garnet stability fields of a fertile mantle source and that of the depleted MORB mantle source (DMM) (Workman and Hart, 2005) (modeling of Doucet *et al.*, 2023) are also shown. (d) $Lu_N/Yb_N$ versus $Yb_N$ for Bini lherzolites compared to melting models in the spinel stability field (green line) and garnet stability field (red dashed line). The primitive mantle values are from McDonough and Sun, 1995. Trace element modeling for a DMM source in spinel and garnet stability fields with garnet exhaustion after 20% of melting. (e) and (f) Whole rock $Al_2O_3$ versus Mg# and $FeO_t$ of the studied lherzolite together with other mantle xenoliths from northern Cameroon. The composition of Northwest China craton basalts is from Dai *et al.* (2024), and that of mantle xenoliths is from Nyos (Bilong *et al.*, 2010; Teitchou *et al.*, 2011); Kumba after Sababa *et al.* (2015); Mt. Cameroon after Wandji *et al.* (2009); Mokolo (ongoing work); Kapsiki after Tamen *et al.* (2015); and Guinnadji and Djalsoka after Adama *et al.* (2021). Thick black lines show the compositions for melting residue formed by isobaric batch melting of fertile mantle sources at 2, 3, and 5 GPa (Herzberg, 2004). Dashed red lines show polybaric melt extraction at 20% and 30% of melting.

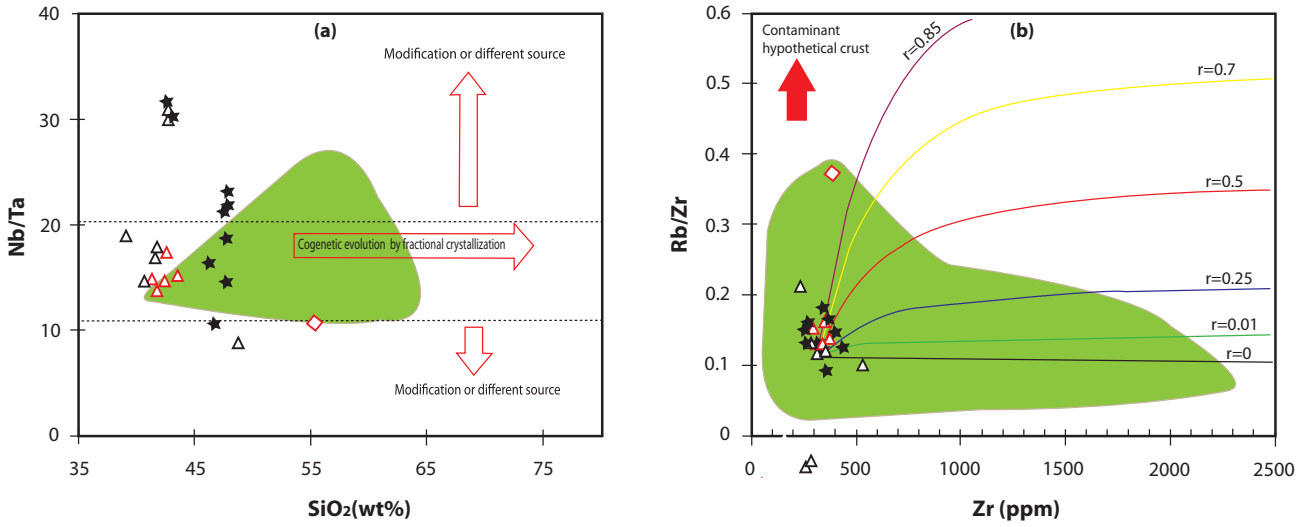


**Fig. 11.** Plot of Bini Warack lavas in (a) the Nb/Ta versus $SiO_2$ diagram illustrating the narrow variation of Nb/Ta ratios for most samples; (b) AFC Rb/Zr versus Zr modeled diagram. The green field represents CVL lavas (Asaah *et al.*, 2015b). The legend is the same as in the previous figure.

composition of melt residues that start melting within the spinel and garnet stability field from a fertile mantle source with a depleted MORB mantle composition (Workman and Hart, 2005). In the melting model within the spinel stability field, the degree of melt extraction for the Bini Warack mantle xenoliths would be somewhat ≥10%, similar to the melting estimates of major elements (see Fig. 10e–10f). On the other hand, their HREE contents (*e.g.*, Yb) are consistent with a low degree (≤4%) of polybaric melting that starts in the garnet stability field and ends in the spinel stability field (Fig. 10e), simulating the ascent of mantle plumes (Simon *et al.*, 2008; Doucet *et al.*, 2012).

### 5.3 Assimilation and fractional crystallization

In general, magmas rising from the mantle are possibly contaminated by the assimilation of crustal material, depending on the time taken to reach the surface. The presence of mantle xenoliths in most of our studied lavas is indicative of a rapid ascent of their parental magmas, which does not favor extensive fractional crystallization and substantial contamination in crustal magma chambers. Nb/Ta ratios for the majority of Bini Warack lavas vary between 10 and 19 with an average of 15 and do not vary meaningfully with $SiO_2$ (Fig. 11a), pointing out their genetic relationship and their evolution by fractional crystallization. These values are similar for the entire CVL (average Nb/Ta = 16: Asaah *et al.*, 2015b). The relatively low Sr isotopic compositions of the analyzed basanites (<0.704) preclude any consistent crustal contamination. Moreover, the plot of the Bini Warack lavas in the assimilation and fractional crystallization (AFC) modeling diagram of DePaolo (1981) (Fig. 11b) reveals that almost all plots are around the initial magma composition and out of AFC curves. This indicates a small amount of fractional crystallization and insignificant assimilation, except for the latite sample, which is the most evolved lava, displaying a high Rb/Zr ratio.

The major and trace element compositions of the Bini Warack mafic lavas (Table 5), such as Ni (89–477 ppm), Cr (104–646 ppm), Co (25–55 ppm), and MgO contents (Mg# ≤71), are not so different from those of primary magmas in equilibrium with mantle olivine as defined by Jung and Masberg (1998) and Frey *et al.* (1978) (Ni: 300–500 ppm; Cr: 300–500 ppm; Co: 50–70 ppm, and Mg#: 68–72), inferring the slight incidence of fractional crystallization. Basanite samples have Mg# ≥61 and high Ni (209–476.5 ppm) and Cr (340–645.6 ppm) contents, nearly matching those of primary magmas. The decrease of CaO with increasing $SiO_2$ contents in the Bini Warack lavas provides evidence for the fractional crystallization of both olivine and clinopyroxene. Conversely, the constant positive correlation of $Al_2O_3$ with $SiO_2$ observed in the studied lavas points out that the crystallization of plagioclase was very restricted during their differentiation.

### 5.4 Mantle metasomatism

The presence of clinopyroxene associated with secondary olivine and spinels confirms that this metasomatism took place in asthenospheric upwelling settings (*e.g.*, Grégoire *et al.*, 2000a,b; Moine *et al.*, 2001; Delpech *et al.*, 2004).

Trace elements such as LILE and HFSE are frequently used to constrain the metasomatic nature and conditions (*e.g.*, Xu *et al.*, 2022) in basaltic rocks. Modal metasomatism is generally evidenced in mantle xenoliths by the presence of mineral phases such as amphibole and phlogopite, while the effects of cryptic metasomatism are particularly noticeable by whole-rock spectra and Cpx, enriched in LREE (Cvetković *et al.*, 2022). The likely presence of amphibole and phlogopite as demonstrated in the preceding section is suggestive of the involvement of a metasomatized SCLM.

According to Pearce (2008), the inference regarding hydrous metasomatism can be further evidenced by the Nb/Yb versus Th/Yb diagrams. In this diagram, the mafic lavas from Bini Warack overlap the mantle array defined by oceanic basalts, except for a few samples with markedly elevated Th/Yb at given Nb/Yb (Fig. 12a). This agrees well with the fact that metasomatic agents are generally controlled by $H_2O$-bearing melts/fluids, which have a low capacity to mobilize elements such as Th, Nb, and Yb (Johnson and Plank, 1999). As shown in Figure 12a, the basaltic lavas from

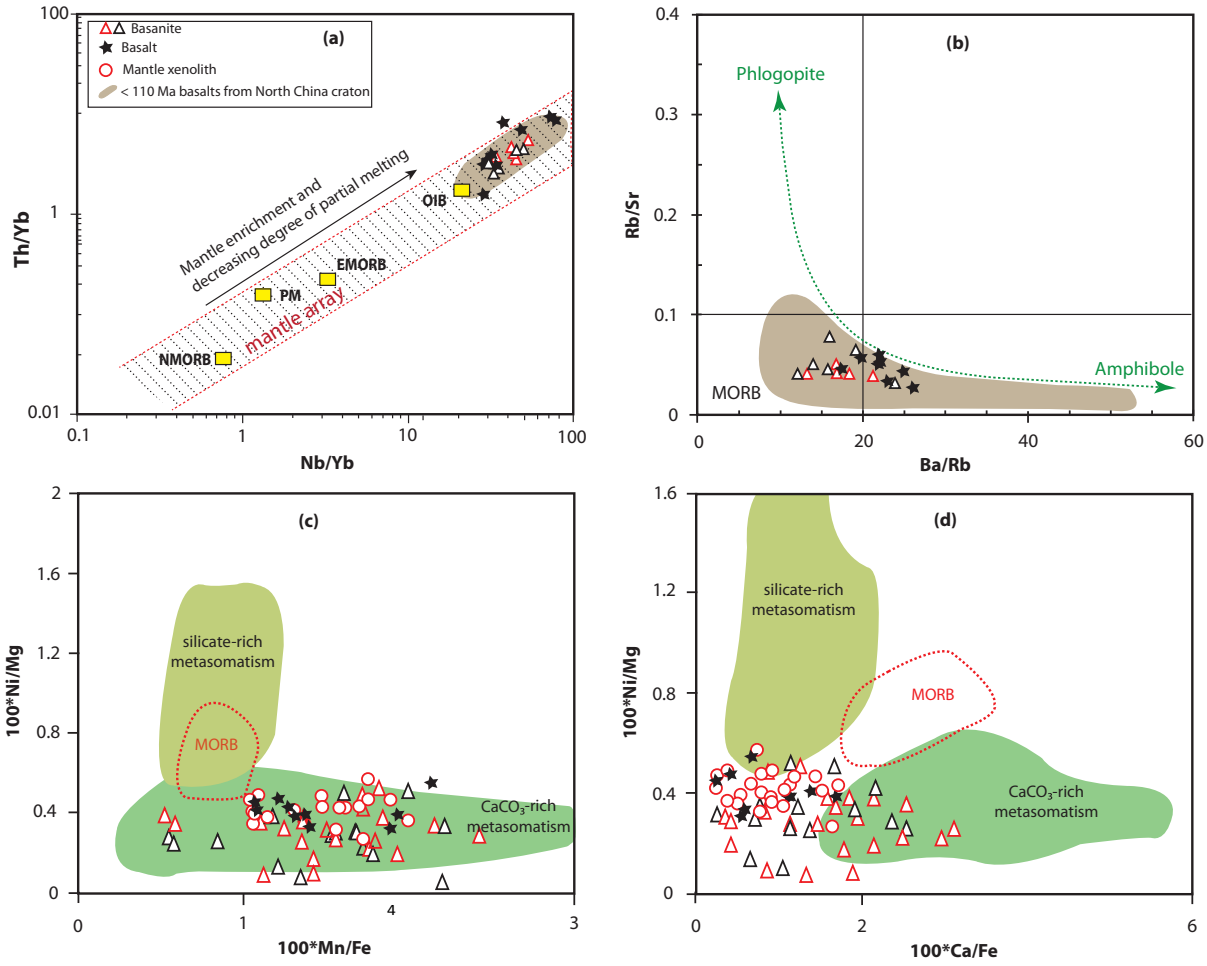


**Fig. 12.** Plots of bulk rock (a) Th/Yb versus Nb/Yb, (b) Rb/Sr versus Ba/Rb, (c) olivines 100*Mn/Fe versus 100*Ni/Mg, and (d) 100*Ca/Fe versus 100*Ni/Mg. The mantle array in panel (a) is defined by oceanic basaltic rocks, and the vertical black arrows indicate the effect of crustal melt input in the source of basaltic rocks (Pearce, 2008). In panel (b), the arrows showing partial melts from amphibole- and phlogopite-bearing mantle sources are adopted from Furman and Graham (1999). The compositions of MORB are taken from Gale *et al.* (2013). The olivine data for MORB are from Sobolev *et al.* (2007).

the Bini Warack area display greater Th/Yb relative to the mantle array (but are somewhat similar to those of recent basalts from the North China Craton), archetypal of lavas originating from the lithospheric mantle metasomatized by partial melts derived from subducted continental crust (Zhang *et al.*, 2002).

According to Furman and Graham (1999), partial melts derived from amphibole- and phlogopite-bearing mantle sources are characterized by high Rb/Sr and Ba/Sr ratios, respectively. Mafic lavas (basanite + basalt) from Bini Warack overall exhibit high Ba/Rb (12.2–26.1) and low Rb/Sr (0.03–0.08) ratios (Fig. 12b), likely suggesting that metasomatism by aqueous fluids may have triggered amphibole formation in the melt sources. Admittedly, Dai *et al.* (2019) attribute the concurrent presence of high Ba/Rb and low Rb/Sr ratios to the legacy of subducted igneous oceanic crust; however, this latter hypothesis cannot be considered given the continental intraplate setting of the lavas studied, unless it's considered as a recycled ancient oceanic crust.

The olivine crystals presented in this study have high Ca/Fe and 100*Mn/Fe ratios and a low 100*Ni/Mg ratio (Fig. 12c–12d), symptomatic of olivine crystallization from a carbonated mantle source-derived magma, according to Ammannati *et al.* (2016). In other words, the SCLM beneath the Bini Warack area has undergone a carbonate metasomatism.

## 6 Conclusion

The present mineralogical and geochemical study of lavas and hosted xenoliths from Bini Warack area of the CVL shed light on magmatic events, petrogenetic processes and provides informations on the sub–continental mantle beneath the Adamawa plateau, marking the transition from the Congo Archean-Paleoproterozoic craton to the Neoproterozoic juvenile crust involved in the Pan-African Central Africa Orogenic Belt.

Lavas from Bini Warack are alkaline and include basanite, alkali basalt and latite, with $SiO_2$ contents ranging from 42.4 to 56.6 wt% while mantle xenoliths are all spinel bearing lherzolite with protogranular to porphyroclastic textures. Mafic lavas are sodic while the only latite sample is potassic, both originated from a similar mantle source with signatures of at least three mantle components (REC, HIMU and EM1). Their OIB character and isotopic ratios are consistent with plume activity.

The mantle xenoliths are spinel lherzolites displaying protogranular to porphyroclastic textures, mainly consisting of minerals with fertile compositions ($Fo_{84-91}$, spinel Cr#:0.1 – 0.22; Al-rich pyroxenes), and are characterized by U/Th typically lower than 1, as well as slight enrichment in LILE relative to HFSE.

The presence of mantle xenoliths in most lavas and the relatively low Sr isotopic of the latter indicate a rapid ascend of their parental magmas, low degree of fractional crystallization and insignificant assimilation or crustal contamination. According to the melting model, the parental magmas of the studied lavas were generated near 80 to 150 km depth, by $\leq$2% partial melting of lherzolitic mantle source containing 2%–6% of garnet, and characterized by a low oxygen fugacity condition and low water content. Trace element concentrations together with olivines chemical features suggest that the SCLM beneath the Bini Warack area have undergone a carbonate-rich metasomatism.

## Acknowledgments

The current work was financially supported by the CNRS–IRD LithoCOAC project. Two research stays in the laboratory *Geosciences Environnement Toulouse* of the University Paul Sabatier Toulouse 3, France, were consecutively granted to the first author for analytical facilities, in addition to his participation in the 2023 South America Exploration Initiative (SAXI) workshop in *Vallées d'Antraigues–Asperjoc* funded by the CNRS IRN FALCoL directed by Olivier Vanderhaeghe. We deeply acknowledge Fabienne De Parseval for the confection of the thin sections presented in this paper and Philippe De Parseval, Sophie Gouy, and Stéphanie Mandrou for their technical assistance during the microprobe and TIMS analyses, respectively. We also thank Etienne Médard and an anonymous reviewer for their significant and constructive comments and the editorial assistance from Laurent Jolivet.

## References

Adam J, Green T. 2006. Trace element partitioning between mica- and amphibole-bearing garnet lherzolite and hydrous basanitic melt: 1. Experimental results and the investigation of controls on partitioning behaviour. Contrib Mineral Petrol 152: 1–17.

Adama H, Nkouandou OF, Bardintzeff JM, *et al*. 2021. Petrography and geochemistry of the harzburgite xenoliths of lake Guinnadji and Ngao Djalsoka volcano from the Dibi area (Adamawa Plateau – Cameroon). J Geogr Envir Earth Sci Intern 25(10): 178–193.

Aït-Hamou F, Dautria J-M, Cantagrel J-M, Dostal J, Briqueu L. 2000. Nouvelles données géochronologiques et isotopiques sur le volcanisme cénozoïque de l'Ahaggar (Sahara algérien): des arguments en faveur de l'existence d'un panache. CR Acad Sci 330(12): 829–836.

Ammannati E, Jacob DE, Avanzinelli R, Foley SF, Conticelli S. 2016. Low Ni olivine in silica-undersaturated ultrapotassic igneous rocks as evidence for carbonate metasomatism in the mantle. Earth Planet Sci Lett 444: 64–74.

Arai S. 1994. Characterization of spinel peridotites by olivine-spinel compositional relationships: review and interpretation. Chem Geol 113(3–4): 191–204.

Asaah ANE, Yokoyama T, Aka TF, *et al*. 2015a. Geochemistry of lavas from maar–bearing volcanoes in the Oku volcanic group of the Cameroon Volcanic Line. Chem Geol 406: 55–69.

Asaah ANE, Yokoyama T, Aka TF, *et al*. 2015b. A comparative review of petrogenetic processes beneath the Cameroon Volcanic Line: geochemical constraints. Geosci Front 6(4): 557–570.

Bian X, Su Y, Zheng J, Wang J, Chen X, Zhou L, *et al*. 2024. Multistage melt/fluid modification of lithospheric mantle beneath the circum-cratonic orogenic belt: Evidence from the Tuoyun peridotite xenoliths. Geol Soc America Bull 137(1-2): 220–240. https://doi.org/10.1130/B37552.1.

Bardintzeff J-M, Nkouandou OF, Mefire AF. 2020. First occurrence of pigeonite in the Cameroon Volcanic Line. Arab J Geosci 13: 496.

Bédard JH. 2006. A catalytic delamination-driven model for coupled genesis of Archaean crust and sub-continental lithospheric mantle. Geochim Cosmochim Acta 70: 1188–1214.

Bénard A, Müntener O, Pilet S, Arculus R, Nebel O. 2021. Silica-rich spinel harzburgite residues formed by fractional hybridization-melting of the intra-oceanic supra-subduction zone mantle: new evidence from TUBAF seamount peridotites. Geochim Cosmochim Acta 293: 477–506.

Bilong P, Ndjigui P-D, Temdjim R, Sababa E. 2011. Geochemistry of peridotite and granite xenoliths under the early stages of weathering in the Nyos volcanic region (NW-Cameroon): implications for PGE exploration. Chem Erde Geochem 71: 77–86.

Boyd FR. 1989. Compositional distinction between oceanic and cratonic lithosphere: Earth Planet Sci Lett 1–2(96): 15–26.

Boyd FR, Mertzman SA. 1987. Composition and structure of the Kaapvaal lithosphere, Southern Africa. In: Mysen BO, ed. Magmatic processes: physicochemical principles. Houston: Geochemical Society, pp. 3–12.

Boyd FR, Pokhilenko NP, Pearson DG, Mertzman SA, Sobolev NV, Finger LW. 1997. Composition of the Siberian cratonic mantle: evidence from Udachnaya peridotite xenoliths: Contrib Mineral Petrol 128(2–3): 228–246.

Brey GP, Köhler T. 1990. Geothermobarometry in four phase lherzolites II. New thermobarometers and practical assessment of existing thermobarometers. J Petrol 31: 1353–1378.

Caldeira R, Munhá JM. 2002. Petrology of ultramafic nodules from São Tomé Island, Cameroon Volcanic Line (oceanic sector). J Afr Earth Sci 34: 231–246.

Canil D. 2004. Mildly incompatible elements in peridotites and the origins of mantle lithosphere. Lithos 77: 375–393.

Carignan J, Hild P, Mevelle G, Morel J, Yeghicheyan D. 2001. Routine analyses of trace elements in geological samples using flow injection and low pressure on–line liquid chromatography coupled to ICP–MS: a study of geochemical reference materials BR, DR–N, UB–N, AN–G and GH. Geostand Newslett 25: 187–198.

Carlson RW, Pearson DG, James DE. 2005. Physical, chemical, and chronological characteristics of continental mantle. Rev Geophys 43(1): RG1001. doi:10.1029/2004RG000156

Christiansen EH. 2009. Petromode. Faculty Publications, Brigham Young University, Provo. http://scholarsarchive.byu.edu/facpub/1334

Condie KC. 2005. High field strength element ratios in Archean basalts: a window to evolving sources of mantle plume. Lithos 79: 491–504.

Cvetković V, Radivojević M, Prelević D, Toljić M, Turki SM. 2022. An insight into the evolution of the lithospheric mantle of south

Saharan metacraton: Mantle xenoliths from Jabal Eghei Volcanic Complex, Libya. J Volc Geotherm Res 432: 107691.

Dai HK, Zheng JP, O'Reilly SY, *et al*. 2019. Langshan basalts record recycled Paleo-Asian oceanic materials beneath the northwest North China Craton. Chem Geol 524: 88–103.

Dai HK, Zheng JP, Xiong Q, Griffin WL, O'Reilly SY. 2023. Continental thermal blanketing explains the compositional dichotomy of the diffuse basaltic province across central-eastern Asia. Geophys Res Lett 50: e2023GL104951.

Dai HK, Zheng J, Xiong Q, Hu L, Zhou X. 2024. Insight of enriched basalts into the nature and evolution of mantle lithosphere beneath craton margins. Sci China Earth Sci 67: 3128–3142. https://doi.org/10.1007/s11430-024-1371-x

De Hoog JCM, Gall L, Cornell DH. 2010. Trace-element geochemistry of mantle olivine and application to mantle petrogenesis and geothermobarometry. Chem Geol 270(1–4): 196–215.

Delpech G, Grégoire M, O'Reilly SY, Cottin JY, Moine B, Michon G. 2004. Feldspar from carbonate– rich metasomatism in the oceanic mantle under Kerguelen Islands (South Indian Ocean). Lithos 75: 209–237.

DePaolo DJ. 1981. Trace Element and Isotopic Effects of Combined Wall Rock Assimilation and Fractional Crystallization. *Earth Planet Sci Lett* 53: 189–202.

Déruelle B, Ngounouno I, Demaiffe D. 2007. The Cameroon Hot Line (CHL): a unique example of active alkaline intraplate structure in both oceanic and continental lithospheres. CR Geosci 339: 589–598.

Doucet LS, Ionov DA, Golovin AV, Pokhilenko NP. 2012. Depth, degrees and tectonic settings of mantle melting during craton formation: inferences from major and trace element compositions of spinel harzburgite xenoliths from the Udachnaya kimberlite, Central Siberia. Earth Planet Sci Lett 359-360: 206–218.

Doucet L, Li Z–X, Brennan D, *et al*. 2023. Precambrian history of the Pacific Mantle Domain: New constraints from Woodsreef and Port Macquarie serpentinized spinel harzburgites of the New England orogen, Australia. J Petrol 64: 1–24.

Downes H. 1997. Shallow continental lithospheric mantle heterogeneity–petrological constraints. In: Fuchs K, ed. Upper mantle heterogeneities from active and passive seismology. Dordrecht: Kluwer Academic, pp. 295–308.

Downes H, Reichow MK, Mason PRD, Beard AD, Thirlwall MF. 2003. Mantle domains in the lithosphere beneath the French Massif Central: trace element and isotopic evidence from mantle clinopyroxenes. Geol Mag 140: 71–87.

Fairhead JD, Okereke CS. 1988. Depths to major density contrasts beneath the West African rift system in Nigeria and Cameroon based on the spectral analysis of gravity data. J Afr Earth Sci 7(5–6): 769–777.

Falloon TJ, Danyushevsky LV. 2000. Melting of refractory mantle at 1.5, 2, and 2.5 GPa under anhydrous and $H_2O$-undersaturated conditions: Implications for the petrogenesis of high-Ca boninites and the influence of subduction components on mantle melting. J Petrol 41: 257–283.

Frey FA, Green DH, Roy SD. 1978. Integrated models of basalts petrogenesis: a study of quartz tholeiites to olivine melilites from South Eastern Australia utilizing geochemical and experimental petrological data. J Petrol 19: 463–513.

Furman T, Graham D. 1999. Erosion of lithospheric mantle beneath the East African Rift system: Geochemical evidence from the Kivu volcanic province. Lithos 48: 237–262.

Gale A, Dalton CA, Langmuir CH, Su YJ, Schilling JG. 2013. The mean composition of ocean ridge basalts. *Geochem Geophys Geosyst* 14: 489–518.

Grégoire M, Moine BN, O'Reilly SY, Cottin JY, Giret A. 2000a. Trace element residence and partitioning in mantle xenoliths metasomatised by high alkaline silicate and carbonate-rich melts (Kerguelen Islands, Indian Ocean). J Petrol 41: 477–509.

Grégoire M, Lorand J-P, O'Reilly S-Y, Cottin J-Y. 2000b. Armalcolite-bearing, Ti-rich metasomatic assemblages in harzburgitic xenoliths from the Kerguelen Islands: Implications for the oceanic mantle budget of high-field strength elements. Geochim Cosmochim Acta 64: 673–694.

Halliday AN, Davidson JP, Holden P, DeWolf C, Lee D-C, Fitton J. G. 1990. Trace element fractionation in plumes and the origin of HIMU mantle beneath the Cameroon line. Nature 347: 523–528.

Hawkesworth CJ, Erlank AJ, Marsh JS, Menzies MA, Calsteren P. 1983. Evolution of the continental lithosphere: evidence from volcanics and xenoliths from southern Africa. In: Hawkesworth CJ, Norry MJ, eds. Continental basalts and mantle xenoliths. Nantwich: Shiva Publishing, pp. 111–138.

Herrmann W, Berry RF. 2002. MINSQ—a least squares spreadsheet method for calculating mineral proportions from whole rock major element analyses. Geochem Expl Envir Anal 2: 361–368.

Herzberg C. 2004. Geodynamic in formation in peridotite petrology. J Petrol 45: 2507–2530.

Herzberg C, Rudnick R. 2012. Formation of cratonic lithosphere: an integrated thermal and petrological model. Lithos 149: 4–15.

Ishii T, Robinson PT, Maekawa H, Fiske R. 1992. Petrological studies of peridotites from diapiric serpentinite seamounts in the Izu–Ogasawara–Mariana forearc, Leg 125. In: Fryer P, Pearce JA, Stokking LB, *et al.*, eds. Proc Ocean Drill Program Sci Results 125: 445–485.

Itiga Z, Bardintzeff JM, Wotchoko P, Wandji P, Bellon H. 2013. Tchabal Gangdaba massif in the Cameroon Volcanic Line: a bimodal association. Arab J Geosci 7(11): 4641–4664.

Johnson MC, Plank T. 1999. Dehydration and melting experiments constrain the fate of subducted sediments. Geochem Geophys Geosyst 1: 1007.

Jung S, Masberg P. 1998. Major and trace element systematics and isotope geochemistry of Cenozoic mafic volcanic from the Vogelsberg (Central Germany): constraints on the origin of continental alkaline and tholeiitic basalts and their mantle sources. J Volcanol Geotherm Res 86: 151–177.

Kamenetsky VS, Crawford AJ, Meffre S. 2001. Factors controlling chemistry of magmatic spinel: an empirical study of associated olivine, Cr-spinel and melt inclusion from primitive rocks. J Petrol 42: 655–671.

Kushiro I. 1996. Partial melting of a fertile peridotite at high pressures: An experimental study using aggregates of diamond. Geophys Monogr 95: 109–122.

Kretz R, 1983. Symbols for rock-forming minerals. Am Mineral 68: 277–279.

Labou I, Benoît M, Baratoux L, *et al*. 2020. Petrological and geochemical study of Birimian ultramafic rocks within the West African Craton: insights from Mako (Senegal) and Loraboué (Burkina Faso) lherzolite/harzburgite/wehrlite associations. J Afr Earth Sci 162: 103677.

Le Bas MJ, Le Maître RW, Streckeisen A, Zanettin B. 1986. A chemical classification of volcanic rocks based on the total alkali-silica diagram. *J Petrol* 27: 745–750.

Lee D-C, Halliday AN, Davies GR, Essene EJ, Fitton JG, Temdjim R. 1996. Melt enrichment of shallow depleted mantle: a detailed petrological, trace element and isotopic study of mantle-derived xenoliths and megacrysts from the Cameroon Line. J Petrol 37(2): 415–441.

Li C–F, Li X–H, Li Q–L, Guoa J–H, Lia X–H. 2011. Directly determining $^{143}Nd/^{144}Nd$ isotope ratios using thermal ionization mass spectrometry for geological samples without separation of Sm–Nd. J Anal At Spectrom 26: 2012–2022.

Li C–F, Li X–H, Li Q–L, Guoa J–H, Li X–H, Yanga Y–H. 2012. Rapid and precise determination of Sr and Nd isotopic ratios in geological samples from the same filament loading by thermal ionization mass spectrometry employing a single–step separation scheme. Anal Chim Acta 727: 54–60.

Liang Y, Sun C, Yao L. 2013. A REE-in-two-pyroxene thermometer for mafic and ultramafic rocks. Geochim Cosmochim Acta 102: 246–260.

Lin A–B, Aulbach S, Zheng J–P, *et al*. 2022. Lithospheric mantle provinces and crust–mantle decoupling beneath northeastern China: Insights from peridotite xenoliths. GSA Bull 0: 1–19.

Liu J, Scott JM, Martin CE, Pearson DG. 2015. The longevity of Archean mantle residues in the convecting upper mantle and their role in young continent formation: Earth Planet Sci Lett 424: 109–118.

Lundstrom CC, Hoernle K, Gill J. 2003. U–series disequilibria in volcanic rocks from the Canary Islands: plume versus lithosphere melting. Geochim Cosmochim Acta 67: 4153–4177.

Ma L, Jiang SY, Hofmann AW, *et al*. 2014. Lithospheric and asthenospheric sources of lamprophyres in the Jiaodong Peninsula: a consequence of rapid lithospheric thinning beneath the North China Craton? Geochim Cosmochim Acta 124: 250–271.

Marzoli A, Renne PR, Piccirillo EM, *et al*. 1999. Silicic magmas from the continental Cameroon Volcanic Line (Oku, Bambouto and Ngaoundere): $^{40}Ar$-$^{39}Ar$ dates, petrology, Sr-Nd-O isotopes and their petrogenetic significance. Contrib Mineral Petrol 135: 133–150.

MacDonald R, Rogers NW, Fitton JG, Black S, Smith M. 2001. Plume–lithosphere interactions in the generation of the basalts of the Kenya Rift, East Africa. J Petrol 42: 877–900.

Marzoli A, Piccirillo EM, Renne PR, *et al*. 2000. The Cameroon Volcanic Line revisited: petrogenesis of continental basaltic magmas from lithospheric and asthenospheric mantle sources. J Petrol 41: 87–109.

Maury RC, Brousse R. 1978. Présence de pigeonite et d'orthopyroxène dans certaines laves du Massif central français: leur répartition et leur origine. Bull Soc Française de Minéralogie et Cristallographie 109: 10–21.

McDonough WF, Sun SS. 1995. The composition of the Earth. *Chem Geol* 120: 223–253.

Mbassa BJ, Sole J, Dawai D, *et al*. 2025. New K–Ar data in the northeastern edge of the Adamawa-Yadé domain, Central African Pan-African Fold belt: shedding light on the transition age between convergent and divergent tectonic regimes. CR Geosci 357: 145–165.

McDonough WF, Rudnick RL. 1998. Mineralogy and composition of the upper mantle. In: Russell J, Hemley, eds. Reviews in Mineralogy 37, Ultrahigh–pressure mineralogy: physics and chemistry of the Earth's deep Interior. Ribbe PH, Series Ed. Washington DC: Mineral Soc Amer, pp. 139–164.

McKenzie DP, O'Nions RK. 1983. Mantle reservoirs and oceanic island basalts. Nature 301: 229–231.

McKenzie DP, O'Nions RK. 1995. The source regions of ocean island basalts. J Petrol 36: 133–159.

Milelli L, Fourel L, Jaupart C. 2012. A lithospheric instability origin for the Cameroon Volcanic Line. Earth Planet Sci Lett 335–336: 80–87.

Moine BN, Grégoire M, O'Reilly SY, Sheppard SMF, Cottin JY. 2001. High field strength element (HFSE) fractionation in the upper mantle: evidence from amphibole-rich composite mantle xenoliths from the Kerguelen Islands (Indian Ocean). J Petrol 42: 2145–2167.

Morimoto N, Fabriès J, Ferguson AK, *et al*. 1988. Nomenclature of pyroxenes. Am Mineral 73: 1123–1133.

Ngako V, Affaton P, Nnangue JM, Njanko T. 2003. Pan-African tectonic evolution in central and southern Cameroon: transpression and transtension during sinistral shear movements. J Afr Earth Sci 36: 207–214.

Nkouandou OF, Ngounouno I, Déruelle B, Ohnenstetter D, Montigny R, Demaiffe D. 2008. Petrology of the Mio–Pliocene volcanism to the North and East of Ngaoundéré (Adamawa, Cameroon). CR Geosci 340: 28–37.

Nkouandou OF, Temdjim R. 2011. Petrology of spinel lherzolite xenoliths and host basaltic lava from Ngao Voglar volcano, Adamawa Massif (Cameroon Volcanic Line, West Africa): equilibrium conditions and mantle characteristics. J Geosci 56: 375–387.

Nguihdama D, Chazot G, Kamgang P, Mbowou GIB, Ngounouno I. 2014. Spinel–bearing lherzolite xenoliths from Hosséré Garba (Likok, Adamawa–Cameroon): Mineral compositions and geothermobarometric implications. Intern J Geosci 5: 1435–1444.

Nkouandou OF, Bardintzeff J–M, Fagny AM. 2015. Sub–continental lithospheric mantle structure beneath the Adamawa plateau inferred from the petrology of ultramafic xenoliths from Ngaoundéré (Adamawa plateau, Cameroon, Central Africa). J Afr Earth Sci 111: 26–40.

Nnange Metuk J, Ngako V, Fairhead JD, Ebinger CJ. 2000. Depths to density discontinuities beneath the Adamawa Plateau region, Central Africa, from spectral analyses of new and existing gravity data. J Afr Earth Sci 30 (4): 887–901.

Nono A, Déruelle B, Demaiffe D, Kambou R. 1994. Tchabal Nganha volcano in Adamawa (Cameroon): petrology of a continental alkaline series. J Volcanol Geotherm Res 60: 147–178.

Owona S, Mvondo Ondoa J, Ekodeck GE. 2013. Evidence of quartz, feldspar and amphibole crystal plastic deformations in the Palaeoproterozoic Nyong complex shear zones under amphibolite to granulite conditions (West Central African Fold Belt, SW Cameroon). J Geogr Geol 5 (3): 186–201.

Pearce JA. 2008. Geochemical fingerprinting of oceanic basalts with applications to ophiolite classification and the search for Archean oceanic crust. Lithos 100: 14–48.

Pearce JA, Van der Laan SR, Arculus RJ, *et al*. 1992. Boninite and harzburgite from Leg 125 (Bonin-Mariana forearc): a case study of magma genesis during the initial stages of subduction. Proceeding of the Ocean Drilling Program, Sci Results, 125: 623–659

Pearson DG. 1999. The age of continental roots: Lithos 48: 171–194.

Pearson DG, Nowell GM. 2002. The continental lithospheric mantle: characteristics and significance as a mantle reservoir. Phil Trans R Soc London A 360: 2383–2410.

Pintér Z, Patkó L, Djoukam JFT, *et al*. 2015. Characterization of the sub–continental lithospheric mantle beneath the Cameroon volcanic line

inferred from alkaline basalts hosted peridotite xenoliths from Barombi Mbo and Nyos Lakes. J Afr Earth Sci 111: 170–193.

Poudjom Djomani Y, Nnange MJ, Diament C, Ebinger, Fairhead J. 1995. Effective elastic thickness and crustal thickness variations in West Central Africa inferred from gravity data. J Geophys Res 100 (B11): 22047–22070.

Putirka K. 1999. Clinopyroxene + liquid equilibria to 100 kbar and 2450 K. *Contrib Min Petrol* 135: 151–163.

Puziewicz J, Aulbach S, Kaczmarek M–A, *et al*. 2023. The origin and evolution of DMM–like lithospheric mantle beneath continents: mantle xenoliths from the Oku volcanic group in the Cameroon Volcanic Line, West Africa. J Petrol 64: 1–25.

Rankenburg K, Lassiter J, Brey G. 2005. The role of continental crust and lithospheric mantle in the genesis of Cameroon Volcanic Line lavas: constraints from isotopic variations in lavas and megacrysts from the Biu and Jos Plateaux. J Petrol 46: 169–190.

Reagan MK, Ishizuka O, Stern RJ, *et al.*, 2010. Fore–arc basalts and subduction initiation in the Izu–Bonin–Mariana system. Geochem Geophys Geosyst 11: Q03X12.

Sababa E, Ndjigui P-D, Ebah Abeng SA, Bilong P. 2015. Geochemistry of peridotite xenoliths from the Kumba and Nyos areas (southern part of the Cameroon volcanic line): implications for Au-PGE exploration. J. Geochem Explor 152: 75–90.

Simon NSC, Neumann E-R, Bonadiman C, *et al*. 2008. Ultra-refractory domains in the oceanic mantle lithosphere sampled as mantle xenoliths at Ocean Islands. J Petrol 49: 1223–1251

Smith JV, Brown W. 1988. Nomenclature, general properties of feldspars and simple determinative diagrams. In: Feldspar Minerals, 2nd revised and extended ed. Berlin Heidelberg: Springer Verlag, pp. 208–228.

Sobolev AV, Hofmann AW, Kuzmin AV, *et al*. 2007. The amount of recycled crust in sources of mantle-derived melts. Science 5823 (316): 412–417.

Stevens RE. 1944. Composition of some chromites of the western hemisphere. Amer Mineral 29: 1–34.

Stracke A, Hofmann AW, Hart SR. 2005. FOZO, HIMU, and the rest of the mantle zoo. Geochem Geophys Geosyst 6: Q05007. doi:10.1029/2004GC000824

Streckeisen A. 1976. To each plutonic rock its proper name. Earth Sci Rev 12: 1–33.

Suh CE, Luhr JF, Njome MS. 2008. Olivine-hosted glass inclusions from Scoriae erupted in 1954–2000 at Mt Cameroon volcano, West Africa. J Volcanol Geotherm Res 169: 1–33.

Sun S-S, McDonough WF. 1989. Chemical and isotopic systematics of oceanic basalts: implications for mantle composition and processes. In: A D. Saunders and MJ. Norry (Eds). Magmatism in the Ocean Basins. *Geol Soc London*. 313–345.

Tamen J, Nkoumbou C, Mouafo L, Reusser E, Tchoua FM. 2007. Petrology and geochemistry of monogenetic volcanoes of the Barombi Koto volcanic field (Kumba graben, Cameroon volcanic line): implications for mantle source characteristics. CR Geosci 339: 799–809.

Tamen J, Nkoumbou C, Reusser E, Tchoua F. 2015. Petrology and geochemistry of mantle xenoliths from the Kapsiki Plateau (Cameroon Volcanic Line): implications for lithospheric upwelling. J Afr Earth Sci 101: 119–134.

Tatsumi YM, Sakuyama H, Fukuyama H, Kushiro I. 1983. Generation of basalt magmas and the thermal structure of the mantle wedge in subduction zones. J Geophys Res 88: 5815–5825.

Taylor SR, McLennan SM. 1985. The Continental Crust: Its Composition and Evolution. Blackwell Scientific, Oxford.

Tedonkenfack SST, Puziewicz J, Aulbach S, *et al*. 2021. Lithospheric mantle refertilization by DMM-derived melts beneath the Cameroon Volcanic Line—a case study of the Befang xenolith suite (Oku Volcanic Group, Cameroon). Contrib Mineral Petrol 176: 37. doi:10.1007/s00410–021–01796–3

Teitchou M.I, Grégoire M, Dantas C, Tchoua FM. 2007. Le manteau supérieur à l'aplomb de la plaine de Kumba (ligne du Cameroun), d'après les enclaves de péridotites à spinelles dans les laves basaltiques. CR Geosci 339: 101–109.

Teitchou MI, Grégoire M, Temdjim R, Ghogomu RT, Ngwa C, Aka FT. 2011. Mineralogical and geochemical fingerprints of mantle metasomatism beneath Nyos volcano (Cameroon volcanic line). In: Beccaluva L, Bianchini G, Wilson M, eds. Volcanism and Evolution of the African Lithosphere. Geol Soc Am Spec Paper 478: 193–210.

Temdjim R, Njilah IK, Kamgang P, Nkoumbou C. 2004. Données nouvelles sur les laves felsiques de Ngaoundéré (Adamaoua, ligne du Cameroun): chronologie et pétrologie. Afr J Sci Technol 5(2): 113–123.

Temdjim R, Tchouankoué JP, Kamgang P, Tchoua F. 2006. Sur l'existence d'un maar trachytique dans la Ligne volcanique du Cameroun: le maar Mbalang–Djalingo dans la région de Ngaoundéré (Plateau de l'Adamaoua). Rev Géogr Cameroun XVII (1): 67–71.

Thompson RN, Gibson SA. 2000. Transient high temperatures in mantle plume heads inferred from magnesian olivines in Phanerozoic picrites: Nature 407(6803): 502–506.

Tiabou FA, Temdjim R, Wandji P, *et al*. 2019. Baossi–Warack monogenetic volcanoes, Adamawa Plateau, Cameroon: petrography, mineralogy and geochemistry. Acta Geochim 38: 40–67.

Tokam APK, Tabod CT, Nyblade AA, Julia J, Wiens DA, Pasyanos ME. 2010. Structure of the crust beneath Cameroon, West Africa, from the joint inversion of Rayleigh wave group velocities and receiver functions. Geophys J Int 183(2): 1061–1076.

Wagsong Njombie MP, Temdjim R, Foley SF. 2018. Petrology of spinel lherzolite xenoliths from Youkou volcano, Adamawa massif, Cameroon Volcanic Line: mineralogical and geochemical fingerprints of sub–rift mantle processes. Contrib Mineral Petrol 173: 13.

Wandji P, Tsafack JPF, Bardintzeff JM, Nkouathio DG, et al. 2009. Xenoliths of dunites, wehrlites and clinopyroxenites in the basanites from Batoke volcanic cone (Mount Cameroon, Central Africa): petrogenetic implications. *Mineral Petrol* 96: 81–98.

Weaver BL. 1991. The origin of ocean island basalt end-member compositions: trace element and isotopic constraints. *Earth Planet Sci Lett* 104:381–397

Weber B. 1991. Interactions between basalt and mantle lithosphere in intraplate oceanic context: examples from Tahiti and Tahaa (fast drifting plate) and Reunion island (slow drifting plate). Univ. thesis, Ecole des Mines de Paris, 222p. https://www.sudoc.fr/044195990

Workman RK, Hart SR. 2005. Major and trace element composition of the depleted MORB mantle (DMM). Earth Planet Sci Lett 231: 53–72.

Xu R, Liu YS, Lambart S, *et al*. 2022. Decoupled Zn–Sr–Nd isotopic composition of continental intraplate basalts caused by two-stage melting process. Geochim Cosmochim Acta 326: 234–252.

Yokoyama T, Aka FT, Kusakabe M, Nakamura E. 2007. Plume–lithosphere interaction beneath Mt. Cameroon volcano, west

Africa: constraints from $^{238}U$–$^{230}Th$–$^{226}Ra$ and Sr–Nd–Pb isotope systematics. Geochim Cosmochim Acta 71: 1835–1854.

Yuan L, Yan Q. 2022. The nature of the sub–continental lithospheric mantle beneath Thailand: evidence from xenocrysts in Cenozoic basalts. Intern Geol Rev 65(3): 396–415.

Zangana NA, Downes H, Thirlwall MF, Hegner E, 1997. Relationship between deformation, equilibration temperatures, REE and radiogenic isotopes in mantle xenoliths Ray Pic, Massif Central, France: an example of plume–lithosphere interaction? Contrib Mineral Petrol 127: 187–203.

Zhang HF, Sun M, Zhou XH, Fan WM, Zhai MG, Yin JF. 2002. Mesozoic lithosphere destruction beneath the North China Craton: Evidence from major-, trace-element and Sr-Nd-Pb isotope studies of Fangcheng basalts. Contrib Mineral Petrol: 144: 241–254.

Zindler A. Hart SR. 1986. Chemical geodynamics. Annu Rev Earth Planet Sci 14: 493–571.

**Cite this article as**: Mbassa BJ, Vanderhaeghe O, Grégoire M, Benoit M, Itiga Z, Ngwa NC, Kamgang P. 2026. Sub–continental lithospheric mantle beneath the Adamawa volcanic area (Cameroon Volcanic Line): inference from lavas and hosted mantle xenoliths from Bini Warack, NE-Ngaoundéré, Cameroon (Central Africa), BSGF - Earth Sciences Bulletin 197: 10. https://doi.org/10.1051/bsgf/2026005